Secondary organic aerosol formation from fossil fuel sources contribute majority of summertime organic mass at Bakersfield

Shang Liu[1], Lars Ahlm[1], Douglas A. Day[1,2], Lynn M. Russell[1*], Yunliang Zhao[3], Drew R. Gentner[4], Robin J. Weber[3], Allen H. Goldstein[3,4], Mohammed Jaoui[5], John H. Offenberg[6], Tadeusz E. Kleindienst[6], Caitlin Rubitschun[7], Jason D. Surratt[7], Rebecca J. Sheesley[8], and Scott Scheller[9]

[1]Scripps Institution of Oceanography, University of California, San Diego, La Jolla, CA, USA,

[2]now at: Cooperative Institute for Research in Environmental Studies, University of Colorado, Boulder, CO, USA

[3]Department of Environmental Science, Policy and Management, University of California, Berkeley, CA, USA

[4]Deptartment of Civil and Environmental Engineering, University of California, Berkeley, CA, USA

[5]Alion Science and Technology, Research Triangle Park, NC, USA

[6]National Exposure Research Laboratory, U.S. EPA, Research Triangle Park, NC, USA

[7]Department of Environmental Sciences and Engineering, Gillings School of Global Public Health, University of North Carolina at Chapel Hill, NC, USA

[8]Department of Environmental Science, Baylor University, Waco, TX, USA

[9]California Air Resources Board, Sacramento, CA, USA

[*]*Correspondence to*: Lynn M. Russell (lmrussell@ucsd.edu)

Key words: Secondary organic aerosol, organic functional group, FTIR, AMS, source apportionment, San Joaquin Valley

Abstract

Secondary organic aerosols (SOA), known to form in the atmosphere from oxidation of volatile organic compounds (VOCs) emitted by anthropogenic and biogenic sources, are a poorly understood but substantial component of atmospheric particles. In this study, we examined the chemical and physical properties of SOA at Bakersfield, California, a site influenced by anthropogenic and terrestrial biogenic emissions. Factor analysis was applied to the infrared and mass spectra of fine particles to identify sources and processing that contributed to the organic mass (OM). We found that OM accounted for 56% of submicron particle mass, with SOA components contributing 80% to 90% of OM from 15 May to 29 June 2010. SOA formed from alkane and aromatic compounds, the two major classes of vehicle-emitted hydrocarbons, accounted for 65% OM (72% SOA). The alkane and aromatic SOA components were associated with 200- to 500-nm-accumulation-mode particles, likely from condensation of daytime photochemical products of VOCs. In contrast, biogenic SOA likely formed from condensation of secondary organic vapors, produced from NO_3 radical oxidation reactions during nighttime hours, on 400- to 700-nm-sized primary particles, and accounted for less than 10% OM. Local petroleum operation emissions contributed 13% to the OM, and the moderate O/C (0.2) of this factor suggested it was largely secondary. Approximately 10% of organic aerosols in submicron particles was identified as either vegetative detritus (10%) or cooking activities (7%), from Fourier transform infrared spectroscopic and aerosol mass spectrometry measurements, respectively. While the mass spectra of several linearly-independent SOA components were nearly identical and external source markers were needed to separate them, each component had distinct infrared spectrum, likely associated with the source-specific VOCs from which they formed.

1. **Introduction**

The organic fraction of atmospheric particles is comprised of a complex mixture of thousands of individual compounds [*Hamilton et al.*, 2004], which originate from a variety of sources and processes. In urban areas, the major source is fossil fuel combustion from gasoline- and diesel-powered vehicles and other industrial activities (e.g., oil burning). Emissions from these sources are largely composed of alkane and aromatic hydrocarbons, with a minor fraction of alkene compounds [*Kirchstetter et al.*, 1999; *Schauer et al.*, 1999]. Another important source, biogenic emissions, accounts for 90% of total volatile organic compounds (VOCs) globally [*Goldstein and Galbally*, 2007] and is key to particle formation in some regions (e.g., the southeastern US) [*Goldstein et al.*, 2009]. After emission, VOCs are transported from their sources during which time they are oxidized in the atmosphere, forming low-volatility products that can condense into the particle phase. The organic aerosols formed in the atmosphere are categorized as "SOA" (secondary organic aerosol) as opposed to "POA," organic aerosols directly emitted at their sources.

Formation of SOA is a dynamic process that involves complex chemical reactions and physical transformations. Despite significant progress in the past years, quantitative measurement of SOA mass and its mass fraction in organic aerosols remains challenging. The elemental carbon (EC)-tracer analysis has been used to identify non-SOA components since the 1980s [*Grosjean*, 1984]: The organic carbon (OC)-to-EC ratio that exceeds the average OC/EC from source measurements is assumed to be SOA [*Turpin et al*., 1991]. Using this method, field measurements conducted at Los Angeles suggested that production of SOA could be 3 to 4 times more than that of POA during smog events [*Grosjean*, 1984; *Turpin et al*., 1991]. Supporting the argument that SOA could be the major OM component were reaction chamber studies carried out during this time, which showed high mass yields of precursor compounds [*Hatakeyama et al.*, 1985, 1987]. However, the EC-tracer approach

suffers from large uncertainties, since OC/EC of emission sources is highly variable and is substantially affected by meteorological conditions (e.g., air mixing) [*Gray et al*., 1986]. Another approach, the organic tracer-based chemistry mass balance (CMB) model [*Schauer et al*., 1996; *Cass*, 1998], has been applied to identify sources of atmospheric fine particles since the 1990s. In this method, the mass that cannot be predicted by the model is assigned to SOA [*Schauer et al.*, 2002a; *Zheng et al*., 2002]. Therefore, the CMB model does not directly predict SOA but provides an upper limit of SOA mass based on limited source markers (source types) [*Cass*, 1998]. Over the last 10 years, the development of aerosol mass spectrometer (AMS) and Fourier transform infrared (FTIR) spectroscopy has provided new insights for SOA quantification [*Jayne et al.*, 2000; *Maria et al.*, 2002]. Positive matrix factor (PMF) analysis applied to the AMS and FTIR measurements during field experiments carried out worldwide consistently showed that 65% to 95% of OM is oxygenated organic aerosols (OOA), having higher OM/OC and oxygen-to-carbon molar ratio (O/C) composition than expected for primary organic components [*Jimenez et al*., 2009; *Lanz et al*., 2007; *Liu et al.*, 2011; *Russell et al*., 2011; *Russell* 2003; *Turpin et al.*, 2000; *Zhang et al*., 2007].

However, there is a lack of direct evidence that oxidized OA equates to SOA, because some primary aerosols are oxidized (e.g., marine polysaccharides and vegetative detritus). Consequently, there is a need to directly compare OOA to laboratory-produced SOA. *Russell et al*. [2011] compared OOA to SOA generated in smog chamber. In this case, OOA was derived by factor analysis of FTIR measurements, a technique that provides more molecular functional group specificity than mass spectra methods that employ electron ionization. Results of this comparison suggested that functional group compositions of OOA and SOA are comparable and precursor (and sometimes oxidant) dependent, making it possible to separate out SOA and, so, help address the controversy of POA and SOA mass fractions. In addition, *Russell et al.* [2011] proposed that

atmospheric alkanes are important SOA precursors—oxidation of alkanes produces multigeneration SOA products, which is supported by a recent model simulation study [*Yee et al.*, 2012] that suggests more than two-thirds of alkane SOA are fourth or higher generation products after reaction for 10 hrs. Despite the improvements in laboratory and model studies, more field measurements are needed to separate SOA formed from different precursors and identify which mechanisms best explain chemical properties of SOA formed in the complex atmosphere.

Size distributions of SOA components can provide additional insights for identifying source and formation mechanisms of ambient particles. Primary combustion-related particles, such as those emitted from gasoline- and diesel-powered vehicles, are typically smaller than 100 nm [*Kittelson*, 1998], whereas dust particles are usually larger than 500 nm [*Tegen and Lacis,* 1996]. Primary particles from cooking activities, including charbroiling and frying, are found to be smaller than 200 nm [*Wallace et al.*, 2004]. Particles in 200- to 500-nm size range typically contain SOA formed by condensation of secondary organic vapors, because particles in this size range have the highest relative surface area that make mass transfer most efficient for growth [*Maria et al.*, 2004; *Seinfeld and Pandis*, 2006]. Size distributions of organic components are also important for evaluating climate impacts of aerosols, since radiative parameters of aerosol particles are strongly dependent on particle size [*Tegen and Lacis*, 1996]. Further, lifetime of particles, which determines the distance that particles can travel and hence particles' regional impacts, is affected by particle size. For these reasons, particle size distributions have been studied extensively [*Heintzenberg et al*., 2000; *Hoppel et al.*, 1990; *Whitby et al.*, 1972]. Although some specific SOA molecules (e.g., oxalic acid) or mass fragments (e.g., m/z 44) have been measured as functions of size [*Kawamura et al.*, 2007; *Alfarra et al.*, 2004], predicting size distributions of different types of ambient SOA (formed from different sources or processes) is challenging. A few studies have applied factor analysis to each size fraction

of size-resolved filter measurements (2-6 size ranges) with limited organic mass quantification [*Han et al.*, 2006*; Karanasiou et al.*, 2009*; Richard et al.*, 2011*; Srivastava et al.*, 2008]. In these studies, estimates of factor size distribution were made by comparing masses of the common factors (typically representing primary sources) derived from each size fraction. However, this approach is not practical for highly size-resolved data sets (e.g., AMS measurements with more than 100 size bins). Another approach, 3-D factorization method, has been valuable for providing time-resolved size distribution of factors and have been recently applied to AMS measurements with success [*Ulbrich et al.*, 2012]. However, to generate physically meaningful factors, this analysis often requires prior information derived from 2-D factorization plus comparisons of results derived from different 3-D factorization methods, which is complicated and, so, the 3-D factorization methods have not been widely used. Thus, despite these improvements, size distributions of ambient SOA components have not been widely investigated.

In this context, we used collaborative measurements at Bakersfield in the San Joaquin Valley (SJV), one of the most polluted regions in the United States [*Chow et al.,* 1996], to study the oxidized fraction of OM. We began by quantifying oxygenated organic functional group and mass fragment abundances of bulk and single particles. Next, we identified sources and processes that contributed to OM using factor analysis and source-specific organic and inorganic marker compounds. After distinguishing secondary components from primary emissions, we evaluated the SOA fraction of OM. In addition, primary and secondary single-particle types were identified using cluster analysis. Finally, we compared different secondary organic components—their precursors, oxidants that lead to formation, and time of production. Size distributions of the SOA components were used to help identify their potential formation mechanisms. These analyses were built on a set of particle- and gas-phase measurements presented as follows.

2. Experimental

2.1. Sampling site and meteorological conditions during the CalNex campaign

The CalNex (California Research at the Nexus of Air Quality and Climate Change) campaign is a collaborative effort aimed at characterizing chemical and physical properties of aerosols in California. One supersite was located at Bakersfield in Kern County in the San Joaquin Valley (SJV). SJV is surrounded by coastal mountain ranges to the west, the Sierra Nevada range to the east, and the Tehachapi Mountains to the south [*Chow et al.*, 2006b], topography that regularly precludes air ventilation. The basin's air pollution levels are especially high during wintertime [*Chow et al.*, 2006a, 2006b]. Bakersfield, located in SJV's southern region and one of its biggest cities, has a wintertime $PM_{2.5}$ concentration often exceeding 50 μg m^{-3}, with OM typically accounting for more than 50% of the $PM_{2.5}$ mass [*Chow et al.*, 2006b]. Previous studies conducted at other sites in Bakersfield showed that gasoline- and diesel-powered vehicles, wood combustion, and meat cooking comprise the site's major air pollution sources [*Kleeman et al.*, 2009; *Schauer and Cass*, 2000]; wood combustion may prevail only in winter [*Chow et al.*, 2006b]. In addition, biogenic hydrocarbons emitted from trees in the foothills are likely significant contributors to summertime VOCs [*Tanner and Zielinska,* 1994], providing potential biogenic precursors to form biogenic SOA. Thus, the high concentration of air pollution and the variety of its sources make Bakersfield an ideal site for studying ambient particles.

Measurements were conducted from 15 May to 29 June 2010 at Bakersfield (35.35º N, 118.97º W). The sampling site, located in an open urban area at the southeast edge of the city center close to freeway 99 (7 km to the west) and highway 58 (0.8 km to the north), had no nearby obstructions (e.g., tall trees or buildings). Instruments were deployed in temperature-controlled

(20ºC) containers with sampling heights of 3 to 5 m and 18 to 20 m above ground level, respectively, for particle-phase and gas-phase measurements. The sampling period was characterized by a series of clear, dry days with consistent diurnal cycles of temperature and relative humidity (RH), except for 15 to 17 May when intermittent rainfall occurred. The average temperature for the campaign, 24°C, included a 7°C standard deviation, with minimums typically occurring at ~0500 hr and maximums often observed at ~1500 hr (lagged by 3 hr of solar radiation). RH was anticorrelated with temperature, with an average of 38% and a standard deviation of 17%. The observed diurnal cycle of wind direction was consistent with the pattern described by *Zhong et al.* [2004]: Northwesterly winds prevailed during daytime (0800 to 2100 hr); between midnight and early morning, easterly and southeasterly winds prevailed for 34 (of 45) days. Easterly and southeasterly winds represented downslope flows [*Zhong et al.*, 2004] that were likely associated with biogenic VOCs emitted from the mountains' coniferous trees (e.g., Sequoia National Forest), the chemistry of which being distinct from anthropogenic pollutants (e.g., aromatic and alkane hydrocarbons).

2.2. Spectroscopic measurements

2.2.1. Bulk particle organic functional groups

PM_1 and $PM_{2.5}$ filter (Teflon filters with pore size of 1 μm) samples were collected for FTIR analysis. Five PM_1 samples were collected daily, representing morning (0600-1200 hr), early afternoon (1200-1500 hr), late afternoon (1500-1800 hr), evening (1800-2300 hr), and nighttime (0000-0600 hr) periods (local time is used throughout the text). Improved time resolution of FTIR PM_1 samples (compared to previously reported 12- or 24-hr samples in *Russell et al.*, [2011]) allows analysis of diurnal variations of organic functional groups. Shorter sampling times also greatly enhanced statistical significance of data analysis (e.g., correlation analysis) and reduced uncertainties

caused by loss of semivolatile compounds. The one $PM_{2.5}$ sample collected each day (0000-2300 hr) that overlapped the multiple PM_1 sample collection times represented daily average $PM_{2.5}$ concentrations. Sample preparation and postprocessing have been detailed previously [*Gilardoni et al.*, 2009; *Liu et al.*, 2009]. Briefly, the filters were scanned using a Bruker Tensor 27 FTIR spectrometer with a deuterated triglycine sulfate (DTGS) detector (Bruker, Waltham, MA) before and after sample collection. Collected samples were immediately stored in a freezer (< 0ºC). An automated algorithm was used to conduct background subtraction, spectrum baselining, peak fitting, and peak integration procedures [*Day et al.*, 2010; *Russell et al.*, 2009]. Mass concentrations of organic functional groups, including alkane, hydroxyl, carboxylic acid, amine, carbonyl, organonitrate, alkene, aromatic, and organosulfate groups, were quantified. We excluded alkene and aromatic groups from this study because they were below the detection limit of the FTIR measurements for all samples.

2.2.2. Single-particle microscopy of organic functional groups

Single particles were impacted on Si_3N_4 windows on 18, 20, 22 May and 13 June. One morning and one afternoon sample were collected on each collection day. Stored samples were frozen below 0ºC. Sample analysis was performed at the Advanced Light Source (Lawrence Berkeley National Laboratory, CA) on beamline 5.3.2. Single-particle X-ray absorption spectra were acquired using a combination of scanning transmission X-ray microscopy (STXM) and near-edge X-ray absorption fine structure (NEXAFS) spectroscopy [*Russell*, 2002], which provided relative quantification of single-particle organic functional groups, including alkane, hydroxyl, ketone, alkene, and carboxylic acid groups. Functional group abundance was quantified using an automated algorithm developed by *Takahama et al*. [2010].

2.2.3. Elemental concentrations

A total of 150 PM_1 and 46 $PM_{2.5}$ filter samples used for FTIR analysis (65% and 100% of PM_1 and $PM_{2.5}$ samples, respectively) were selectively analyzed using X-ray fluorescence (XRF) at Chester Laboratories (Chester LabNet, Tigard, Oregon). Concentrations of 38 elements (heavier than Ne) were quantified. Elements Al, Si, S, K, Ca, Fe, Co, Zn, and Br were above detection limit in 80% of the samples.

2.3. Size-resolved organic and inorganic mass fragments for bulk and single particles

A high resolution time-of-flight aerosol mass spectrometer (HR-ToF-AMS; Aerodyne, Billerica, MA) was deployed to provide high time-resolution measurements of nonrefractory components, including OM, sulfate, nitrate, ammonium, and chloride. Particles passing through a 100-μm pinhole are focused and accelerated by an aerodynamic lens. The accelerated particles impact a heated surface (600ºC), and the nonrefractory components flash vaporized and ionized. The ionized vapor fragments are subsequently analyzed by a time-of-flight mass spectrometer [*Canagaratna et al.*, 2007]. The resulting high mass resolution allows the HR-ToF-AMS to separate ions that would otherwise overlap in a relatively low-mass resolution quadrupole detector (in a Quadrupole-AMS). As a result, the detector provides detailed quantitative elemental compositions from which the O/C, an indicator of the oxidation state of ambient aerosols [*Jimenez et al.*, 2009], can be calculated. The ionization efficiency (IE) of nitrate, which is used to calculate the mass of the fragments, was calibrated using 350 nm NH_4NO_3 particles (selected by a scanning differential mobility analyzer) every 3-5 days during the campaign. The relative IE (RIE) of ammonium, derived from the NH_4NO_3 calibration, was 4.1 during this study (the default RIE is 4.0 in the standard AMS

data analysis software). Particle sizes, measured by the time-of-flight between a rotating chopper and the vaporizer [*Jayne et al.*, 2000], provide size-resolved chemical composition measurements of submicron particles. A light-scattering (LS) module, coupled with the HR-ToF-AMS, optically detects single particles from a 405-nm laser before particles reach the vaporizer. Light pulses scattered by the particles trigger acquisition of single-particle mass spectra [*Cross et al.*, 2007], enabling real-time measurements of single-particle chemical compositions. The "mass spectrum" (MS) mode (including high S/N "V" mode and high mass resolution "W" mode), the "time-of-flight" (TOF) mode, and the "LS" mode alternated during operation, with a ~5-min time resolution for each measurement cycle.

The collection efficiency (CE) of the AMS measurements was evaluated by comparing AMS-measured particle mass to the mass derived from a scanning differential mobility analyzer (DMA; described in Section 2.3). Comparisons were made for particles of vacuum aerodynamic diameters (d_{va}) smaller than 700 nm and d_{va} smaller than 1 μm (Figure 1). The 700-nm size cut was selected (in addition to 1 μm) because smaller particle sizes (60 to 700 nm d_{va}) have nearly 100% transmission efficiency [*Jayne et al.*, 2000] and likely compare better with the DMA measurements in the same size range. AMS-measured PM_{700nm} and PM_1 were calculated by summing the concentrations of the individual components, each of which was derived by integrating their mass size distributions measured in TOF mode. A factor of 2 was applied to the integrated concentrations (i.e., multiply by 2) to scale the integrated concentration (from the TOF-mode measurements) to the concentration measured from the MS-V mode. To account for the missing refractory components, elemental carbon (EC) and the sum of EC and dust were added to PM_{700nm} and PM_1, respectively, assuming that dust mainly existed in the larger particles (700 nm–1 μm d_{va}). A density (ρ) of 1.4 g cm^{-3} was applied to convert the DMA-measured number concentration to mass concentration, assuming spherical

particles [*Ahlm et al.*, 2012]. The density was calculated by converting the vacuum aerodynamic diameter (d_{va}) measured by the AMS to the mobility diameter measured by the SMPS (d_m), using the equation $d_m = (d_{va}/\rho)\bullet \rho_0$ [*DeCarlo et al.*, 2004], where ρ is the effective density and $\rho_0 = 1.0$ g cm^{-3}. *Ahlm et al*. [2012] found that ρ = 1.4 g cm^{-3} resulted in the best agreement between the DMA-derived and AMS-measured mass size distributions. Concentrations were calculated by integrating the DMA-derived mass size distributions for particles smaller than 500 nm and 700 nm in mobility diameter (d_m), which corresponded to 700 nm and 1 μm in d_{va} ($d_m = d_{va}/\rho$), respectively. A set of CE (0.5–1) values was tested, and a CE of 0.80 resulted in the best comparison of the AMS- and DMA-derived masses (slopes are close to 1) for both PM_{700nm} and PM_1 (Figure 1). Therefore, a CE of 0.8 was assigned to each of the 5-min AMS-measured organic and inorganic components and the PMF-factors throughout the campaign.

2.4. Molecular organic markers

Speciated organic marker compounds were measured with 1- or 2-hr resolution using thermal desorption aerosol gas chromatograph-mass spectrometer (TAG) [*Williams et al.*, 2006; *Worton et al.*, *2010*]. The sampling strategy and configuration of TAG in this study are detailed in *Zhao et al*. [2012] (manuscript in preparation, 2012). Briefly, aerosols (gases and particles) passed through a $PM_{2.5}$ cyclone (SCC BGI Inc., Waltham, MA; ~5 m above ground level) are collected by a collection-thermal desorption cell. Collected particles are thermally desorbed and transferred into gas chromatograph-mass spectrometer for quantification. Gas- and particle-phase organic marker compounds are measured by periodically alternating an active carbon denuder situated downstream of the sampling inlet. The molecular source markers used in this study are from the TAG measurements (particle-phase marker compounds are used) unless otherwise specified.

In addition to in situ measurements using TAG, organic marker compounds were measured from daily filter (prebaked quartz fiber filters) samples that were collected (synchronizing the FTIR $PM_{2.5}$ sampling time) by high-volume filter samplers (Tisch Environmental Village of Cleves, OH) from 15 May to 30 June 2010. Multiple samplers were operated simultaneously so that multiple sets of samples were collected. One set of the samples was extracted using 125 mL 1:1 (v/v) dichloromethane and methanol mixture for 24 hr in a Soxhlet extractor. Filter extracts were evaporated to dryness, followed by derivatization using 250 μL N,O-bis (trimethylsilyl) trifluoroacetamide (BSTFA) with 1% trimethylchlorosilane (TMCS) and 100 μL pyridine [*Jaoui et al.*, 2004]. The derivatized sample was analyzed by GC-ion trap mass spectrometer (GC-MS; Thermoquest Model GCQ+, Austin, TX), with analysis procedures described previously [*Kleindienst et al.*, 2007, 2012; *Offenberg et al.*, 2011]. Another set of samples was spiked with deuterated internal standards (alkanes, polycyclic aromatic hydrocarbons, and cholestane) and extracted using accelerated solvent extraction (Dionex ASE 300) with dichloromethane and methanol (1:1). Extracts were then concentrated to 250 μL and analyzed using an Agilent 7890 GC coupled to an Agilent 5975 MS in electron impact (EI) ionization scan mode [*Sheesley et al.*, 2004]. A third set of the samples was extracted in 15 mL high-purity methanol (LC-MS Chromasolv grade, Sigma-Aldrich) by ultrasonication for 45 min. The extracts were dried under a gentle stream of N_2 gas. Dried extracts were reconstituted using 250 μL 1:1 (v/v) solvent mixture of 0.1% acetic acid in water (LC-MS Chromasolv grade, Sigma-Aldrich) and 0.1% acetic acid in methanol (LC-MS Chromasolv grade, Sigma-Aldrich). Reconstituted samples were shaken and sonicated for 5 min before being analyzed by an Agilent ultra performance liquid chromatography (UPLC) system coupled to a Agilent 6520 Series Accurate-Mass high resolution quadrupole time-of-flight mass spectrometer (Q-TOFMS) equipped with an electrospray ionization (ESI) source operated in the negative ion mode

(UPLC/ESI-HR-Q-TOFMS). Detailed operating conditions and spectral analyses are presented in [*Zhang et al.*, 2011].

2.5. Additional measurements

Other supporting particle-phase and gas-phase measurements included submicron particle number size distributions measured by a custom-built DMA with a time resolution of 11 min [*Ahlm et al.*, 2012], elemental carbon measured using a Sunset real-time EC/OC analyzer (Oregon, USA), ozone monitored by a Dasibi 1008 PC ozone monitor, and OH radicals measured by a ground-based tropospheric hydrogen oxides sensor (GTHOS).

Meteorological measurements included temperature and relative humidity (RH) monitored by a Vaisala HMP45C RH/T sensor, and wind direction and wind speed recorded using an R. M. Young 5103 Wind Monitor.

3. Results

OM was the major component in submicron particle mass (56%), followed by dust (12%), sulfate (11%), nitrate (9%), ammonium (8%), and EC (4%) (Figure 2a). In comparison, for particles smaller than 150 nm (PM_{150nm}), OM accounted for 76% of the particle mass [*Ahlm et al.*, 2012] (Figure 2c). The submicron OM (OM_1) concentration measured by FTIR varied from 0.4 to 11.5 μg m^{-3}, averaging 2.4 μg m^{-3} for the entire campaign (Table 1). This OM was substantially lower than the OM measured in Mexico City (9.9 μg m^{-3}) and in the vicinity of Houston (4.9 μg m^{-3}), using the same technique [*Liu et al.*, 2009; *Russell et al.*, 2009]; this suggested a lower PM pollution level at Bakersfield during CalNex than that in Mexico City and Houston. AMS- and FTIR-measured OM closely tracked each other (Figure 3) with a correlation coefficient (*r*) of 0.77. Linear regression of

the two quantities (intercept forced to zero) suggested that the FTIR-measured OM was on average nearly 70% of the CE-corrected AMS-measured OM. Given the measurement uncertainties (25%–30% for the FTIR and AMS measurements), the differences lie within the expected range for the two independent measurements. However, the possibility of desorption of semivolatile components from the 3- or 6-hr filter samples could not be ruled out, although the comparability of the AMS-FTIR mass differences for both the 3-hr and 6-hr samples suggests that volatile losses did not increase with sampling time as is usually expected [*Mader et al.*, 2001].

Major functional groups contributing to OM_1 included alkane (35%), hydroxyl (22%), and carboxylic acid (21%) groups, among which carboxylic acid and alkane groups correlated with an *r* of 0.90. Similar correlation between these two groups was observed previously [*Liu et al.*, 2011], suggesting that carboxylic acid and alkane groups formed from the same source and likely via the same mechanism, likely by photooxidation of gas-phase alkane molecules [*Russell et al.*, 2011]. Nonacid carbonyl groups, typically associated with oxidation products of aromatic compounds [*Lee and Lane*, 2010], accounted for 11% of the OM. Amine groups (9% OM) were likely associated with bovine emissions in the region, as animal husbandry operations are major sources of atmospheric ammonia and amines [*Schade and Crutzen*, 1995]. Organosulfate groups were below detection limit for all submicron particles and identified as 1% of $OM_{2.5}$ (Table 1), which is consistent with the low mass of organosulfate molecules (~0.2% OM) measured by UPLC/ESI-HR-Q-TOFMS at the same site.

To identify particle types, normalized FTIR (PM_1) spectra were grouped using the hierarchical clustering technique with the Ward algorithm [*Liu et al.*, 2009; *Russell et al.*, 2009; *Ward*, 1963]. In the Ward algorithm, each IR spectrum is initially considered as one category. The spectra are progressively merged by minimizing the sum-of-square errors. By selecting a level of

branching (k), the spectra can be grouped into k clusters. Using $k \geq 5$ resulted in at least two clusters that had similar functional group compositions, indicating splitting of certain clusters into smaller clusters that are not distinguishable. Hence $k = 4$ was selected as the largest number of clusters without splitting, resulting in four chemically distinct clusters (Figure 4). Particles in Cluster 1 had the largest fraction of nonacid carbonyl groups (15%) among the four clusters, with alkane, hydroxyl, and carboxylic acid groups contributing 29%, 28%, and 16% to the OM, respectively. Cluster 2 particles were mainly composed of alkane (42%) and carboxylic acid (29%) groups. Together, Cluster 1 and Cluster 2 accounted for 93% of the submicron FTIR spectra. Spectra in Cluster 3 were characterized by sharp alkane group peaks and had the largest fraction of alkane groups (52%) among the four clusters. Cluster 4 represented particles that were mainly composed of hydroxyl groups (65%). The distinct chemical composition of the four clusters indicated differing contributions from various sources and processes throughout the study.

We found m/z 44 (CO_2^+) accounted for 10% of AMS-measured OM. AMS-measured sulfate, nitrate, and ammonium contributed almost equally to PM_1, the mass fraction ranging from 8% to 11% on average. Using these three components in an ion balance calculation revealed that the PM_1 positive ions (ammonium) were 20% higher than that of the negative ions (2×sulfate + nitrate). The time series of the positive and negative ions correlated with an r of 0.99, indicating that these ions likely formed and condensed simultaneously, i.e., sulfuric acid and nitric acid interact with ammonia to form ammonium sulfate and ammonium nitrate salts, respectively, followed by condensation of the salts into preexisting particles. High ammonium levels in Bakersfield aerosols are consistent with large ammonia emissions in the SJV [*Sorooshian et al.*, 2008]. The excess ammonium (relative to inorganic sulfate and nitrate) was likely formed by reaction of ammonia with secondary organic acids, such as phthalic acid [*Na et al.*, 2007; *Zhao et al.*, in preparation]. Because the excess

ammonium (relative to inorganic sulfate and nitrate) was ~50% less (in molar concentration) than the FTIR-measured carboxylic acid groups, the aerosol might be slightly acidic.

Elemental ratios (H/C and O/C) measured by the HR-ToF-AMS are illustrated in the Van Krevelen diagram space (Figure 5). The Van Krevelen diagram, displayed as H/C versus O/C, has proven to be useful for describing evolution of atmospheric organic aerosols [*Heald et al.*, 2010; *Ng et al.*, 2011]. For example, conversion of alkane groups (–CH_2–) to carbonyl groups (–C(=O)–) results in a slope of -2 (addition of 1 oxygen and loss of 2 hydrogen atoms), whereas processes that convert alkane groups to hydroxyl groups (–OH) have a slope of 0. Consequently, formation of hydroxycarbonyl or carboxylic acid groups yields a slope of -1. The O/C and H/C in this study ranged from 0.02 to 0.62 and from 1.28 to 1.99, respectively. The points in the Van Krevelen diagram can be grouped into two categories that have different slopes. The relatively high-temperature points have a slope of -0.93, while the slope of the low-temperature points is -1.3 (Figure 5). The distinct slope and temperature for the two categories suggest different chemical and physical processes, including oxidation, condensation, volatilization, and mixing, between daytime and nighttime hours. The measured O/C and H/C in both categories strongly anti-correlated (r = -0.94 to -0.92), suggesting these atmospheric processes changed the O/C and H/C along straight lines. The slopes of -0.93 and -1.3 of the linear fit from this study was similar to the slope of -1.1 observed during the SOAR-1 (Study of Organic Aerosol at Riverside) measurements at Riverside [*Heald et al.*, 2010], but organic aerosol composition at Bakersfield had larger ranges of O/C and H/C than at Riverside (O/C and H/C varied in 0.2-0.5 and 1.4-1.7, respectively, during SOAR-1), which reflects a larger variety of emission sources at Bakersfield.

Compared to PM_1, $PM_{2.5}$ was comprised of a larger fraction of dust components (39%) and a lower fraction of OM (41%) (Figure 2b). Dust components were mainly composed of elements Ca,

Si, Al, and Fe (more likely by their oxides and salts). OM in $PM_{2.5}$ ($OM_{2.5}$) was largely (75%) in submicron particles. The mass difference between OM_1 and $OM_{2.5}$ (55% of OM_1) can be explained by the hydroxyl groups, suggesting that they were associated with larger particles such as dust components (details in following section). Scaling the AMS-measured OM_1 by the $OM_{2.5}$-to-OM_1 ratio measured by FTIR, the calculated AMS $OM_{2.5}$ was 5.6 μg m^{-3}, which is comparable to the $OM_{2.5}$ (~6–7 μg m^{-3}) measured during May-June 1999-2001 at Bakersfield [*Chow et al.*, 2006a].

3.1. Identification of organic mass sources

The main factors contributing to the OM were identified separately from FTIR (PM_1 and $PM_{2.5}$) and AMS measurements using positive matrix factorization (PMF) method (PMF2) [*Paatero and Tapper,* 1994]. PMF procedures are described in the appendices. The factors were identified primarily by their correlations with particle-phase source markers, facilitated by comparisons of factor composition and spectra to factors identified from past studies. Pearson's correlation coefficients (*r*) are used in this study. The correlations were done at the highest time resolution possible with the tracer measurements. The time resolution of the AMS, TAG, and XRF measurements was ~5 min, 1-2 hours, and 3-4 hours, respectively. Subscripts "FTIR," "FTIR2.5," and "AMS" denote the factors commonly identified from FTIR PM_1, FTIR $PM_{2.5}$, and AMS measurements. Detailed factor identification procedures are presented below.

3.1.1. Factors identified from FTIR PM_1 and $PM_{2.5}$ measurements

Five factors were identified from FTIR PM_1 and $PM_{2.5}$ measurements (Appendix A), respectively. The PM_1 and $PM_{2.5}$ factors were similar in factor spectra and compositions (Figure 6a),

indicating nearly the same factors were found for OM_1 and $OM_{2.5}$, which is consistent with the fact that 75% of $OM_{2.5}$ was in OM_1.

The first factor covaried in time with polycyclic aromatic hydrocarbon (PAH) oxidation products 2H-1-benzopyran-2-one, dibenzofuran, 1,8-naphthalic acid/anhydride, benzophenone, 4-hydroxy-9-fluorenone, and phthalic acid/anhydride [*Kautzman et al.*, 2010; *Lee and Lane*, 2009, 2010; *Webb et al.*, 2006] measured by TAG (Table A1a) and phthalic acid (r = 0.7) measured by GC-MS. The factor composition, largely composed of nonacid carbonyl groups (59%), was consistent with oxidation products for aromatic hydrocarbons [*Chan et al.*, 2009; *Jaoui et al.*, 2008; *Russell et al.*, 2011], including PAH and light aromatic compounds. Therefore, this factor was identified as an aromatic SOA factor, representing SOA formed from aromatic hydrocarbons (PAHs and light aromatic compounds) that were likely emitted from gasoline- and diesel-powered vehicles [*Schauer et al.*, 1999; 2002b]. This factor had the greatest contribution (31%) to Cluster 1 particles (Figure 4).

The time series of the second factor correlated most strongly to the time series of C_{11}-C_{14} ketones (undecanone, dodecanone, tridecanone, and tetradecanone) with r of 0.63 to 0.77 for the PM_1 factor and 0.58 of 0.90 for the $PM_{2.5}$ factor (Table A1a and A1b). Note that the enhanced correlations for the $PM_{2.5}$ factor were likely caused by the longer duration of these daily samples, which averaged out any offsets between the time of formation in the gas and particle phases. The long-chain (C_{11}-C_{14}) ketones are suggested to be first-generation alkane oxidation products [*Lim and Ziemann*, 2005, 2009], indicating that this component likely formed from alkane oxidation processes. The factor spectra and functional group compositions were nearly identical to the fossil fuel combustion factors identified from the shipboard measurements near Houston and the ground-based measurements in Southern California, which were suggested to originate from alkane

oxidation processes [*Hawkins and Russell*, 2010; *Liu et al.*, 2011; *Russell et al.*, 2009]. Thus this factor was denoted as the alkane SOA factor.

The third factor from the PM_1 factor analysis correlated (r of 0.65) to pinonaldehyde measured by TAG and 3-Hydroxyglutaric acid (r of 0.5) measured by GC-MS, which are markers for biogenic SOA formed from oxidation of α-pinene [*Hallquist et al.*, 1999; *Claeys et al.*, 2007]. This factor, observed in high concentrations at night, was largely composed of alkane groups (79%) and had the largest mass fraction (8%) of organonitrate groups of all the factors; its composition was consistent with products from α-pinene and β-pinene oxidation by NO_3 radicals [*Hallquist et al.*, 1999; *Wangberg et al.*, 1997]. However, the factor showed a weaker correlation ($r \leq 0.50$) to PAH compounds, suggesting a contribution of primary anthropogenic sources to this factor. Thus, this factor was determined to be the nighttime biogenic SOA factor mixed with less oxygenated hydrocarbon-like anthropogenic emissions and denoted as nighttime OA. The $PM_{2.5}$ nighttime OA factor had similar composition to the PM_1 nighttime OA factor, being dominated by alkane (57%) and organonitrate (17%) groups, but also contained a larger hydroxyl group mass and enhanced correlations to dust elements. Thus, the $PM_{2.5}$ nighttime OA factor likely included a small fraction of dust-related organic components.

The fourth factor of PM_1 correlated (r of 0.6) to the crude oil marker V (vanadium) [*Khalaf et al.*, 1982]. Its IR spectrum was comparable to the "oil combustion/refining" factor spectrum identified from the shipboard measurements near Houston [*Russell et al.*, 2009]. High mass fraction (40% to 65%) of hydroxyl groups indicates that this factor was likely secondarily formed in the atmosphere. The factor was identified as a petroleum operation SOA (PO SOA) factor, representing the oil extraction and refinery operations north and northwest of Bakersfield. The most commonly used method for oil extraction, steam injection, heats crude oil using high-temperature steams. The

heated crude oil has reduced viscosity thereby it is easier to flow [*Fatemi and Jamaloei*, 2011]. The high-temperature steam comes from steam generators, which usually burns crude oil and likely emits V-rich pollutants that include NO_x, CO, and hydrocarbons [*Myers*, 1986]. The corresponding $PM_{2.5}$ factor spectrum was comparable to that of the PM_1 factor (Figure 6a), suggesting that they are the same factors. It is worth noting that V in $PM_{2.5}$ correlated well with dust elements, such as V correlating to Si with an r of 0.96 in $PM_{2.5}$ that is much greater than the correlation of V and Si (r = 0.35) in PM_1, indicating that V in $PM_{2.5}$ was largely from dust sources [*Chow et al.*, 2003], resulting in a weakly negative correlation of the PO SOA factor and V in $PM_{2.5}$. The average concentration of the PO SOA factor peaked in the afternoon, which was consistent with the daytime northwesterly winds from the direction of the oil drilling and the associated petroleum operation activities located to the northwest of the sampling site.

The fifth factor of the PM_1 and $PM_{2.5}$ solutions correlated to the dust elements Si, Al, Ca, and Mg, suggesting that the factor represented organic components associated with dust particles. Double peaks at 2850 cm^{-1} and 2920 cm^{-1}, along with a strong spectral absorption at 3500 cm^{-1}, indicated the existence of repeating methylene and phenol groups, which likely originated from plant wax [*Hawkins and Russell*, 2010] and plant lignin compounds [*Cass*, 1998], respectively. The large fraction of hydroxyl groups (71% to 79%) in this factor was consistent with saccharide-type compounds in plant materials [*Bianchi et al.*, 1993]. Association of the factor with dust and plant components suggests that this factor was likely from vegetative detritus that resuspended with dust particles. This factor was denoted as a vegetative detritus factor and appeared predominately in Cluster 4 particles (Figure 4).

3.1.2. Factors identified from AMS measurements

Six or seven factors were identified from the AMS measurements. The factors in the 6- and 7-factor solutions had similar factor time series and mass spectra (Figures A7 and A8). Compared to the 6-factor solution, an additional factor with high O/C (named as high O/C alkane SOA and discussed below) was identified in the 7-factor solution. We present both the 6- and 7-factor solutions to show the consistency and variability of the PMF factors. The factor m/z spectra, O/C, and H/C are shown in Figure 6c and Figure A7.

The first factor correlated strongly (*r* of 0.81 to 0.90) to particle-phase PAH marker compounds (Table A2a), which are usually coemitted with light aromatic compounds in vehicular exhausts. This factor was characterized by a strong peak at m/z 44 and had an O/C of 0.36, which was higher than the typical O/C of HOA components (~0.10) observed in laboratory and field studies (Table 2) but in the O/C range of 0.20 to 0.60 for SV-OOA (semivolatile OOA) identified from a number of AMS measurements [*Ng et al.*, 2010]. Thus, it suggests that this factor was oxidized but associated with a low oxidation state and, so, was termed low O/C aromatic SOA factor.

Compared to the low O/C aromatic SOA factor, the second factor more closely correlated to long-chain alkanes and alkane SOA components (Table A2a and A2b), suggesting that this factor likely originated from alkane-related sources. The H/C of this factor was 21% higher than the O/C of the low O/C aromatic SOA factor (Figure 6c). This result is consistent with the expectation of a higher H/C for alkane SOA than aromatic SOA: Since alkanes are more saturated than aromatics, alkane SOA is expected to be less oxygenated than aromatic SOA. As the factor O/C (0.27) was higher than expected for primary OM (~0.10) (Table 2), it was identified as a low O/C alkane SOA factor.

The third factor had the highest O/C (0.68-0.72) of all the factors, suggesting that this factor is also secondary but more oxidized than the first two factors—possibly because they formed in later

generations [*Jimenez et al.*, 2009]. The factor spectrum was nearly identical and resembled those of LV-OOA (low-volatility OOA) [*Ulbrich et al.*, 2009]. The time series of this factor correlated most strongly to PAH SOA marker compounds, suggesting that this factor likely represented the oxidation products of aromatic hydrocarbons, including light aromatics and PAH. This factor was identified as a high O/C aromatic SOA factor. The high O/C aromatic SOA factors in the 6- and 7-factor solutions had similar time series, with the former associated with greater mass concentration (Figure A7 and A8).

The fourth factor, the additional factor identified in the 7-factor solution, had similar mass spectra to the high O/C aromatic SOA factor. This factor correlated to both PAH SOA and alkane SOA markers. While the similarity of the factor spectra and correlations with source markers make it difficult to distinguish this factor and the high O/C aromatic SOA factor, their diurnal cycles were different (Figure 7a and 7b). The high O/C aromatic SOA factor peaked at noon and in the evening (2000 hr), while the fourth factor had a broad peak centered at 1500 hr. Distinct diurnal cycles suggested different formation pathways. The high O/C aromatic SOA factor and the fourth factor correlated weakly to long-chain alkane compounds (e.g., heptadecane and octadecane in Table A2b), with the latter having stronger correlations (r of 0.25 to 0.27 for the high O/C aromatic SOA factor and r of 0.37 to 0.38 for the fourth factor). Furthermore, enhanced correlations to alkane compounds of 0.63 to 0.72 resulted from daily-averaged concentration of the fourth factor, but such a large enhancement was not observed under the same conditions for the high O/C aromatic SOA factor (r of 0.37 to 0.46). This suggests that the fourth factor was likely largely linked to alkane-related sources, although contribution of aromatic SOA to this factor cannot be entirely ruled out. Accordingly, the fourth factor was defined as a high O/C alkane SOA factor. The higher H/C ratio of the high O/C alkane SOA compared to the high O/C aromatic SOA is consistent with the expectation

that alkane SOA contains more C-H bonds than aromatic SOA, given that the precursor alkanes are more saturated than aromatics. The high O/C alkane SOA factor accounted for 71% of total alkane SOA, which includes high and low O/C alkane SOA components. This mass fraction is consistent with mechanism simulation that suggests more than 67% of alkane SOA was fourth and higher generation products after 10 hrs of reactions [*Yee et al.*, 2012].

Concentrations of the fifth factor peaked at night (Figure 7c), having been associated with nighttime easterly and southeasterly winds. This pattern compares to that of monoterpenes and their oxidation products (e.g., pinonaldehyde), which suggests contributions from biogenic sources to this factor. The very low O/C (<0.1) also indicates a contribution from primary OM. The mass spectrum was similar to spectrum of HOA (hydrocarbon-like organic aerosol) [*Ulbrich et al.*, 2007; 2009], indicating unoxidized primary anthropogenic sources. As such, this factor was identified as nighttime OA.

The sixth factor had a stronger correlation to V than any other source markers. In addition, the factor's diurnal cycle matched the diurnal cycle of V, suggesting organic components from petroleum operations. The factor was characterized by m/z 43 (87% $C_2H_3O^+$ and 13% $C_3H_7^+$) with an O/C of 0.20, which is larger than 0.10 that is typical for HOA (Table 2). For this reason, this factor is considered secondary rather than primary and termed petroleum operation SOA (PO SOA).

The seventh factor was identified as a cooking organic aerosol (COA) factor for two reasons: The factor spectrum was similar to the previously identified COA factor mass spectra [*Huang et al.,* 2010; *Mohr et al.,* 2012] that were characterized by m/z 27, 41, 55, and 69 with Δm/z of 14, fragments specific for unsaturated fatty acids emitted from cooking activities [*He et al.*, 2010]; and the factor correlated to the food cooking marker hexadecanoic acid (Table A2a and A2b) [*Allan et al.*, 2010; *He et al.*, 2004]. Further, a low O/C (0.05) suggests that this factor was simply

recondensed cooking oils from local sources that had undergone little or no oxidation in the atmosphere.

We have focused on the 7-factor solution in the following discussions since it may suggest differences in the oxidation products formed with time.

3.1.3. Comparison of FTIR (PM_1 and $PM_{2.5}$) and AMS factors

The FTIR PM_1 and $PM_{2.5}$ factors were similar in compositions but differed in mass. Overall, the reconstructed ratio of OM_1 (the sum of PM_1 factors) to $OM_{2.5}$ (the sum of $PM_{2.5}$ factors) was 0.85, 13% higher than the actual measured $OM_1/OM_{2.5}$ of 0.75. The greatest difference between PM_1 and $PM_{2.5}$ factors was observed in the vegetative detritus factor, the OM being 55% higher in $PM_{2.5}$. This difference was largely (92%) attributed to hydroxyl groups (Figure 8), which likely originated from plant materials and then mixed with dusts to result in a larger fraction with bigger particles. The aromatic SOA and alkane SOA factors were 12% and 33% higher, respectively, in $PM_{2.5}$, with the alkane groups accounting for the largest difference in each pair of factors. As aforementioned, the nighttime $OA_{FTIR2.5}$ likely had some dust fractions, indicating incomplete separation of this factor from $PM_{2.5}$ samples, so nighttime $OA_{FTIR2.5}$ was slightly smaller than nighttime OA_{FTIR}. The PO SOA_{FTIR} was higher in the alkane group mass and lower in the hydroxyl group mass compared to the PO $SOA_{FTIR2.5}$, resulting in comparable total OM between the two factors.

The factors identified from AMS measurements show consistencies and differences to the factors derived from FTIR measurements. The low O/C and high O/C aromatic SOA_{AMS} factors, taken together, correlated to aromatic SOA_{FTIR} with an r of 0.73 (Figure A9). The sum of the low and high O/C aromatic SOA_{AMS} factors accounted for 25% of OM, consistent with the OM fraction (24%) of the aromatic SOA_{FTIR} factor (Figure 6b). Similarly, good correlation (r = 0.74) was

observed for the sum of the low and high O/C alkane SOA_{AMS} factors and the alkane SOA_{FTIR} factor, each of which accounted for 41% to 42% of the OM. The difference between the FTIR and AMS high O/C factors can be seen from Figure 7: The diurnal cycle of the alkane SOA_{FTIR} is more similar to the low O/C alkane SOA_{AMS} than the total alkane SOA_{AMS}, and the diurnal cycle of the aromatic SOA_{FTIR} is more similar to the high O/C aromatic SOA_{AMS} than the total aromatic SOA_{AMS}. The difference in diurnal cycles may result from the scatter in their correlations as well as the uncertainties of the measurements and factorization. The PO SOA_{AMS} and PO SOA_{FTIR} (correlated with an r of 0.52) contributed 13% to 14% of OM. The campaign-average mass fractions of NOA_{FTIR} and NOA_{AMS} factors were 10% to 13%, with higher fractions of 21% to 24% during 0000–0600 hr. The difference between NOA_{FTIR} and NOA_{AMS} is that NOA_{FTIR} includes a substantial contribution of organonitrate functional groups (and a higher associated O/C from them) whereas the organonitrate mass was not distinguishable from the inorganic nitrate in the AMS. However, the AMS measurements were likely more sensitive to smaller particles that may have included a larger fraction of HOA that was not resolved by the FTIR PMF. These differences likely resulted in the relatively low correlation (r = 0.52) between NOA_{FTIR} and NOA_{AMS}. The vegetative detritus factor (10% OM) was identified only from FTIR measurements, likely because this component was mixed with dust in particles of 500 nm and larger, which have reduced transmission efficiency in the AMS aerodynamic lens and could not be detected effectively by the AMS. The COA_{AMS} (7% OM) was not found in the FTIR measurements. This difference between the AMS and FTIR factors may be due to COA components mainly existing as small particles (100–200 nm, as discussed in Section 4.3), where the small-particle collection efficiency of 1-μm Teflon filters drops off [*Liu and Lee,* 1976] and the small mass in this size range were insufficient for detection.

In summary, factors identified from PM_1 and $PM_{2.5}$ FTIR and AMS measurements showed good agreement in source type, mass fraction, and time series. The missing vegetative detritus factor for the AMS measurements and COA factor for the FTIR measurements contributed 10% of OM in PM_1, and both were within the expected uncertainties for each technique. The high O/C aromatic and alkane SOA factors were mathematically independent ($r < 0.7$) but their mass spectra were chemically similar (cosine similarity was 0.99) (cosine similarity is defined as cosine of the angle between two vectors [*Stein and Scott,* 1994], values ranging from 0 to 1, with higher values indicating higher similarity), thus source markers are needed to justify separation of these factors; in contrast, the FTIR aromatic and alkane SOA factors were mathematically independent ($r < 0.5$) and their IR spectra were chemically different (e.g., cosine similarity was 0.3), thus source markers are not needed to justify separation of the FTIR factors but provide a link to their precursors. The FTIR and AMS factors suggested that 80% to 90% of OM was secondary, even those measurements conducted near emission sources. Of these SOA components, aromatic and alkane SOA factors accounted for 65% of OM, indicating fossil fuel combustion that was likely from motor vehicles is the largest source at Bakersfield. This finding is consistent with previous source apportionment studies at Bakersfield [*Hamilton et al.*, 2004; *Kleeman et al.*, 1999; *Schauer and Cass*, 2000]. Also from these studies, wood combustion was identified as a significant source only in winter, likely because residential heating (the main source of wood burning) was not in use during the early summer period [*Chow et al.*, 2006b]. However, the petroleum operation, categorized as having near-zero emissions in recent source inventory in southern SJV (Table A3), should be added given its contribution of 14% OM.

3.2. Identification of single-particle types

3.2.1 Single-particle NEXAFS spectra

Single-particle X-ray spectra (80 particles) were categorized into three major groups based on their spectroscopic similarities (Figure 9). To gain further insight into their source types, each group was compared to single-particle X-ray spectra for each of the 14 types of particles identified by *Takahama et al*. [2007]: Group I particles showed strong carboxylic acid group absorption at 288.7 eV. Their particle spectra were comparable to type "a" particles, likely formed from atmospheric processing, which suggests the group's secondary origins. Group II spectra were characterized by strong absorption at 285.0 eV due to sp^2-bonding of soot or black carbon. Since these particles resembled Takahama's "strongly aromatic aerosols" (e.g., type "h" particles) (Figure 9b), defined as particles that have strong absorption at 285 eV due to sp^2 carbon bonding, diesel exhaust was the likely origin. Group III particles showed no significant peaks for organic functional groups. The lack of a C=C peak at 285.0 eV and a C-OH peak at ~287.0 eV, which are characteristic for biomass-burning type particles, essentially excluded the possibility of Group III having a biomass burning source [*Braun*, 2005; *Tivanski et al*., 2007], although the C=C peak for such particles is relatively smaller compared to that of diesel soot particles. Furthermore, high absorbance seen in the K region (at 297.4 and 299.9 eV) was consistent with dust sources, the likely origin of Group III's particles.

3.2.2 Single-particle mass spectra

Single-particle mass spectra for 147,357 particles were clustered (detailed in *Liu et al*. [2012]) to reveal three single-particle clusters: Cluster I mass spectra were characterized by m/z 44 and were comparable to LV-OOA spectra in the AMS database [*Ulbrich et al*., 2009]. Cluster II particles had strong m/z 43 signals, and their spectra resembled those of SV-OOA components.

Cluster III spectra were characterized by m/z 27, 29, 41, 55, 57, and 69, which were typical for hydrocarbon type aerosols (m/z 29, 57) or cooking organic aerosols (m/z 27, 41, 55, 69). This suggested that Cluster III particles likely originated from mixed local primary sources.

3.2.3 Single-particle types compared with bulk source types

The "secondary" (Group I), "diesel exhaust" (Group II), and "dust" (Group III) particle types resulting from single-particle X-ray spectra broadly matched the major source types identified from bulk particle functional group factor analysis. Secondary particles accounted for 44% of total measured particles, which was consistent with bulk particle analysis that suggested SOA was the major component of OM. Similarly, the "high m/z 44" (Cluster I), "high m/z 43" (Cluster II), and "mixed" (Cluster III) particle types derived from single-particle mass spectra analysis matched the major source types from the bulk particle mass spectra factor analysis. Taken together, the high m/z 44 and m/z 43 types accounted for 56% of identified particles, both by number and mass. Specifically, the group-average high m/z 44 single-particle spectrum correlated to the mass spectra for the high O/C alkane and aromatic SOA components with an r of 0.96 and 0.92, respectively. High spectral correlations were also observed for the high m/z 43 type particles that correlated to the low O/C alkane SOA with $r = 0.96$ and the mixed-type particles that correlated to COA, PO SOA, and nighttime OA with $r = 0.86$, 0.76, and 0.70, respectively. Agreement of single and bulk particle types speaks to the ubiquity of SOA in fine OM at Bakersfield.

4. Discussion

The SOA components, which were derived from factor analysis, differed in mass, chemical composition, and diurnal cycle (summarized in Table 3), suggesting they were produced via distinct

oxidation processes and likely favored by specific meteorological conditions. In this section, we compare the SOA components and discuss the underlying processes that likely led to their formation. Special attention is given to alkane SOA, aromatic SOA, and nighttime OA; the first two prevailed during daytime, and the last was a significant constituent at night. In addition, we discuss size distributions of SOA components, which confirm the source identification and indicate the likely formation process.

4.1. **Contrasting formation of alkane and aromatic secondary organic aerosol components**

The diurnal cycle for high O/C alkane SOA_{AMS} was consistent over the course of the study, with concentrations peaking in the afternoon for 74% of the 45-day campaign (Figure 10a). The average diurnal cycle resembled that of the odd oxygen ($O_3 + NO_2$), and the factor mass fraction correlated to odd oxygen with an *r* of 0.70 (higher temperature associated with larger odd oxygen mixing ratios and greater factor mass fractions) (Figure 10b), suggesting O_3 either played an important role in its formation or was coproduced with alkane SOA from similar precursors on similar time scales. Good correlation of alkane SOA to odd oxygen were also found by recent model simulations even without a role for O_3 in the oxidation of alkanes [*Pye and Pouliot*, 2012]. The alkane SOA_{FTIR} factor mole composition of 0.11/0.04/0.00/0.86 among carboxylic acid/hydroxyl/nonacid carbonyl/alkane groups compared well to C_{12} alkane oxidation products, with mole fractions of 0.12/0.13/0.02/0.73 for the carboxylic acid/hydroxyl/nonacid carbonyl/alkane groups [*Russell et al.,* 2011]. This composition was inferred from a two-step oxidation pathway: 1) gas-phase alkane oxidation by OH radicals to form particle-phase dihydrofuran; and 2) evaporation of dihydrofuran followed by O_3 oxidation, forming carboxylic acid and alkane group dominated products [*Russell et al.*, 2011]. The products from each step likely represented first and higher

generation SOA components, respectively [*Lim and Ziemann*, 2005, 2009]. Therefore, that the high O/C alkane SOA_{AMS} factor correlated with odd oxygen indicated second or higher generation products from alkane oxidation. Neither the low O/C alkane SOA_{AMS} factor nor the sum of the high and low O/C alkane SOA_{AMS} factors (correlating to the alkane SOA_{FTIR} factor, $r = 0.74$) correlated to odd oxygen, indicating that the low O/C alkane SOA_{AMS} factor may have been associated with the first step of oxidation which happened faster than O_3 formation or for which O_3 was not required.

For the diurnal cycle of the high O/C aromatic SOA_{AMS} factor, no consistent pattern was identified. Day-to-day variation likely resulted from the variety of the aromatic species emitted from vehicular emissions, including light aromatic hydrocarbons and polycyclic aromatic hydrocarbons (PAHs), the quantities of which are highly dependent on combusted fuels [*Richter and Howard*, 2000]. In contrast, alkane compounds were relatively simple in their structure and could readily be grouped into linear, branched, and cyclic alkane classes, with SOA products fairly similar among these classes [*Lim and Ziemann*, 2009]. The mass yield of aromatic compounds may vary significantly as was found in SOA yields from naphthalene, which ranged from 2% to 22% [*Shakya and Griffin*, 2010] and from 19% to 74% [*Chan et al.*, 2009] under comparable experimental conditions (i.e., OH concentration, initial hydrocarbon concentration, and initial NO_x-mixing ratio). This indicated that yields of aromatic hydrocarbons were extremely sensitive to environmental conditions. In addition, SOA components from PAH oxidation have been shown to be sensitive to NO_x mixing ratios, with ring-opening compounds being major products under high NO_x conditions and ring-retaining compounds formed under low NO_x conditions [*Kautzman et al.*, 2010].

The variety of the aromatic compounds, sensitivity of their yields to the environmental conditions, and dependence of their oxidation products on NO_x, likely contributed to the variability of the diurnal cycle for the high O/C aromatic SOA_{AMS} factor. This factor's mass fraction (or mass

concentration) did not correlate to odd oxygen (Figure 10), suggesting that O_3 played a minor role (if any) in its formation. The aromatic SOA_{FTIR} factor, which likely represented the average composition of a variety of aromatic SOA components, was largely composed of nonacid carbonyl groups (59%), which was consistent with the OH radical oxidation products for aromatic precursors, a majority of which contain ketone groups [*Esteve et al.*, 2003; *Lee and Lane*, 2009; *Lee and Lane*, 2010; *Wang et al.*, 2007; *Webb et al.*, 2006]. The similarity of the aromatic SOA_{FTIR} factor to OH oxidation products for aromatic hydrocarbons suggests that OH was the main oxidant that oxidized primary aromatic compounds to their SOA products. This observation is consistent with previous kinetic studies that showed that aromatic hydrocarbons primarily react with OH radicals in the atmosphere [*Kwok et al.*, 1994].

The functional group composition of alkane and aromatic SOA_{FTIR} factors are significantly different from the biogenic SOA factors identified in previous studies. For example, the biogenic SOA factor identified from Whistler, a remote forested site, has mole fractions of 0.44/0.25/0.16/0.10 for alkane, hydroxyl, nonacid, and carboxylic groups [*Russell et al.*, 2011], i.e. the Whistler biogenic factor has a smaller alkane group fraction and a larger hydroxyl group fraction than the alkane SOA_{FTIR} factor. The biogenic SOA factor also has a smaller fraction of nonacid carbonyl groups than the aromatic SOA_{FTIR} factor.

4.2. **Nighttime formation of biogenic secondary organic aerosols**

While high O/C alkane and aromatic SOA_{AMS} components peaked during the day, high concentrations (20% to 52% OM) of the nighttime OA factors were observed at night (Figure 11a). The nighttime OA_{FTIR} factor, although influenced by primary anthropogenic sources, had significant signatures of biogenic SOA. The factor composition of alkane (57% to 79% OM), organonitrate (8%

to 17% OM), and nonacid carbonyl groups (0% to 8% OM) was chemically similar to α-pinene and β-pinene SOA produced by NO_3 radical oxidation. These SOA components typically comprise 63% to 68% alkane groups, 8% to 26% organonitrate groups, and 2% to 24% nonacid carbonyl groups [*Hallquist et al.*, 1999; *Wangberg et al.*, 1997]. Therefore, the SOA fraction of the nighttime OA_{FTIR} factor likely formed via NO_3 radical oxidation. Supporting this argument is the correlation (r = 0.5) of nighttime OA_{FTIR} with nitrated organosulfates (e.g., $C_{10}H_{16}NO_7S^-$, $C_9H_{14}NO_8S^-$, and $C_{10}H_{16}NO_{10}S^-$ ions measured by UPLC/ESI-HR-Q-TOFMS), the most abundant organosulfate compound class (observed at the Bakersfield site) that is likely produced from NO_3 radical oxidation of α-pinene and limonene-like monoterpenes (e.g., myrcene) under dark conditions [*Surratt et al.*, 2008].

As described in Section 3.1, easterly downslope winds prevailed at night, which likely carried biogenic VOCs to the sampling site. Biogenic VOCs (e.g., terpenes) typically contain one or more carbon-carbon double bonds, highly chemically active and readily oxidized typically by O_3 and NO_3 radicals under nighttime conditions. While some background O_3 was still detected at night (~10 ppb), no correlation was observed between the nighttime OA_{FTIR} factor and the O_3 concentration, indicating O_3 may not play a major role in formation of nighttime OA_{FTIR}. However, background O_3 could react with NO_2 to generate NO_3 radicals and could also convert NO to NO_2 to prevent loss of NO_3 radicals by reacting with NO. The nighttime OA_{FTIR} factor correlated to nighttime NO_x (Figure 11b), which is the precursor of NO_3 radicals, confirming that nighttime OA_{FTIR} was likely formed by NO_3 radical oxidation. *Rollins* et al. [2012] estimated that 1/3 of OM increase at night was accounted for by organonitrate group-containing molecules, which is consistent with the nighttime formation mechanism of the nighttime OA_{FTIR} factor. Moreover, the nighttime OA_{FTIR} factor accounted for 50% to 80% of the observed organonitrate group mass, which is consistent with an expected higher

organonitate group yield from NO_3 oxidation reactions than that from OH radical and O_3 oxidation processes. Additionally, lower concentrations of nighttime OA_{FTIR} were associated with high RH (Figure 11b), which is consistent with the loss of NO_3 radicals under high RH conditions (shifting the reaction $NO_3 + NO_2 = N_2O_5$ to the right through N_2O_5 uptake under high RH). Although alkane and aromatic hydrocarbons coexisted with biogenic VOCs at night, their oxidation rate constants for NO_3 radicals were typically less than 10^{-16} and 10^{-15} cm^3 $molecule^{-1}$ s^{-1}, respectively [*Atkinson and Arey*, 2003]. These rate constants were 10^3 to 10^6 times smaller than rate constants of the biogenic hydrocarbons (oxidation by NO_3 radicals), which typically ranged from 10^{-10} to 10^{-12} cm^3 $molecule^{-1}$ s^{-1} [*Atkinson and Arey*, 2003]. Therefore, NO_3 radicals mainly reacted with biogenic VOCs, forming biogenic SOA components with organonitrate functional groups in the nighttime atmosphere.

Compared to the biogenic SOA factors identified at Whistler (British Columbia, at 1020 m above sea level) [*Schwartz et al.*, 2010], the nighttime OA_{FTIR} factor had significantly larger contribution of organonitrate groups. This difference likely arises from distinct oxidation conditions: O_3 or OH radical oxidation under low NO_x (1.5 ppb) at Whistler and NO_3 radical oxidation under high NO_x (15 ppb at night) at Bakersfield.

4.3. **Insights of SOA formation from factor size distribution**

Time series of the OM factors were correlated to time series of OM particle size sections ($OM_{30\text{-}100}$, $OM_{100\text{-}200}$, $OM_{200\text{-}300}$, $OM_{300\text{-}400}$, $OM_{400\text{-}500}$, $OM_{500\text{-}600}$, $OM_{600\text{-}700}$, $OM_{700\text{-}800}$, $OM_{800\text{-}900}$, $OM_{900\text{-}1000}$) derived from the AMS TOF mode measurements, resulting in a set of correlation coefficients for each factor. The square of the correlation coefficient (r^2) between an OM section and a factor represents the fraction of variability of an OM section that could be explained by variability of the factor [*Rodgers and Nicewander*, 1988]. The mean and variability (standard deviation) for the

OM sections were comparable (Table 4), suggesting that most of the OM concentration was controlled by OM variability. Similarly, the factor concentration was controlled by variability in the factor concentration. Therefore, high r^2 between an OM section and a factor suggests that the mass of the OM section was likely accounted for by the factor, i.e., a majority of the factor mass likely distributed in the same size range as the OM section. For this reason, the r^2 distribution (versus size) for each factor represents the factor mass size distribution to a great extent. Factor mass size distribution estimated from this approach can be validated by size distribution estimated from a marker-based method (e.g., size distribution of m/z 44 represents size distribution of SOA), which has proven to be approximately accurate [*Ulbrich et al.,* 2012].

Variability of OM in 200- to 500-nm-sized particles was accounted for by the high O/C alkane and aromatic SOA factors (Figure 12a), suggesting that the high O/C factors peaked in 200- to 500-nm size range. Mass of fragment CO_2^+ (m/z 44), largely accounted for by high O/C alkane SOA (55%) and high O/C aromatic SOA (30%) factors, peaked in the 150- to 500-nm size range, which agreed well with r^2 distributions for the two high O/C factors. These peak size ranges are comparable to those for the OOA factor identified from Mexico City measurements using 3-D factorization analysis [*Ulbrich et al.,* 2012]. Oxidized components enriched in 200- to 500-nm-sized particles typically form by condensation of gas-phase secondary organic species, because these particles provide most of the surface area that mass transfer mainly occurs in this size range [*Seinfeld and Pandis*, 2006]. In addition, oxidized components in 200- to 500-nm-sized particles are often associated with high O_3 mixing ratios [*Alfarra et al.,* 2004; *Liu et al.,* 2008; *Zhang et al.,* 2005], suggesting that the high O/C factors were produced during photochemical processes. Note that r^2 size distributions of the high O/C factors shifted 50 nm (daytime) and 20 nm (nighttime) towards larger sized particles compared to the m/z 44 size distribution, a difference likely caused by variation

of non-m/z 44 fragments in the high O/C factors that underwent different atmospheric processes compared to the processes experienced by fragment m/z 44. Larger daytime shifts reflect more complex processes, which could also explain the shoulder at 600- to 900-nm of daytime r^2 distributions. Low O/C alkane and aromatic SOA factors had similar r^2 size distributions compared to those for the high O/C factors, except the low O/C alkane SOA was broadly distributed (250 to 900 nm) (Figure 12b). This likely resulted from the low O/C alkane SOA's temperature-driven condensation at night [*Lanz et al.,* 2007; *Ng et al.,* 2010], as daily temperatures fluctuated widely (10–20 ºC). r^2 of another low O/C factor, PO SOA, peaked in the 100- to 200-nm size range. Fragment m/z 43 (72% $C_2H_3O^+$ and 28% $C_3H_7^+$) was representative of low O/C factors. Daytime size distribution of m/z 43 peaked in the 100- to 600-nm size range, as was consistent with size distributions of low O/C alkane SOA, low O/C aromatic SOA, and PO SOA factors. A distinct mode of m/z 43 at 400- to 700-nm occurred at night, likely a contribution of $C_3H_7^+$ from primary emissions.

The size distribution of r^2 of the nighttime OA factor peaked in the 400- to 700-nm size range at night (Figure 12c). This size range largely overlapped the larger mode in nighttime size distribution of m/z 57, which was expected because 60% of m/z 57 mass fragment was attributed to the nighttime OA factor. The 400- to 700-nm mode was not present in the size distribution of SOA components (such as fragment m/z 44, sulfate, and nitrate, Figure 12), suggesting that nighttime $OM_{400\text{-}700}$ was likely associated with primary emissions. A likely primary source was vehicular emission. Although fresh exhaust particles are typically smaller than 100 nm, a mode at 550 nm was observed from chase studies using AMS [*Canagaratna et al*., 2004]. In addition, *Kleeman et al*. [2009] attributed a significant mass of particles (560–1000 nm) to diesel fuel and gasoline combustion sources at the same site. Another source of particles in this mode could be vegetative

detritus, which likely existed as large particles (Section 3.1). SOA produced at night (e.g., biogenic SOA) could condense on large primary particles to form internal mixtures. Therefore, the nighttime OA factor, which included a mixture of primary and secondary signatures, likely represented a mixture of primary hydrocarbons and condensed secondary biogenic SOA components formed by NO_3 oxidation.

The size distribution of r^2 for the COA factor peaked in 100- to 200-nm, a size range consistent with primarily emitted particles from meat charbroiling and frying activities [*Hildmann et al.*, 1991; *Wallace et al.*, 2004; *Kleeman et al.*, 2009; *Allan et al.*, 2010; *Zhang et al.*, 2007], which agreed with the low O/C (0.04) for this factor.

5. Conclusions

Summertime measurements suggested that organic mass comprised the major component of fine aerosol particles at Bakersfield in the San Joaquin Valley. On average, OM in PM_1 and $PM_{2.5}$ was 2.42 and 3.23 μg m^{-3}, respectively. PMF analysis was applied to the FTIR and AMS measurements, resulting in very high agreement between the two sets of independently-derived factors, both of which suggested that SOA components accounted for 80% to 90% of fine particle OM. The high O/C AMS factors were chemically similar, so that external source marker were needed to link them to specific sources; whereas the FTIR factors had distinct infrared spectra that could be used as references for future studies when source marker measurements are not available. Among the PMF-derived components, vehicular emission oxidation products, including the alkane and aromatic SOA factors, constituted 65% OM, whereas nighttime organic aerosols (the nighttime OA factor), a mixture of POA and SOA that likely originated from biogenic emissions, accounted for a relatively small fraction on average (10% OM), although it was higher at night (20% OM).

Potential formation mechanisms of the SOA components were discussed. Anthropogenic SOA components mainly formed during daytime. The alkane SOA consisted of alkane and carboxylic acid groups, consistent with the composition expected for oxidation products of C_{12}-C_{25} alkanes. Furthermore, organic mass fraction of alkane SOA covaried and correlated with odd oxygen, providing evidence for the ozone-driven formation of alkane SOA, a mechanism derived from laboratory studies. In contrast, aromatic SOA did not correlate with ozone. This component was largely composed of nonacid carbonyl groups, which is consistent with oxidation products formed from OH radical-driven reactions for aromatic hydrocarbons and, therefore, indicates formation by this process. The nighttime organic aerosol component accounted for 50% to 80% of organonitrate group mass during the project; the secondary fraction of nighttime OA likely formed from oxidation of biogenic precursors (e.g., terpenes) by nitrate radicals during nighttime hours.

Not only did anthropogenic and biogenic SOA components differ in composition, they also differed in size: namely, oxidized alkane and aromatic SOA components was largely distributed in 200- to 500-nm-sized particles, suggesting that they were formed from condensation of gas-phase oxidation products, while biogenic SOA was in 400- to 700-nm-sized particles at night, likely due to condensation of biogenic SOA on large primary particles.

We also identified aerosols likely emitted from local petroleum operations and cooking activities, which were likely in particles smaller than 200 nm. Though these sources were negligibly small in the emission inventory for the Bakersfield site, they accounted for 13% and 7% of the PM_1 organic mass, respectively.

Overall, this work demonstrates that OOA components identified from factor analysis can be linked to SOA formed by different oxidants and precursors mainly from gasoline and diesel fuel combustion emissions with minor contributions from petroleum operation and biogenic sources. In

addition, these SOA components were enriched at particular sizes. We conclude that SOA accounts for a major fraction of summertime OM, even in areas close to urban sources. This result provides a benefit to the SJV community because it identifies the need for regulating vehicular emissions as the largest source of PM_1 in summertime.

Appendix

PMF was applied to FTIR and AMS measurements to identify sources that contributed to OM. Solutions were grouped by number of factors, rotational values, and seed values. Mathematical criteria were used to evaluate PMF model fitting and facilitate solution selection. Detailed factor extraction procedures are presented as follows.

Appendix A: Factor extraction of FTIR PM_1 and $PM_{2.5}$ samples

PMF was applied to PM_1 (228 samples) and $PM_{2.5}$ (46 samples) mass-weighted FTIR spectra, respectively. Data matrices were composed of infrared absorptions, and scaling factor matrices were calculated from baselining errors using an automated algorithm described in *Russell et al.* [2009]. Robust mode was used (i.e., outliers were downweighted during fitting processes). "FPEAKs" (rotational values) of □1, □0.8, □0.6, □0.4, □0.2, and 0 were tested, resulting in nearly identical factors. Minimum $Q/Q_{expected}$, a mathematical diagnostic for PMF fitting (*Paatero et al.*, 2002), corresponded to FPEAK of 0 in PM_1 and $PM_{2.5}$ factor analysis results (Figure A1). Therefore, factors with FPEAK of 0 were selected to represent solutions. To investigate consistency of the solutions, seed values of 0 to 100 (varied by 10) were tested. For each of the PM_1 and $PM_{2.5}$ measurements, factor spectra and strengths derived using different seed values correlated with *r* of 0.99 or better, demonstrating robustness of the factors.

When exploring 2- to 8-factor solutions, $Q/Q_{expected}$ decreased with increasing factor numbers (Figure A2), indicating that the measured spectra were a better fit with more factors. However, too many factors may result in "factor spitting" [*Ulbrich et al.*, 2009], and the "correct" number of factors should be evaluated on the basis of the physical meaning of the solutions. Therefore, solutions with $Q/Q_{expected}$ close to 1 (theoretical value of ideal solution) are not necessarily the best

solutions. The 5-factor solution was chosen for PM_1 factor analysis because one or more factors (≥ 12% OM) with specific source signatures were not identified from the 2-, 3-, and 4-factor solutions, and small (≤ 7% OM) factors (i.e., unidentified factors) that did not correlate to any source markers were generated when 6 or more factors were applied. For $PM_{2.5}$ factor analysis, a unique factor with 15% (mass fraction) organonitrate groups was not identified in solutions with less than 6 factors, and factors with unrealistic infrared spectra were found in solutions with more than 6 factors. Therefore, the 6-factor solution was selected for $PM_{2.5}$ measurements. In this solution, 2 factors had similar chemical compositions and correlated in time with an *r* of 0.60, indicating they were likely split from one source [*Ulbrich et al.*, 2009]. The 2 correlated factors were combined into 1 factor (mass of the combined factor equals sum of factor masses used in combination), resulting in 5 linearly-independent factors, which explained the same degree of OM variability as the 6 factors prior to factor recombination.

The normalized sum of residuals (sum of infrared absorptions for each sample) fluctuated around 0, with amplitude less than 7% for the PM_1 and $PM_{2.5}$ solutions (Figures A3a and A3b). No correlation was observed for the normalized sum of residuals and OM. Scaled residuals showed no evidence of characteristic functional group absorptions (Figures A4a and A4b). Random patterns of the normalized sum of residuals and scaled residuals suggested that residuals represented fitting noises and input matrices were well fit.

Appendix B: Factor extraction of AMS measurements

PMF was applied to high-resolution mass spectra (V mode) measured by the HR-ToF-AMS. Data and error matrices were prepared using standard AMS data processing procedures (PIKA version 1.09) with Igor Pro 6 (Wavemetrics, Inc.). To appropriately weigh the data points, variables

(time series of m/z) with S/N smaller than 0.2 were omitted from the analysis. Weak points (S/N between 0.2 and 2) and CO_2^+-related ions (m/z 16, 17, 18, 28, and 44) were downweighted by a factor of two [*Paatero and Hopke*, 2003; *Ulbrich et al*., 2009]. Robust mode was used in the fitting procedure. FPEAKs of □1, □0.8, □0.6, □0.4, □0.2, and 0 were investigated. Factors with an FPEAK of 0 corresponded to the minimum $Q/Q_{expected}$ (Figure A1), so they were selected to represent the solutions. Seeds of 0 to 100 (varied by 10) were tested, resulting in two groups of solutions: Group I was composed of solutions with seeds 10, 20, 30, 50, 70, 80, and 100, and Group II comprised solutions with seeds 0, 40, 60, 90. Within each group, the factors had nearly identical mass spectra and strengths (with $r \geq 0.94$ and $r \geq 0.99$ for Group I and Group II factors, respectively). Comparing Group I with Group II, factors had similar factor mass spectra ($r \geq 0.90$) but different factor strengths, resulting in different factor time series. The factors in Group I were more linearly independent and correlated better to the source markers than Group II factors. For example, F_1 and F_7 in the 7-factor solution in Group II correlated with an r of 0.82, and F_1 and F_7 did not significantly correlate to any group of source markers (Table A2c). Therefore, the Group I factors were preferred in the PMF solutions.

Solutions with 2 to 8 factors were investigated to determine the optimal number of factors. For solutions with 5 or fewer factors, one or more physically meaningful factors with significant masses (> 15% OM) were missing; when 8 factors were applied, small (< 6% OM) and highly correlated (r of 0.80) factors were generated, indicating that some factors split into smaller factors that correlated in time, which could not be identified. Consistent factors were identified in the 6- and 7-factor solutions, with the 7-factor solution having an additional factor with high O/C (see Section 3.1.2 for detailed description). We present both the 6- and 7-factor solutions to show the consistency and variability of the solutions. The summed residual of the 6- and 7-factor solution fluctuated

around 0, with an absolute amplitude smaller than 0.2 μg m^{-3} (Figure A3c)—much smaller than OM variability of 2.2 μg m^{-3}. The pattern of scaled residuals resembled random noise (Figure A4c), indicating the measurement was well fit by the factors.

Acknowledgments

The authors appreciate California Air Resources Board (CARB) for funding this work (contract 09-328). We thank the CalNex-SJV research team for the cooperation and contribution to this paper. Particularly we acknowledge Professor Ron Cohen at UC Berkeley and his group members Sally Pusede and Ellie Browne for providing the NO_x measurements, and Professor William Brune at Pennsylvania State University for providing OH measurements. The authors are also grateful to John Karlik and the Kern County University of California Cooperative Extension staff for their generous help during the measurements. The statements and conclusions in this paper are those of the researchers (contractor) and not necessarily those of CARB. The mention of commercial products, their source, or their use in connection with material reported herein is not to be construed as actual or implied endorsement of such products.

References

Ahlm, L., et al. (2012), Formation and growth of ultrafine particles from secondary sources in Bakersfield, California, *J. Geophys. Res.,* 117, D00V08, doi: 10.1029/2011JD017144.

Aiken, A. C., et al. (2008), O/C and OM/OC ratios of primary, secondary, and ambient organic aerosols with high-resolution time-of-flight aerosol mass spectrometry, *Environ. Sci. Technol.*, 42(12), 4478-4485.

Alfarra, M. R., et al. (2004): Characterization of urban and rural organic particulate in the lower fraser valley using two aerodyne aerosol mass spectrometers, *Atmos. Environ.*, 38(34), 5745-5758.

Allan, J. D., P. I. Williams, W. T. Morgan, C. L. Martin, M. J. Flynn, J. Lee, E. Nemitz, G. J. Phillips, M. W. Gallagher, and H. Coe (2010), Contributions from transport, solid fuel burning and cooking to primary organic aerosols in two UK cities, *Atmos. Chem. Phys.*, *10*(2), 647-668.

Atkinson, R. and J. Arey (2003), Atmospheric degradation of volatile organic compounds, *Chem. Rev.*, 103(12), 4605-4638.

Bianchi, G., A. Gamba, R. Limiroli, N. Pozzi, R. Elster, F. Salamini, and D. Bartels (1993), The unusual sugur composition in leaves of the resurrection plant myrothamnus-flabellifolia, *Physiologia Plantarum*, 87(2), 223-226.

Braun, A. (2005), Carbon speciation in airborne particulate matter with C (1s) NEXAFS spectroscopy, *J. Environ. Monit.*, *7*(11), 1059-1065.

Canagaratna, M. R., et al. (2004), Chase studies of particulate emissions from in-use New York City vehicles, *Aerosol Sci. Technol.*, 38(6), 555-573.

Canagaratna, M. R., et al. (2007), Chemical and microphysical characterization of ambient aerosols with the aerodyne aerosol mass spectrometer, *Mass Spectrometry Reviews*, *26*(2), 185-222.

Cass, G. R.: Organic molecular tracers for particulate air pollution sources, Trac-Trends in *Analytical Chemistry*, 17(6), 356-366, 1998.

Chan, A. W. H., K. E. Kautzman, P. S. Chhabra, J. D. Surratt, M. N. Chan, J. D. Crounse, A. Kuerten, P. O. Wennberg, R. C. Flagan, and J. H. Seinfeld (2009), Secondary organic aerosol formation from photooxidation of naphthalene and alkylnaphthalenes: implications for oxidation of intermediate volatility organic compounds (IVOCs), *Atmos. Chem. Phys.*, *9*(9), 3049-3060.

Chow, J. C., J. G. Watson, Z. Q. Lu, D. H. Lowenthal, C. A. Frazier, P. A. Solomon, R. H. Thuillier, and K. Magliano (1996), Descriptive analysis of PM2.5 and PM10 at regionally representative locations during sjvaqs/auspex, *Atmos. Environ.*, 30(12), 2079-2112.

Chow, J. C., J. G. Watson, L. L. Ashbaugh, and K. L. Magliano (2003), Similarities and differences in PM10 chemical source profiles for geological dust from the San Joaquin Valley, California, *Atmos. Environ.*, 37(9-10), 1317-1340.

Chow, J. C., J. G. Watson, D. H. Lowenthal, L. W. A. Chen, and K. L. Magliano (2006a), Particulate carbon measurements in California's San Joaquin Valley, *Chemosphere*, *62*(3), 337-348.

Chow, J. C., L. W. A. Chen, J. G. Watson, D. H. Lowenthal, K. A. Magliano, K. Turkiewicz, and D. E. Lehrman (2006b), PM2.5 chemical composition and spatiotemporal variability during the California Regional PM10/PM2.5 Air Quality Study (CRPAQS), *J. Geophys. Res.*, *111*(D10), doi: 10.1029/2005JD006457.

Claeys, M., et al. (2007), Hydroxydicarboxylic acids: Markers for secondary organic aerosol from the photooxidation of alpha-pinene, *Environ. Sci. Technol.*, 41(5), 1628-1634.

Cross, E. S., J. G. Slowik, P. Davidovits, J. D. Allan, D. R. Worsnop, J. T. Jayne, D. K. Lewis, M. Canagaratna, and T. B. Onasch (2007), Laboratory and ambient particle density determinations

using light scattering in conjunction with aerosol mass spectrometry, *Aerosol Sci. Technol.*, 41(4), 343-359.

Day, D. A., S. Liu, L. M. Russell, and P. J. Ziemann (2010), Organonitrate group concentrations in submicron particles with high nitrate and organic fractions in coastal southern California, *Atmos. Environ.*, *44*(16), 1970-1979.

DeCarlo, P. F., et al. (2010), Investigation of the sources and processing of organic aerosol over the Central Mexican Plateau from aircraft measurements during MILAGRO, *Atmos. Chem. Phys.*, 10(12), 5257-5280.

Esteve, W., H. Budzinski, and E. Villenave (2003), Heterogeneous reactivity of OH radicals with phenanthrene, *Polycyclic Aromatic Compounds*, *23*(5), 441-456.

Fatemi, S. M., and B. Y. Jamaloei (2011), Preliminary considerations on the application of toe-to-heel steam flooding (THSF): Injection well-producer well configurations, *Chemical Engineering Research & Design*, 89(11A), 2365-2379.

Gray, H. A., G. R. Cass, J. J. Huntzicker, E. K. Heyerdahl, and J. A. Rau (1986), Characteristics of atmospheric organic and elemental carbon particle concentrations in Los Angeles, *Environ. Sci. Technol.*, 20(6), 580-589.

Gilardoni, S., S. Liu, S. Takahama, L. M. Russell, J. D. Allan, R. Steinbrecher, J. L. Jimenez, P. F. De Carlo, E. J. Dunlea, and D. Baumgardner (2009), Characterization of organic ambient aerosol during MIRAGE 2006 on three platforms, *Atmos. Chem. Phys.*, *9*(15), 5417-5432.

Goldstein, A. H. and I. E. Galbally (2007), Known and unexplored organic constituents in the earth's atmosphere, *Environ. Sci. Technol.*, *41*(5), 1514-1521.

Goldstein, A. H., C. D. Koven, C. L. Heald, and I. Y. Fung (2009), Biogenic carbon and anthropogenic pollutants combine to form a cooling haze over the southeastern United States, *Proc. Natl. Acad. Sci.*, *106*(22), 8835-8840.

Grosjean, D. (1984), Particulate carbon in Los Angeles air, *Science of the Total Environment*, 32(2), 133-145.

Hallquist, M., I. Wangberg, E. Ljungstrom, I. Barnes, and K. H. Becker (1999), Aerosol and product yields from NO_3 radical-initiated oxidation of selected monoterpenes, *Environ. Sci. Technol.*, *33*(4), 553-559.

Hamilton, J. F., P. J. Webb, A. C. Lewis, J. R. Hopkins, S. Smith, and P. Davy (2004), Partially oxidised organic components in urban aerosol using GCXGC-TOF/MS, *Atmos. Chem. Phys.*, *4*, 1279-1290.

Han, J. S., K. J. Moon, S. J. Lee, Y. J. Kim, S. Y. Ryu, S. S. Cliff, and S. M. Yi (2006), Size-resolved source apportionment of ambient particles by positive matrix factorization at Gosan background site in East Asia, *Atmos. Chem. Phys.*, *6*, 211-223.

Hatakeyama, S., T. Tanonaka, J. H. Weng, H. Bandow, H. Takagi, and H. Akimoto (1985), Ozone-cyclohexene reaction in air: quantitative analysis of particulate products and the reaction mechanism, *Environ. Sci. Technol*, 19(10), 935-942.

Hatakeyama, S., M. Ohno, J. H. Weng, H. Takagi, and H. Akimoto (1987), Mechanism for the formation of gaseous and particulate products from ozone-cycloalkene reactions in air, *Environ. Sci. Technol.*, 21(1), 52-57.

Hawkins, L. N. and L. M. Russell (2010), Oxidation of ketone groups in transported biomass burning aerosol from the 2008 Northern California Lightning Series fires, *Atmos. Environ.*, *44*(34), 4142-4154.

He, L. Y., M. Hu, X. F. Huang, B. D. Yu, Y. H. Zhang, and D. Q. Liu (2004), Measurement of emissions of fine particulate organic matter from Chinese cooking, *Atmos. Environ.*, *38*(38), 6557-6564.

He, L. Y., Y. Lin, X. F. Huang, S. Guo, L. Xue, Q. Su, M. Hu, S. J. Luan, and Y. H. Zhang (2010), Characterization of high-resolution aerosol mass spectra of primary organic aerosol emissions from Chinese cooking and biomass burning, *Atmos. Chem. Phys.*, *10*(23), 11535-11543.

Heald, C. L., J. H. Kroll, J. L. Jimenez, K. S. Docherty, P. F. DeCarlo, A. C. Aiken, Q. Chen, S. T. Martin, D. K. Farmer, and P. Artaxo (2010), A simplified description of the evolution of organic aerosol composition in the atmosphere, Geophys. Res. Lett., 37, L08803, doi: 10.1029/2010GL042737.

Heintzenberg, J., D. C. Covert, and R. Van Dingenen (2000), Size distribution and chemical composition of marine aerosols: a compilation and review, *Tellus Series B-Chemical and Physical Meteorology*, 52(4), 1104-1122.

Hildemann, L. M., G. R. Markowski, M. C. Jones, and G. R. Cass (1991), Submicrometer aerosol mass distributions of emissions from boilers, fireplaces, automobiles, diesel trucks, and meat cooking operations, *Aerosol Sci. Technol.*, 14(1), 138-152.

Hoppel, W. A., J. W. Fitzgerald, G. M. Frick, R. E. Larson, and E. J. Mack (1990), Aerosol size distributions and optical properties found in the marine boundary layer over the Atlantic Ocean, J. Geophys. Res., 95(D4), 3659-3686.

Jaoui, M., T. E. Kleindienst, M. Lewandowski, and E. O. Edney (2004), Identification and quantification of aerosol polar oxygenated compounds bearing carboxylic or hydroxyl groups. 1. Method development, *Analytical Chemistry*, 76(16), 4765-4778.

Jaoui, M., E. O. Edney, T. E. Kleindienst, M. Lewandowski, J. H. Offenberg, J. D. Surratt, and J. H. Seinfeld (2008), Formation of secondary organic aerosol from irradiated alpha-pinene/toluene/NOx mixtures and the effect of isoprene and sulfur dioxide, *J. Geophys. Res.*, *113*(D9), D09303, doi: 10.1029/2007JD009426.

Jayne, J. T., D. C. Leard, X. F. Zhang, P. Davidovits, K. A. Smith, C. E. Kolb, and D. R. Worsnop (2000), Development of an aerosol mass spectrometer for size and composition analysis of submicron particles, *Aerosol Sci. Technol.*, *33*(1-2), 49-70.

Jimenez, J. L., et al. (2009), Evolution of Organic Aerosols in the Atmosphere, *Science*, *326*(5959), 1525-1529.

Karanasiou, A. A., P. A. Siskos, and K. Eleftheriadis (2009), Assessment of source apportionment by Positive Matrix Factorization analysis on fine and coarse urban aerosol size fractions, *Atmos. Environ.*, *43*(21), 3385-3395.

Kautzman, K. E., J. D. Surratt, M. N. Chan, A. W. H. Chan, S. P. Hersey, P. S. Chhabra, N. F. Dalleska, P. O. Wennberg, R. C. Flagan, and J. H. Seinfeld (2010), Chemical Composition of Gas- and Aerosol-Phase Products from the Photooxidation of Naphthalene, *Journal of Physical Chemistry A*, *114*(2), 913-934.

Kawamura, K., M. Narukawa, S.-M. Li, and L. A. Barrie (2007), Size distributions of dicarboxylic acids and inorganic ions in atmospheric aerosols collected during polar sunrise in the Canadian high Arctic, *J. Geophys. Res.*, 112(D10), D10307, doi: 10.1029/2006JD008244.

Khalaf, F., P. Literathy, and V. Anderlini (1982), Vanadium as a tracer of oil pollution in the sediments of Kuwait, *Hydrobiologia*, 91, 147-154.

Kirchstetter, T. W., B. C. Singer, R. A. Harley, G. R. Kendall, and J. M. Hesson (1999), Impact of California reformulated gasoline on motor vehicle emissions. 2. Volatile organic compound speciation and reactivity, *Environmental Science & Technology*, *33*(2), 329-336.

Kittelson, D. B. (1998), Engines and nanoparticles: A review, *Journal of Aerosol Science*, 29(5-6), 575-588.

Kleeman, M. J., Riddle, S. G., Robert, M. A., Jakober, C. A., Fine, P. M., Hays, M. D., Schauer, J. J. and Hannigan, M. P.: Source apportionment of fine (PM1.8) and ultrafine (PM0.1) airborne particulate matter during a severe winter pollution episode, *Environ. Sci. Technol.*, 43(2), 272-279, 2009.

Kleeman, M. J., L. S. Hughes, J. O. Allen, and G. R. Cass (1999), Source contributions to the size and composition distribution of atmospheric particles: Southern California in September 1996, *Environ. Sci. Technol.*, *33*(23), 4331-4341.

Kleindienst, T. E., M. Jaoui, M. Lewandowski, J. H. Offenberg, and K. S. Docherty (2012), The formation of SOA and chemical tracer compounds from the photooxidation of naphthalene and its methyl analogs in the presence and absence of nitrogen oxides, *Atmos. Chem. Phys. Discuss.*, 12, 12163-12201.

Kleindienst, T. E., M. Jaoui, M. Lewandowski, J. H. Offenberg, C. W. Lewis, P. V. Bhave, and E. O. Edney (2007), Estimates of the contributions of biogenic and anthropogenic hydrocarbons to secondary organic aerosol at a southeastern US location, *Atmos. Environ.*, 41(37), 8288-8300.

Kwok, E. S. C., W. P. Harger, J. Arey, and R. Atkinson (1994), Reactions of gas-phase phenanthrene under simulated atmospheric conditions, *Environ. Sci. Technol*, *28*(3), 521-527.

Lanz, V. A., Alfarra, M. R., Baltensperger, U., Buchmann, B., Hueglin, C. and Prevot, A. S. H.: Source apportionment of submicron organic aerosols at an urban site by factor analytical modelling of aerosol mass spectra, *Atmos. Chem. Phys.*, 7(6), 1503-1522, 2007.

Lee, J. and D. A. Lane (2009), Unique products from the reaction of naphthalene with the hydroxyl radical, *Atmos. Environ.*, *43*(32), 4886-4893.

Lee, J. and D. A. Lane (2010), Formation of oxidized products from the reaction of gaseous phenanthrene with the OH radical in a reaction chamber, *Atmos. Environ.*, *44*(20), 2469-2477.

Lim, Y. B., and P. J. Ziemann (2009), Chemistry of Secondary Organic Aerosol Formation from OH Radical-Initiated Reactions of Linear, Branched, and Cyclic Alkanes in the Presence of NOx, *Aerosol Sci. Technol.*, *43*(6), 604-619.

Lim, Y. B., and P. J. Ziemann (2005), Products and mechanism of secondary organic aerosol formation from reactions of n-alkanes with OH radicals in the presence of NOx, *Environ. Sci. Technol.*, *39*(23), 9229-9236.

Liu, B. Y. H. and K. W. Lee (1976), Efficiency of membrane and nuclepore filters for submicrometer aerosols, *Environ. Sci. Technol.*, *10*(4), 345-350.

Liu, S., Hu, M., Slanina, S., He, L.-Y., Niu, Y.-W., Bruegemann, E., Gnauk, T. and Herrmann, H.: Size distribution and source analysis of ionic compositions of aerosols in polluted periods at xinken in pearl river delta (PRD) of china, *Atmos. Environ.*, 42(25), 6284-6295, 2008.

Liu, S., S. Takahama, L. M. Russell, S. Gilardoni, and D. Baumgardner (2009), Oxygenated organic functional groups and their sources in single and submicron organic particles in MILAGRO 2006 campaign, *Atmos. Chem. Phys.*, *9*(18), 6849-6863.

Liu, S., D. A. Day, J. E. Shields, and L. M. Russell (2011), Ozone-driven daytime formation of secondary organic aerosol containing carboxylic acid groups and alkane groups, *Atmos. Chem. Phys.*, *11*(16), 8321-8341.

Liu, S., L. M. Russell, D. T. Sueper, and T. B. Onasch (2012), Organic particle types by single-particle measurements using a time-of-flight aerosol mass spectrometer coupled with a light scattering module, *Atmos. Meas. Tech. Discuss*, 5, 3047-3077.

Mader, B. T., R. C. Flagan, and J. H. Seinfeld (2001), Sampling atmospheric carbonaceous aerosols using a particle trap impactor/denuder sampler, *Environ. Sci. Technol.*, 35(24), 4857-4867.

Maria, S. F., L. M. Russell, B. J. Turpin, and R. J. Porcja (2002), FTIR measurements of functional groups and organic mass in aerosol samples over the Caribbean, *Atmos. Environ.*, 36(33), 5185-5196.

Maria, S. F., L. M. Russell, M. K. Gilles, and S. C. B. Myneni (2004), Organic aerosol growth mechanisms and their climate-forcing implications, *Science*, 306(5703), 1921-1924.

Myers, C. O. (1986), Kern River cogeneration project, *IEEE ElectroTechnol. Rev.*, 2, 113-114.

Nakao, S., M. Shrivastava, N. Anh, H. Jung, and D. R. Cocker III (2011), Interpretation of Secondary Organic Aerosol Formation from Diesel Exhaust Photooxidation in an Environmental Chamber, *Aerosol Sci. Technol.*, 45(8).

Na, K., C. Song, C. Switzer, and D. R. Cocker (III) (2007), Effect of ammonia on secondary organic aerosol formation from alpha-Pinene ozonolysis in dry and humid conditions, *Environ. Sci. Technol,* 41(17): 6096-6102.

Ng, N. L., et al. (2010), Organic aerosol components observed in Northern Hemispheric datasets from Aerosol Mass Spectrometry, *Atmos. Chem. Phys.*, *10*(10), 4625-4641.

Ng, N. L., M. R. Canagaratna, J. L. Jimenez, P. S. Chhabra, J. H. Seinfeld, and D. R. Worsnop (2011), Changes in organic aerosol composition with aging inferred from aerosol mass spectra, *Atmos. Chem. Phys.*, 11(13), 6465-6474.

Offenberg, J. H., M. Lewandowski, M. Jaoui, and T. E. Kleindienst (2011), Contributions of Biogenic and Anthropogenic Hydrocarbons to Secondary Organic Aerosol during 2006 in Research Triangle Park, NC, *Aerosol and Air Quality Research*, 11(2), 99-U15.

Paatero, P. and U. Tapper (1994), Positive matrix factorization – A nonnegative factor model with optimal utilization of error-estimates of data values, *Environmetrics*, *5*(2), 111-126.

Paatero, P. and P. K. Hopke (2003), Discarding or downweighting high-noise variables in factor analytic models, *Analytica Chimica Acta*, *490*(1-2), 277-289.

Pye, H. O. T., and G. A. Pouliot (2012), Modeling the Role of Alkanes, Polycyclic Aromatic Hydrocarbons, and Their Oligomers in Secondary Organic Aerosol Formation, *Environ. Sci. Technol.*, doi: 10.1021/es300409w.

Richard, A., Gianini, M. F. D., Mohr, C., Furger, M., Bukowiecki, N., Minguillon, M. C., Lienemann, P., Flechsig, U., Appel, K., DeCarlo, P. F., Heringa, M. F., Chirico, R., Baltensperger, U., Prevot, A. S. H.. (2011), Source apportionment of size and time resolved trace elements and organic aerosols from an urban courtyard site in Switzerland, *Atmos. Chem. Phys*, *11*(17), 8945-8963.

Richter, H. and J. B. Howard (2000), Formation of polycyclic aromatic hydrocarbons and their growth to soot - a review of chemical reaction pathways, *Progress in Energy and Combustion Science*, *26*(4-6), 565-608.

Rodgers, J. L. and W. A. Nicewander (1998), Thirteen ways to look at the correlation-coefficient, *American Statistician*, 42(1), 59-66.

Rollins, A. W., E. C. Browne, K.-E. Min, S. E. Pusede, P. J. Wooldridge, D. R. Gentner, A. H. Goldstein, S. Liu, D. A. Day, L. M. Russell, and R. C. Cohen, Nighttime growth of particulate organic nitrates: A significant source of atmospheric secondary organic aerosols, *Science*, in press.

Russell, L. M., S. F. Maria, and S. C. B. Myneni (2002), Mapping organic coatings on atmospheric particles, *Geophys. Res. Lett.*, 29 (16), doi: 10.1029/2002GL014874.

Russell, L. M. (2003): Aerosol organic-mass-to-organic-carbon ratio measurements, *Environ. Sci. Technol.*, 37(13), 2982-2987.

Russell, L. M., S. Takahama, S. Liu, L. N. Hawkins, D. S. Covert, P. K. Quinn, and T. S. Bates (2009), Oxygenated fraction and mass of organic aerosol from direct emission and atmospheric processing measured on the R/V Ronald Brown during TEXAQS/GoMACCS 2006, *J. Geophys. Res*, *114*, D00F05, doi: 10.1029/2008JD011275.

Russell, L. M., R. Bahadur, and P. J. Ziemann (2011), Identifying organic aerosol sources by comparing functional group composition in chamber and atmospheric particles, *Proc. Natl. Acad. Sci.*, *108*(9), 3516-3521.

Schade, G. W. and P. J. Crutzen (1995), Emission of Aliphatic-amines from animal husbandry and their reactions-potential source of N_2O and HCN, *Journal of Atmospheric Chemistry*, *22* (3), 319-346.

Schauer, J. J., Rogge, W. F., Hildemann, L. M., Mazurek, M. A., Cass, G. R. and Simoneit, B. R. T.: Source apportionment of airborne particulate matter using organic compounds as tracers, *Atmos. Environ.*, 30(22), 3837-3855, 1996.

Schauer, J. J., M. J. Kleeman, G. R. Cass, and B. R. T. Simoneit (1999), Measurement of emissions from air pollution sources. 2. C-1 through C-30 organic compounds from medium duty diesel trucks, *Environ. Sci. Technol.*, *33*(10), 1578-1587.

Schauer, J. J., and G. R. Cass (2000), Source apportionment of wintertime gas-phase and particle-phase air pollutants using organic compounds as tracers, *Environ. Sci. Technol.*, *34*(9), 1821-1832.

Schauer, J. J., M. P. Fraser, G. R. Cass, and B. R. T. Simoneit (2002a), Source reconciliation of atmospheric gas-phase and particle-phase pollutants during a severe photochemical smog episode, *Environ. Sci. Technol.*, 36(17), 3806-3814.

Schauer, J. J., M. J. Kleeman, G. R. Cass, and B. R. T. Simoneit (2002b), Measurement of emissions from air pollution sources. 5. C-1-C-32 organic compounds from gasoline-powered motor vehicles, *Environ. Sci. Technol.*, *36*(6), 1169-1180.

Schwartz, R. E., et al. (2010), Biogenic oxidized organic functional groups in aerosol particles from a mountain forest site and their similarities to laboratory chamber products, *Atmos. Chem. Phys.*, 10(11), 5075-5088.

Sheesley, R. J., J. J. Schauer and D. Kenski (2004), Trends in secondary organic aerosol at a remote site in Michigan's Upper Peninsula, *Environ. Sci. Technol.*, 38, 6491-6500.

Seinfeld, J. H. and S. N. Pandis (2006): Atmospheric chemistry and physics—from air pollution to climate change, John Wiley & Sons New Jersey.

Shakya, K. M. and R. J. Griffin (2010), Secondary Organic Aerosol from Photooxidation of Polycyclic Aromatic Hydrocarbons, *Environ. Sci. Technol.*, *44*(21), 8134-8139.

Sorooshian, A., S. N. Murphy, S. Hersey, H. Gates, L. T. Padro, A. Nenes, F. J. Brechtel, H. Jonsson, R. C. Flagan, and J. H. Seinfeld (2008), Comprehensive airborne characterization of aerosol from a major bovine source, *Atmos. Chem. Phys.*, *8*(17), 5489-5520.

Srivastava, A., S. Gupta, and V. K. Jain (2008), Source apportionment of total suspended particulate matter in coarse and fine size ranges over Delhi, *Aerosol and Air Quality Research*, *8*(2), 188-200.

Stein, S. E. and D. R. Scott (1994), Optimization and testing of mass-spectral library search algorithms for compound identification, *Journal of the American Society for Mass Spectrometry*, 5(9), 859-866.

Sun, Y. L., Zhang, Q., Schwab, J. J., Demerjian, K. L., Chen, W. N., Bae, M. S., Hung, H. M., Hogrefe, O., Frank, B., Rattigan, O. V. and Lin, Y. C. (2011), Characterization of the sources and processes of organic and inorganic aerosols in new york city with a high-resolution time-of-flight aerosol mass apectrometer, *Atmos. Chem. Phys.*, 11(4), 1581-1602.

Surratt, J. D., et al. (2008), Organosulfate formation in biogenic secondary organic aerosol, *Journal of Physical Chemistry A*, 112(36), 8345-8378.

Takahama, S., S. Liu, and L. M. Russell (2010), Coatings and clusters of carboxylic acids in carbon-containing atmospheric particles from spectromicroscopy and their implications for cloud-nucleating and optical properties, *J. Geophys. Res.*, 115, D01202, doi: 10.1029/2009JD012622.

Takahama, S., S. Gilardoni, L. M. Russell, and A. L. D. Kilcoyne (2007), Classification of multiple types of organic carbon composition in atmospheric particles by scanning transmission X-ray microscopy analysis, *Atmos. Environ*, 41(40), 9435-9451.

Tanner, R. L. and B. Zielinska (1994), Determination of the biogenic emission rates of species contributing to VOC in the San Joaquin Valley of California, *Atmos. Environ*, 28(6), 1113-1120.

Tegen, I., and A. A. Lacis (1996), Modeling of particle size distribution and its influence on the radiative properties of mineral dust aerosol, *J. Geophys. Res.*, 101(D14), 19237-19244.

Tivanski, A. V., R. J. Hopkins, T. Tyliszczak, and M. K. Gilles (2007), Oxygenated interface on biomass burn tar balls determined by single particle scanning transmission X-ray microscopy, *Journal of Physical Chemistry A*, *111*(25), 5448-5458.

Turpin, B. J., J. J. Huntzicker, S. M. Larson, and G. R. Cass (1991), Los Angeles summer midday particulate carbon-primary and secondary aerosol, *Environ. Sci. Technol.*, 25(10), 1788-1793.

Turpin, B. J., P. Saxena, and E. Andrews (2000), Measuring and simulating particulate organics in the atmosphere: Problems and prospects, *Atmos. Environ.*, 34(18), 2983-3013.

Ulbrich, I. M., M. Lechner, and J. L. Jimenez (2007), AMS Spectral Database, http://cires.colorado.edu/jimenez-group/AMSsd.

Ulbrich, I. M., M. R. Canagaratna, Q. Zhang, D. R. Worsnop, and J. L. Jimenez (2009), Interpretation of organic components from Positive Matrix Factorization of aerosol mass spectrometric data, *Atmos. Chem. Phys.*, *9*(9), 2891-2918.

Ulbrich, I. M., M. R. Canagaratna, M. J. Cubison, Q. Zhang, N. L. Ng, A. C. Aiken, and J. L. Jimenez: Three-dimensional factorization of size-resolved organic aerosol mass spectra from mexico city, *Atmos. Meas. Tech*., 5, 195-224, 2012.

Usher, C. R., A. E. Michel, and V. H. Grassian (2003), Reactions on mineral dust, *Chem. Rev.*, 103(12), 4883-4939.

Wallace, L. A., S. J. Emmerich, and C. Howard-Reed (2004), Source strengths of ultrafine and fine particles due to cooking with a gas stove, *Environ. Sci. Technol.*, 38(8), 2304-2311.

Wang, L., R. Atkinson, and J. Arey (2007), Dicarbonyl products of the OH radical-initiated reactions of naphthalene and the C-1- and C-2-alkylnaphthalenes, *Environ. Sci. Technol.*, *41*(8), 2803-2810.

Wangberg, I., I. Barnes, and K. H. Becker (1997), Product and mechanistic study of the reaction of NO3 radicals with alpha-pinene, *Environ. Sci. Technol.*, *31*(7), 2130-2135.

Ward, J. H. (1963), Hierarchical grouping to optimize an objective function, *J. Am. Stat. Assoc*., 58(301), 236–244, doi:10.2307/2282967.

Webb, P. J., J. F. Hamilton, A. C. Lewis, and K. Wirtz (2006), Formation of oxygenated-polycyclic aromatic compounds in aerosol from the photo-oxidation of o-tolualdehyde, *Polycyclic Aromatic Compounds*, *26*(4), 237-252.

Whitby, K. T., B. Y. H. Liu, and Husar R. B. (1972), Aerosol size distribution of Los Angeles smog, *Journal of Colloid and Interface Science*, 39(1), 177-204.

Williams, B. J., A. H. Goldstein, N. M. Kreisberg, and S. V. Hering (2006), An in-situ instrument for speciated organic composition of atmospheric aerosols: Thermal Desorption Aerosol GC/MS-FID (TAG), *Aerosol Science and Technology*, *40*(8), 627-638.

Worton, D. R., Goldstein, A. H., Farmer, D. K., Docherty, K. S., Jimenez, J. L., Gilman, J. B., Kuster, W. C., de Gouw, J., Williams, B. J., Kreisberg, N. M., Hering, S. V., Bench, G., McKay, M., Kristensen, K., Glasius, M., Surratt, J. D. and Seinfeld, J. H. (2011), Origins and composition of fine atmospheric carbonaceous aerosol in the Sierra Nevada Mountains, California, *Atmos. Chem. Phys.*, 11(19), 10219-10241.

Yee, L. D., J. S. Craven, C. L. Loza, K. A. Schilling, N. L. Ng, M. R. Canagaratna, P. J. Ziemann, R. C. Flagan, and J. H. Seinfeld (2012), Secondary Organic Aerosol Formation from Low-NOx Photooxidation of Dodecane: Evolution of Multi-Generation Gas-Phase Chemistry and Aerosol Composition, *Journal of Physical Chemistry A*, doi: 10.1021/jp211531h.

Zhang, Q., Canagaratna, M. R., Jayne, J. T., Worsnop, D. R. and Jimenez, J. L. (2005), Time- and size-resolved chemical composition of submicron particles in Pittsburgh: Implications for aerosol sources and processes, *J. Geophys. Res.*, 110 (D7), D07S09, doi:10.1029/2004JD004649.

Zhang, Q., et al. (2007), Ubiquity and dominance of oxygenated species in organic aerosols in anthropogenically-influenced Northern Hemisphere midlatitudes, *Geophys. Res. Lett.*, 34(13), L13801, doi:10.1029/2007GL029979.

Zhang, H., J. D. Surratt, Y. H. Lin, J. Bapat, and R. M. Kamens (2011), Effect of relative humidity on SOA formation from isoprene/NO photooxidation: enhancement of 2-methylglyceric acid and its corresponding oligoesters under dry conditions, *Atmos. Chem. Phys.*, 11(13), 6411-6424.

Zhao, Y., et al. (in preparation). Insights for SOA formation mechanisms from measured gas/particle partitioning of specific organic tracer compounds.

Zheng, M., G. R. Cass, J. J. Schauer, and E. S. Edgerton (2002), Source apportionment of PM2.5 in the southeastern United States using solvent-extractable organic compounds as tracers, *Environ. Sci. Technol.*, 36(11), 2361-2371.

Zhong, S. Y., C. D. Whiteman, and X. D. Bian (2004), Diurnal evolution of three-dimensional wind and temperature structure in California's Central Valley, *Journal of Applied Meteorology*, *43*(11), 1679-1699.

Figure captions

Figure 1. (a) Comparison of DMA-measured PM_{500nm} (d_m) with the sum of concentrations for AMS-measured PM_{700nm} (d_{va}) and EC. Correlation coefficient and slope are 0.88 and 0.97, respectively. Hourly-averaged concentrations were used to match the 1-hr time resolution of EC measurements; (b) comparison of DMA-measured PM_{700nm} (d_m) with the sum of concentrations for AMS-measured PM_1 (d_{va}), EC, and dusts. Correlation coefficient and slope are 0.90 and 0.98, respectively. Averaged concentrations of 3 or 6 hr (time resolution for FTIR measurements) were used for comparison. Dust was assumed to be a mixture of metal oxides and salts, including SiO_2, Al_2O_3, Fe_2O_3, Na_2O, K_2O, TiO_2, BaO, MnO, $CaCO_3$, and $MgCO_3$ [*Usher et al.*, 2003]; their concentrations were calculated from corresponding elemental concentrations quantified by XRF. In both figures, a CE of 0.8 was used for AMS measurements. The red line in each panel shows the best linear fit for the data points.

Figure 2. Campaign average composition of (a) PM_1, (b) $PM_{2.5}$, and (c) PM_{150nm} [*Ahlm et al.*, 2012]. The OM concentration in PM_1 and PM_{150nm} was measured by the AMS. The OM in $PM_{2.5}$ was calculated by scaling the AMS-measured OM_1 by the FTIR-measured $OM_{2.5}$-to-OM_1 ratio. The concentration of dust in (a) and (b) was calculated using the XRF-measured dust elements in PM_1 and $PM_{2.5}$ as described in Figure 1. EC was not shown in PM_{150nm} because ultrafine EC measurements were not available.

Figure 3. Time series of FTIR-measured organic functional group concentrations (stacked bars) in PM_1 and AMS-measured OM (green line). The pie chart shows campaign average functional group composition in PM_1.

Figure 4. FTIR spectra during CalNex for (a) cluster 1 (143 spectra), (b) cluster 2 (69 spectra), (c) cluster 3 (11 spectra), and (d) cluster 4 (5 spectra). Horizontal bars represent functional group absorbance ranges: hydroxyl (pink), carboxylic acid (green), alkane (blue), nonacid carbonyl (teal), amine (orange), organonitrate (beige). Pie chart shows the average functional group composition in each cluster. Vertical bar represents the average relative contributions of the FTIR factors in each clusters, with colors indicating alkane SOA (blue), aromatic SOA (red), nighttime OA (green), PO SOA (black), and vegetative detritus (orange).

Figure 5. Van Krevelen diagram (H/C versus O/C) from the AMS measurements. The points are colored by temperature (°C), with the scale shown by the vertical bar. The points with temperature greater and less than 25 °C are fitted by the red and blue dashed lines, respectively. The slopes of the red and blue lines are -0.93 and -1.3, respectively. The intercepts of the red and blue lines are 1.76 and 1.91, respectively.

Figure 6. (a) FTIR factor spectra derived from PM_1 (solid line) and $PM_{2.5}$ (dashed line) measurements. The pie charts show factor compositions, with functional groups as follows: alkane (blue), hydroxyl (hot pink), carboxylic acid (green), nonacid carbonyl (teal), and organonitrate (beige) functional groups. (b) Campaign average mass fractions of FTIR PM_1 and AMS factors. Colors indicate aromatic SOA (red) (red and dark red for the AMS low and high O/C aromatic SOA factors, respectively), alkane SOA (blue) (light blue and dark blue for the AMS low and high O/C alkane SOA factors, respectively), nighttime OA (green), PO SOA (black), and vegetative detritus (orange), and COA (purple) factors. (c) Normalized mass spectra of AMS factors.

Figure 7. Diurnal cycles for (a) aromatic SOA_{FTIR} (red), low O/C aromatic SOA_{AMS} (red), and high O/C aromatic SOA_{AMS} (dark red), (b) alkane SOA_{FTIR} (blue), low O/C alkane SOA_{AMS} (light blue), and high O/C alkane SOA_{AMS} (dark blue), (c) nighttime OA_{FTIR} (green) and nighttime OA_{AMS} (green), (d) PO SOA_{FTIR} (black) and PO SOA_{AMS} (black), (e) vegetative detritus (orange), and (f) COA (purple) factors. In each panel, horizontal bars represent FTIR factors (PM_1 samples), with bar lengths indicating sampling duration; lines with markers represent AMS factors.

Figure 8. Mass concentration comparison of FTIR PM_1 and $PM_{2.5}$ factors. Striped and solid bars indicate PM_1 and $PM_{2.5}$ factors, respectively. Color assignments for functional groups are the same as in Figure 3.

Figure 9. Normalized single-particle X-ray spectra for particle types: a) Group I (35 particles), b) Group II (24 particles), and c) Group III (21 particles). Other identifiers include individual particle spectra (gray) and group averages (blue). For comparison, note type “a”, “h”, and “k” particles (red) [as identified by *Takahama et al.* 2007], respectively, in panels a), b), and c). Vertical lines (orange) in each panel represent absorptions at energies 285.0, 288.7, 297.4, and 299.9 eV.

Figure 10. (a) Diurnal variations of mass fraction for the high O/C alkane SOA_{AMS} factor (blue boxes), mass fraction for the high O/C aromatic SOA_{AMS} factor (dashed red line), odd oxygen (pink), CO (black), and OH (purple). (OH radical was measured by William Brune’s research group [*Ahlm et al.*, 2012].) The horizontal bar in each box represents the median value. Upper and lower bounds of the boxes represent 25th and 75th percentiles, with whiskers extending to 5th and 95th percentiles. (b) Correlation of mass fraction of the high O/C alkane SOA_{AMS} (blue) and high O/C aromatic

SOA_{AMS} (red) factors to odd oxygen. Darker colors indicate higher temperatures as the vertical color bars show.

Figure 11. (a) Diurnal cycle of nighttime OA_{FTIR} with inner charts showing frequency of daytime and nighttime wind directions. (b) Correlation of nighttime OA_{FTIR} with NO_x for nighttime samples. The inner box plot shows dependence of factor concentration on RH, which included at least 10 points (45 points total) per bin. For each box in (a) and (b), upper and lower bounds represent 25th and 75th percentiles, and whiskers extend to 5th and 95th percentiles.

Figure 12. Size distributions of r^2 (fraction of variability explained) for FTIR and AMS factors (left axes) and mass size distributions of (a) m/z 44, (b) m/z 57, (c) m/z 43, and (d) sulfate and nitrate (right axes) for daytime (I) and nighttime (II) measurements. Legends for the factors and AMS-measured components are displayed on the left and right sides of the graphs, respectively.

Figure A1. Dependence of $Q/Q_{expected}$ on FPEAK values for FTIR PM_1 (blue), FTIR $PM_{2.5}$ (green), and AMS (red) PMF analyses.

Figure A2. Dependence of $Q/Q_{expected}$ on number of factors for FTIR PM_1 (blue), FTIR $PM_{2.5}$ (green; right axis), and AMS (red) PMF analyses. Solid circles indicate selected solutions.

Figure A3. Time series for (a) normalized (by total infrared absorptions) sum of total residuals of FTIR PM_1 5-factor solution, (b) normalized sum of total residuals of FTIR $PM_{2.5}$ 6-factor solution, and (c) sum of total residuals of the AMS 6- or 7-factor solution.

Figure A4. Box plots of scaled residuals for (a) FTIR PM_1 5-factor solution, (b) FTIR $PM_{2.5}$ 6-factor solution, and (c) AMS 6- or 7-factor solution. Upper and lower bounds of the boxes represent 25th and 75th percentiles, and whiskers extend to 5th and 95th percentiles.

Figure A5. Time series of Q/Q_{exp} for (a) the 5-factor solution of FTIR PM_1, (b) the 6-factor solution of FTIR $PM_{2.5}$, and (c) the 6- or 7-factor solution of the AMS measurements.

Figure A6. Q/Q_{exp} contribution to each wavenumber for (a) the 5-factor solution of FTIR PM_1 and (b) the 6-factor solution of FTIR PM2.5. (c) Q/Q_{exp} contribution to each fragment for the 6- or 7-factor solution of the AMS measurements.

Figure A7. Factor mass spectra for the 6-factor (blue) and 7-factor (red) solution.

Figure A8. Factor time series for the 6-factor (blue) and 7-factor solutions.

Figure A9. Correlation of the FTIR and AMS factors. The AMS aromatic SOA is the sum of the high and low O/C aromatic SOA_{AMS} factors, and the AMS alkane SOA is the sum of the high and low O/C alkane SOA_{AMS}.

Table 1. Campaign average OM (measured by FTIR and AMS) and organic functional group (measured by FTIR) concentrations (μg m^{-3}) in PM_1 and $PM_{2.5}$. Functional group mass fractions are shown in parentheses.

	$FTIR_{PM1}$	$FTIR_{PM2.5}$	AMS
OM	2.42±1.68	3.24±1.42	3.38±2.20
Alkane	0.85±0.73 (35%)	1.09±0.45 (34%)	-
Hydroxyl	0.53±0.58 (22%)	0.98±1.00 (30%)	-
Carboxylic acid	0.51±0.58 (21%)	0.61±0.29 (19%)	-
Nonacid carbonyl	0.26±0.24 (11%)	0.14±0.20 (4%)	-
Amine	0.22±0.18 (9%)	0.33±0.15 (10%)	-
Organonitrate	0.05±0.05 (2%)	0.07±0.06 (2%)	-
Organosulfate	BDL	0.02±0.04 (1%)	-

Table 2. Summary of O/C values for primary or HOA components from previous studies and O/C of SOA components in this study.

Source type	O/C[a]	References
Primary OA	< 0.1	This study
HOA (New York City)	0.06	Sun et al., 2011
HOA (Mexico City aircraft)	0.06	DeCarlo et al., 2010
Diesel exhaust	0.03	Aiken et al., 2008
	0.05	Nakao et al., 2011
Gasoline exhaust	0.04	Aiken et al., 2008
Cooking emission	0.08-0.13	He et al., 2010
COA	0.11	Huang et al., 2010
COA	0.05	This study
Nighttime OA	0.01	This study
Secondary OA	0.20–0.68	This study
Alkane SOA	0.27–0.63	This study
Aromatic SOA	0.36-0.68	This study
PO SOA	0.20	This study

[a]AMS-measured O/C excludes organonitrate and organosulfate contributions to O as the nitrate and sulfate components were not distinguishable from inorganic.

Table 3. Summary of concentration, OM fraction (in parentheses), oxidant, peak time, O/C, organic functional group (OFG) composition, size range, and source of FTIR and the AMS factors. The colors in the pie charts represent alkane (blue), hydroxyl (hot pink), carboxylic acid (green), nonacid carbonyl (teal), and organonitrate (beige) functional groups.

FTIR			AMS								
Factor	Concentration in PM_1 (μg m^{-3})	Concentration in $PM_{2.5}$ (μg m^{-3})	Factor	Concentration in PM_1 (μg m^{-3})	Oxidant	Peak Time	O/C	OFG	Size (nm)	Source	Primary or secondary
Aromatic SOA	0.61 (24%)	0.77 (23%)	Low O/C aromatic SOA	0.35 (9%)	OH	0-6; 12-18	0.36		250-900	Fossil fuel combustion	Secondary
			High O/C aromatic SOA	0.64 (16%)	OH	18-23	0.68		200-500	Fossil fuel combustion	Secondary
Alkane SOA	1.21 (41%)	1.43 (43%)	Low O/C alkane SOA	0.48 (12%)	OH	22-6	0.27		200-500	Fossil fuel combustion	Secondary
			High O/C alkane SOA	1.19 (30%)	O_3	10-17	0.63		200-500	Fossil fuel combustion	Secondary
Nighttime OA	0.30 (10%)	0.25 (8%)	Nighttime OA	0.50 (13%)	NO_3	0-6	0.01		400-700	Fossil fuel combustion/biogenic emissions	Primary and secondary
PO SOA	0.42 (14%)	0.42 (13%)	PO SOA	0.49 (13%)	OH and/or O_3	10-17	0.20		100-200	Petroleum operations	Secondary
Vegetative detritus	0.29 (10%)	0.45 (14%)	-	-	-	12-18	1.09		-	Resuspended dusts and plant materials	Primary
-	-	-	COA	0.29 (7%)	-	12-18; 20-23	0.05	-	100- 200	Cooking activities	Primary

Table 4. Mean concentration, variability, and fraction of variability explained by the AMS factors for the OM sections.

		$OM_{30\text{-}100}$	$OM_{100\text{-}200}$	$OM_{200\text{-}300}$	$OM_{300\text{-}400}$	$OM_{400\text{-}500}$	$OM_{500\text{-}600}$	$OM_{600\text{-}700}$	$OM_{700\text{-}800}$	$OM_{800\text{-}900}$	$OM_{900\text{-}1000}$
Mean concentration ($\mu g\ m^{-3}$)		0.12	0.55	0.30	0.20	0.11	0.07	0.04	0.03	0.01	0.01
Variability (standard deviation) ($\mu g\ m^{-3}$)		0.08	0.32	0.22	0.17	0.09	0.06	0.04	0.03	0.02	0.01
Ratio of variability to mean		0.69	0.58	0.71	0.83	0.83	0.83	0.95	1.05	1.20	1.50
Fraction of variability explained (r^2)	Low O/C aromatic SOA	0.03	0.04	0.36	0.44	0.49	0.45	0.43	0.45	0.38	0.35
	High O/C aromatic SOA	0.02	0.28	0.69	0.61	0.35	0.15	0.10	0.12	0.13	0.14
	Low O/C alkane SOA	0.01	0.26	0.60	0.53	0.44	0.30	0.27	0.27	0.24	0.25
	High O/C alkane SOA	0.01	0.16	0.67	0.64	0.31	0.12	0.10	0.13	0.14	0.15
	Nighttime OA	0.00	0.04	0.05	0.12	0.45	0.67	0.66	0.56	0.44	0.31
	PO SOA	0.25	0.53	0.33	0.20	0.08	0.02	0.01	0.02	0.03	0.03
	COA	0.21	0.48	0.07	0.01	0.00	0.00	0.00	0.00	0.00	0.00

Table A1a. Correlations of FTIR factors in PM_1 to source markers.

	PAH					PAH SOA						Alkane		Alkane SOA				Biogenic SOA	Petroleum operation	Dust				Cooking
	Methylanthracene	Methylphenanthracene-1	Methylphenanthracene	Naphthalene-2-phenyl	1, 2-Benzanthracene	2H-1-benzopyran-2-one	Dibenzofuran	1,8-Naphthalic acid/Naphthalic anhydride	Benzophenone	4-hydroxy-9-fluorenone	Phthalic acid/Phthalic anhydride	Heptadecane	Octadecane	Undecanone	Dodecanone	Tridecanone	Tetradecanone	Pinonaldehyde	V	Si	Ca	Al	Mg	Hexadecanoic acid[a]
Aromatic SOA	0.49	0.54	0.54	0.47	0.17	0.75	0.73	0.69	0.67	0.67	0.62	0.21	0.16	0.65	0.39	0.60	0.56	0.24	0.15	0.28	0.16	0.25	0.12	-
Alkane SOA	0.56	0.50	0.50	0.54	0.13	0.72	0.35	0.63	0.43	0.58	0.58	0.38	0.46	0.71	0.65	0.63	0.77	0.28	-0.01	0.19	0.22	0.15	0.06	-
Nighttime OA	0.50	0.47	0.47	0.40	0.37	-0.16	-0.17	0.04	-0.31	-0.20	0.01	0.50	0.53	0.2	-0.10	0.47	-0.07	0.65	-0.06	-0.01	0.07	-0.01	-0.03	-
PO SOA	0.11	0.11	0.05	0.12	-0.07	0.36	0.37	-0.09	0.39	0.21	0.28	-0.04	-0.10	0.42	0.03	0.32	0.26	0.12	0.60	0.02	-0.06	-0.01	-0.06	-
Vegetative detritus	-0.01	-0.07	-0.07	-0.03	0.15	-0.22	-0.05	-0.03	-0.07	-0.05	-0.08	-0.09	-0.14	0.42	0.18	0.13	0.04	-0.08	0.04	0.82	0.74	0.90	0.94	-

[a]Correlations are not reported for the cooking marker since less than 10 data points remained after averaging-to-filter sampling times.

Table A1b. Correlations of FTIR factors in $PM_{2.5}$ to source markers.

	PAH					PAH SOA						Alkane		Alkane SOA				Biogenic SOA	Petroleum operation	Dust				Cooking
	Methylanthracene	Methylphenanthracene-1	Methylphenanthracene	Naphthalene-2-phenyl	1, 2-Benzanthracene	2H-1-benzopyran-2-one	Dibenzofuran	1,8-Naphthalic acid/Naphthalic anhydride	Benzophenone	4-hydroxy-9-fluorenone	Phthalic acid/Phthalic anhydride	Heptadecane	Octadecane	Undecanone	Dodecanone	Tridecanone	Tetradecanone	pinonaldehyde	V	Si	Ca	Al	Mg	Hexadecanoic acid[a]
Aromatic SOA	0.59	0.67	0.67	0.56	0.18	0.73	0.61	0.68	0.63	0.67	0.66	0.45	0.47	0.75	0.79	0.76	0.81	0.57	0.04	-0.03	-0.34	-0.04	-0.13	-
Alkane SOA	0.66	0.74	0.74	0.65	0.49	0.67	0.53	0.68	0.58	0.56	0.47	0.49	0.53	0.90	0.65	0.85	0.58	0.53	-0.52	-0.52	-0.03	-0.53	-0.56	-
Nighttime OA	0.45	0.41	0.41	0.26	0.59	-0.18	0.06	0.24	-0.09	-0.04	0.16	0.02	-0.05	0.29	-0.16	0.07	0.07	0.04	0.67	0.74	0.47	0.73	0.78	-
PO SOA	-0.20	-0.14	-0.14	0.00	0.07	-0.10	-0.19	-0.25	-0.09	0.04	-0.44	0.01	0.01	-0.19	-0.14	0.07	-0.32	-0.04	-0.31	-0.26	-0.10	-0.25	-0.25	-
Vegetative detritus	-0.30	-0.33	-0.33	-0.34	-0.24	-0.27	-0.29	-0.34	-0.30	-0.25	-0.12	-0.24	-0.24	0.03	-0.50	-0.35	-0.34	-0.18	0.78	0.81	0.41	0.82	0.77	-

[a]Correlations are not reported for the cooking marker since less than 10 data points remained after averaging-to-filter sampling times.

Table A2a. Correlations of AMS factors to source markers for the 6-factor solution.

	PAH					PAH SOA						Alkane		Alkane SOA				Biogenic SOA	Petroleum Operation	Dust				Cook
	Methylanthracene	Methylphenanthracene-1	Methylphenanthracene	Naphthalene-2-phenyl	1, 2-Benzanthracene	2H-1-benzopyran-2-one	Dibenzofuran	1,8-Naphthalic acid/Naphthalic anhydride	Benzophenone	4-hydroxy-9-fluorenone	Phthalic acid/Phthalic anhydride	Heptadecane	Octadecane	Undecanone	Dodecanone	Tridecanone	Tetradecanone	pinonaldehyde	V	Si	Ca	Al	Mg	Hexadecanoic acid
Low O/C aromatic SOA	0.71	0.60	0.60	0.60	0.55	0.43	0.25	0.40	0.22	0.40	0.36	0.42	0.42	0.36	0.40	0.54	0.52	0.25	0.29	0.22	0.27	0.17	0	0.4
Low O/C Alkane SOA	0.75	0.81	0.81	0.76	0.60	0.34	0.12	0.71	0.03	0.37	0.23	0.69	0.68	0.61	0.73	0.82	0.70	0.67	-0.20	0.13	0.17	0.10	-0.32	0.2
High O/C aromatic SOA	0.58	0.62	0.59	0.55	0.56	0.76	0.62	0.75	0.72	0.65	0.62	0.34	0.33	0.46	0.40	0.62	0.59	0.30	0.15	0.43	0.38	0.39	0.17	0.4
Nighttime OA	0.32	0.25	0.26	0.31	0.36	-0.06	-0.18	0.04	-0.26	-0.13	-0.07	0.21	0.22	-0.01	0.50	0.29	0.27	0.00	-0.30	-0.11	0	-0.12	-0.24	0.1
PO SOA	-0.02	0	0.03	0.09	-0.22	0.50	0.27	0.01	0.35	0.39	0.34	0.09	0.15	0.28	0.22	0.13	0.09	0.28	0.39	0.10	0.13	0.10	0	0.1
COA	-0.08	-0.07	-0.14	-0.06	0.04	0.09	-0.14	-0.03	-0.13	0.16	-0.08	-0.04	0.01	-0.25	0.44	0.42	0.40	-0.13	0	-0.16	-0.15	-0.17	-0.39	0.8

Table A2b. Correlations of AMS Group I factors to source markers for the 7-factor solution.

	PAH					PAH SOA						Alkane		Alkane SOA				Biogenic SOA	Petroleum Operation	Dust				Cooking
	Methylanthracene	Methylphenanthracene-1	Methylphenanthracene	Naphthalene-2-phenyl	1, 2-Benzanthracene	2H-1-benzopyran-2-one	Dibenzofuran	1,8-Naphthalic acid/Naphthalic anhydride	Benzophenone	4-hydroxy-9-fluorenone	Phthalic acid/Phthalic anhydride	Heptadecane	Octadecane	Undecanone	Dodecanone	Tridecanone	Tetradecanone	pinonaldehyde	V	Si	Ca	Al	Mg	Hexadecanoic acid
Low O/C aromatic SOA	0.90	0.84	0.84	0.82	0.81	0.43	0.32	0.69	0.26	0.39	0.38	0.56	0.60	0.58	0.49	0.66	0.62	0.35	0.00	0.35	0.38	0.31	0.22	0.43
Low O/C alkane SOA	0.72	0.78	0.78	0.73	0.57	0.29	0.07	0.67	-0.02	0.32	0.17	0.66	0.66	0.59	0.73	0.81	0.68	0.69	-0.09	0.08	0.12	0.08	-0.05	0.25
High O/C aromatic SOA	0.42	0.46	0.42	0.45	0.38	0.64	0.37	0.65	0.44	0.62	0.49	0.25	0.27	0.28	0.52	0.71	0.66	0.15	-0.03	0.32	0.29	0.29	0.14	0.62
High O/C alkane SOA	0.55	0.61	0.60	0.56	0.43	0.78	0.61	0.68	0.70	0.66	0.60	0.37	0.38	0.52	0.38	0.54	0.50	0.44	0.02	0.38	0.36	0.34	0.22	0.27
Nighttime OA	0.32	0.25	0.26	0.31	0.36	-0.07	-0.18	0.04	-0.27	-0.13	-0.07	0.21	0.22	0.00	0.49	0.29	0.27	0.00	-0.17	-0.10	0.00	-0.11	-0.10	0.15
PO SOA	-0.12	-0.12	-0.10	-0.04	-0.32	0.38	0.17	-0.13	0.24	0.31	0.28	0.01	0.08	0.21	0.22	0.10	0.07	0.16	0.40	0.07	0.10	0.03	0.01	0.19
COA	-0.19	-0.22	-0.21	-0.13	-0.09	0.07	-0.13	-0.27	-0.11	0.05	-0.14	-0.10	-0.03	-0.25	0.33	0.14	0.15	-0.13	-0.03	-0.18	-0.17	-0.18	-0.16	0.68

Table A2c. Correlations of AMS Group II factors to source markers for the 7-factor solution.

	PAH					PAH SOA						Alkane		Alkane SOA				Biogenic SOA	Petroleum Operation	Dust				Cooking
	Methylanthracene	Methylphenanthracene-1	Methylphenanthracene	Naphthalene-2-phenyl	1, 2-Benzanthracene	2H-1-benzopyran-2-one	Dibenzofuran	1,8-Naphthalic acid/Naphthalic anhydride	Benzophenone	4-hydroxy-9-fluorenone	Phthalic acid/Phthalic anhydride	Heptadecane	Octadecane	Undecanone	Dodecanone	Tridecanone	Tetradecanone	pinonaldehyde	V	Si	Ca	Al	Mg	Hexadecanoic acid
F1	0.26	0.33	0.34	0.37	0.08	0.59	0.30	0.33	0.36	0.50	0.33	0.28	0.33	0.41	0.40	0.41	0.33	0.44	0.25	0.12	0.15	0.13	-0.02	0.36
F2	0.78	0.82	0.83	0.77	0.61	0.31	0.12	0.72	0.03	0.34	0.24	0.70	0.69	0.66	0.67	0.82	0.69	0.67	-0.20	0.16	0.21	0.11	-0.29	-0.09
F3	0.57	0.59	0.56	0.52	0.58	0.74	0.64	0.73	0.75	0.63	0.63	0.31	0.29	0.42	0.35	0.57	0.56	0.24	0.18	0.45	0.40	0.40	0.19	0.47
F4	0.01	0.07	0.00	0.06	0.06	0.24	-0.05	0.18	-0.02	0.31	0.09	0.04	0.10	-0.15	0.50	0.57	0.52	-0.04	-0.13	-0.01	-0.01	-0.02	-0.32	0.79
F5	0.45	0.33	0.28	0.34	0.49	0.16	0.01	0.08	-0.03	0.10	0.02	0.25	0.26	-0.15	0.42	0.37	0.39	-0.04	0.05	-0.02	0.02	-0.05	-0.12	0.69
F6	0.31	0.24	0.25	0.30	0.35	-0.07	-0.18	0.03	-0.27	-0.13	-0.07	0.20	0.22	-0.01	0.49	0.29	0.27	0.00	-0.30	-0.12	0.00	-0.13	-0.24	0.17
F7	0.11	0.08	0.11	0.14	-0.14	0.49	0.30	0.05	0.36	0.42	0.43	0.15	0.19	0.32	0.20	0.19	0.15	0.26	0.44	0.14	0.18	0.13	0.03	0.02

1456 Table A3. Source inventory of $PM_{2.5}$ for Kern County in the San Joaquin Valley in 2008

1457 (downloaded from http://www.arb.ca.gov/ei/emissiondata.htm) (shown as percentage of $PM_{2.5}$)

1458 and sources identified in this study (shown as percentage of $OM_{2.5}$).

1459

Source type		Inventory (%)	This study (%)
Mobile motor sources		31 (80)[a]	65
Petroleum production and refining		0 (1)	14
	Dust	16 (14)	10
	Cooking	2 (4)	7
Miscellaneous processes	Residential fuel combustion	7	ND[b]
	Farming operations	9	ND
	Construction and demolition	1	ND
	Managed burning and disposal	6	ND
Fuel (mainly natural gas) combustion		14	ND
Industrial processes		13	ND
Solvent evaporation		0	ND
Waste disposal		0	ND
Cleaning and surface coatings		0	ND

1460

1461 [a]The numbers in the parentheses represent percentage out of the four sources that are commonly identified in the
1462 source inventory and from this study.
1463 [b]ND represents sources that were not detected from this study.

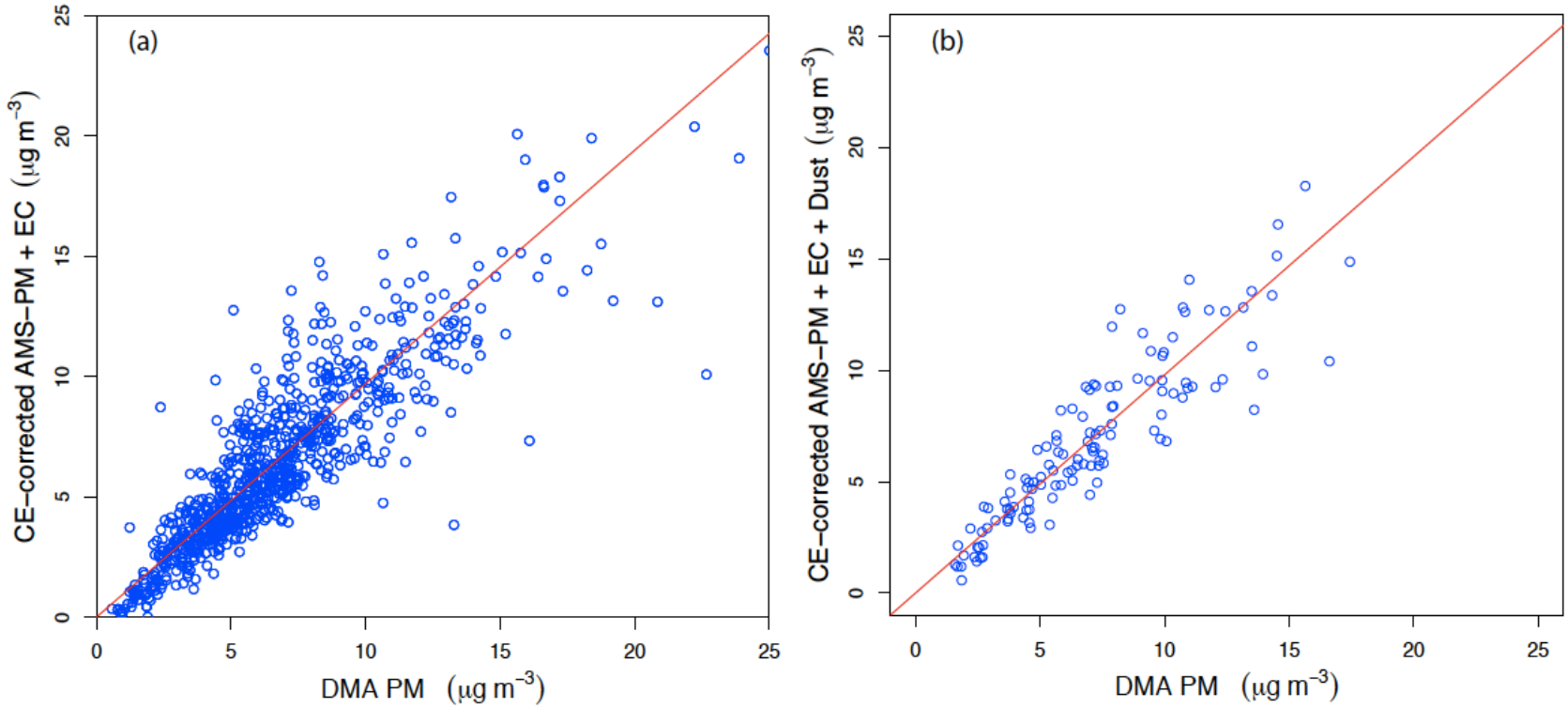
(a)
CE–corrected AMS–PM + EC (μg m^{-3})
DMA PM (μg m^{-3})
0
5
10
15
20
25
(b)
CE–corrected AMS–PM + EC + Dust (μg m^{-3})
DMA PM (μg m^{-3})

Figure 1

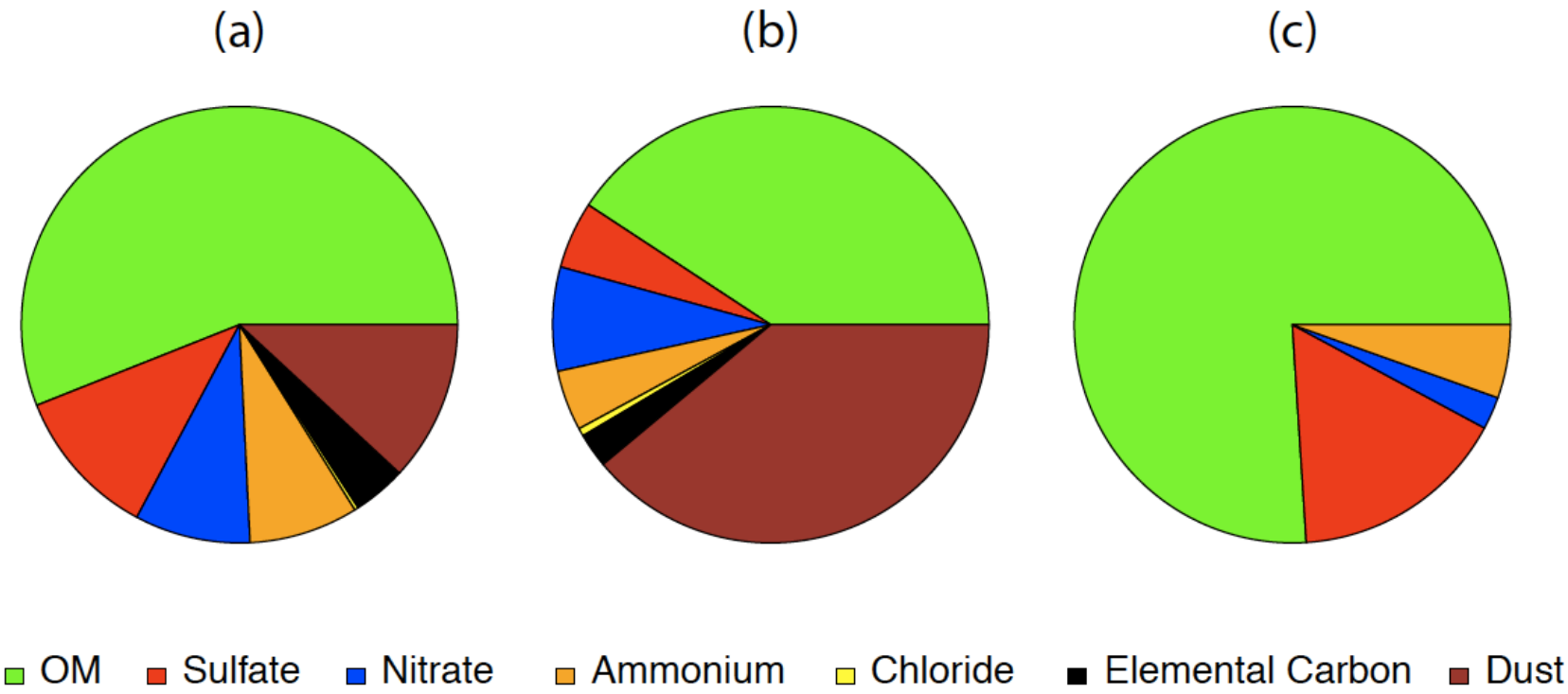
(a)
(b)
(c)
OM
Sulfate
Nitrate
Ammonium
Chloride
Elemental Carbon
Dust

Figure 2

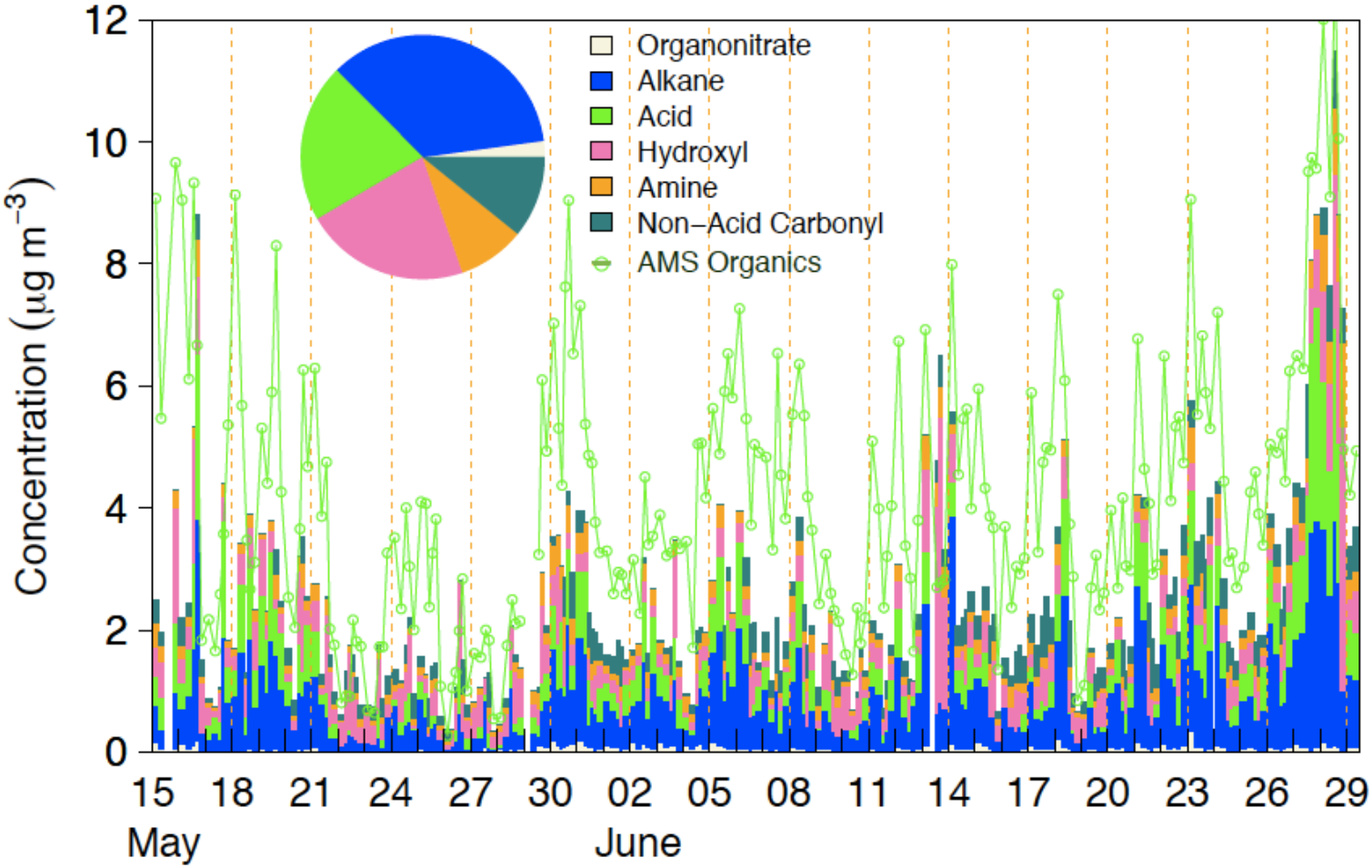
Organonitrate
Alkane
Acid
Hydroxyl
Amine
Non–Acid Carbonyl
AMS Organics
Concentration (μg m^{-3})
0
2
4
6
8
10
12
15
18
21
24
27
30
02
05
08
11
14
17
20
23
26
29
May
June

Figure 3

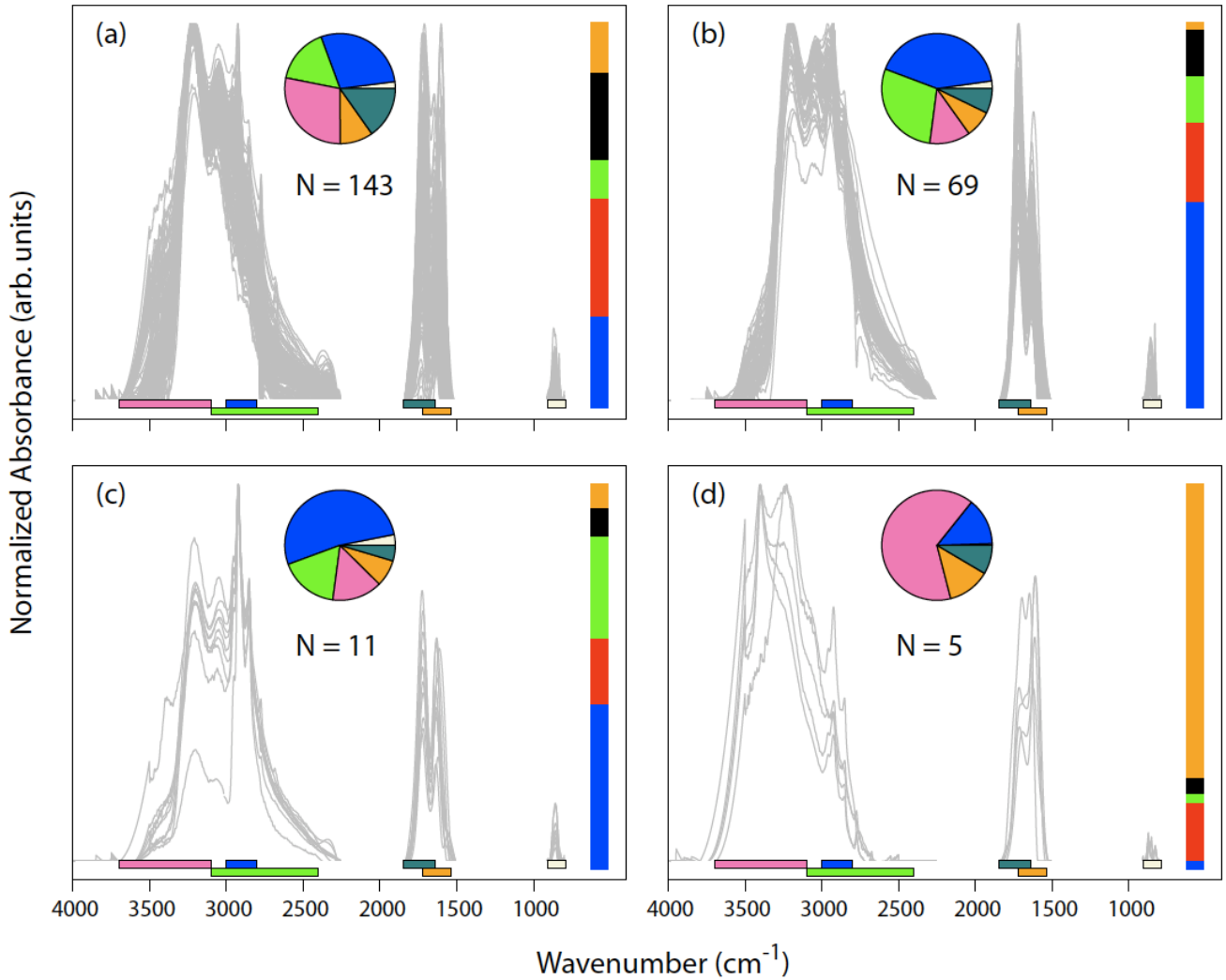
(a)
N = 143
(b)
N = 69
(c)
N = 11
(d)
N = 5
Normalized Absorbance (arb. units)
4000
3500
3000
2500
2000
1500
1000
Wavenumber (cm^{-1})

Figure 4

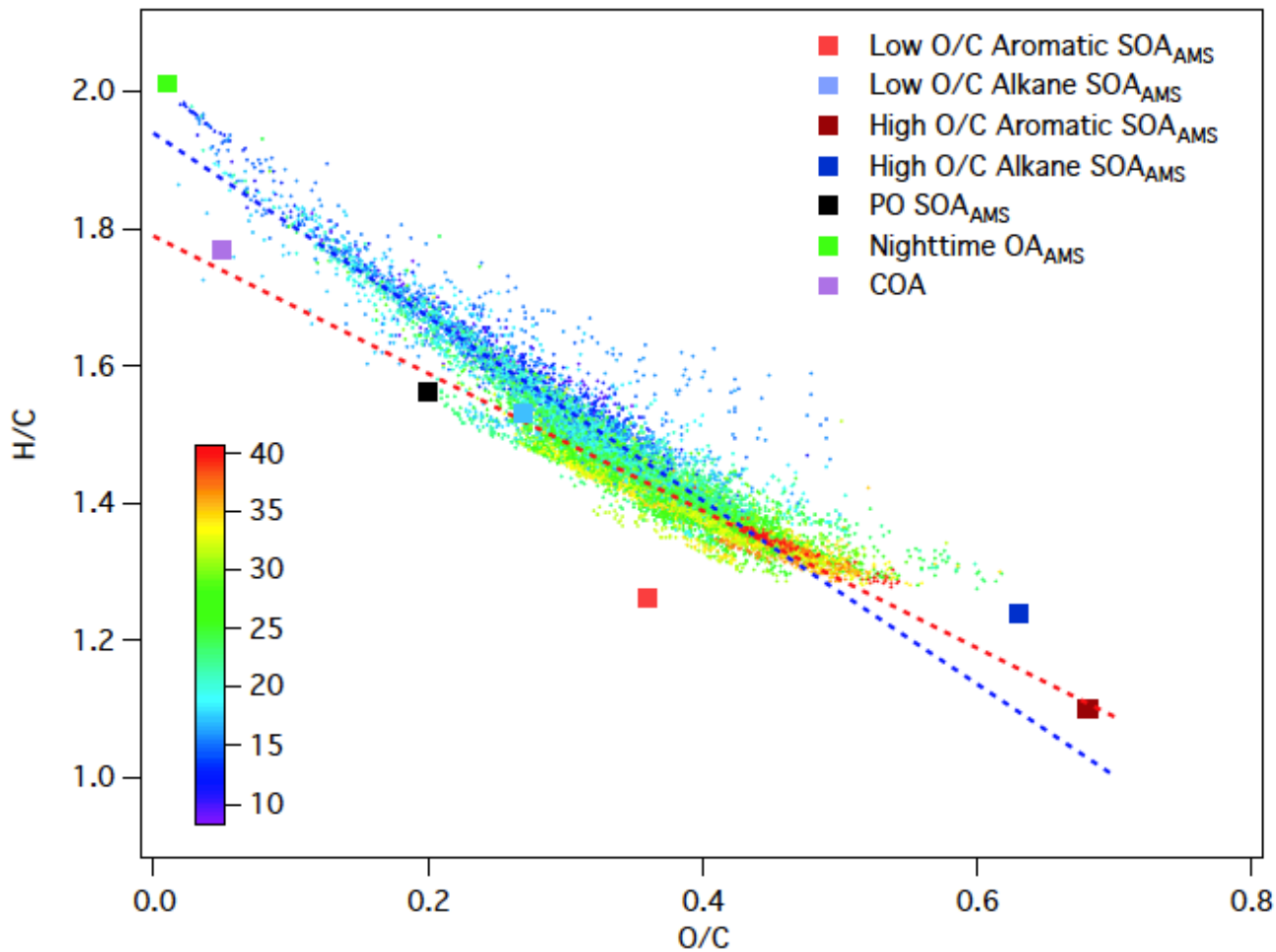
Low O/C Aromatic SOA$_{AMS}$
Low O/C Alkane SOA$_{AMS}$
High O/C Aromatic SOA$_{AMS}$
High O/C Alkane SOA$_{AMS}$
PO SOA$_{AMS}$
Nighttime OA$_{AMS}$
COA
H/C
O/C
2.0
1.8
1.6
1.4
1.2
1.0
0.0
0.2
0.4
0.6
0.8
40
35
30
25
20
15
10

Figure 5

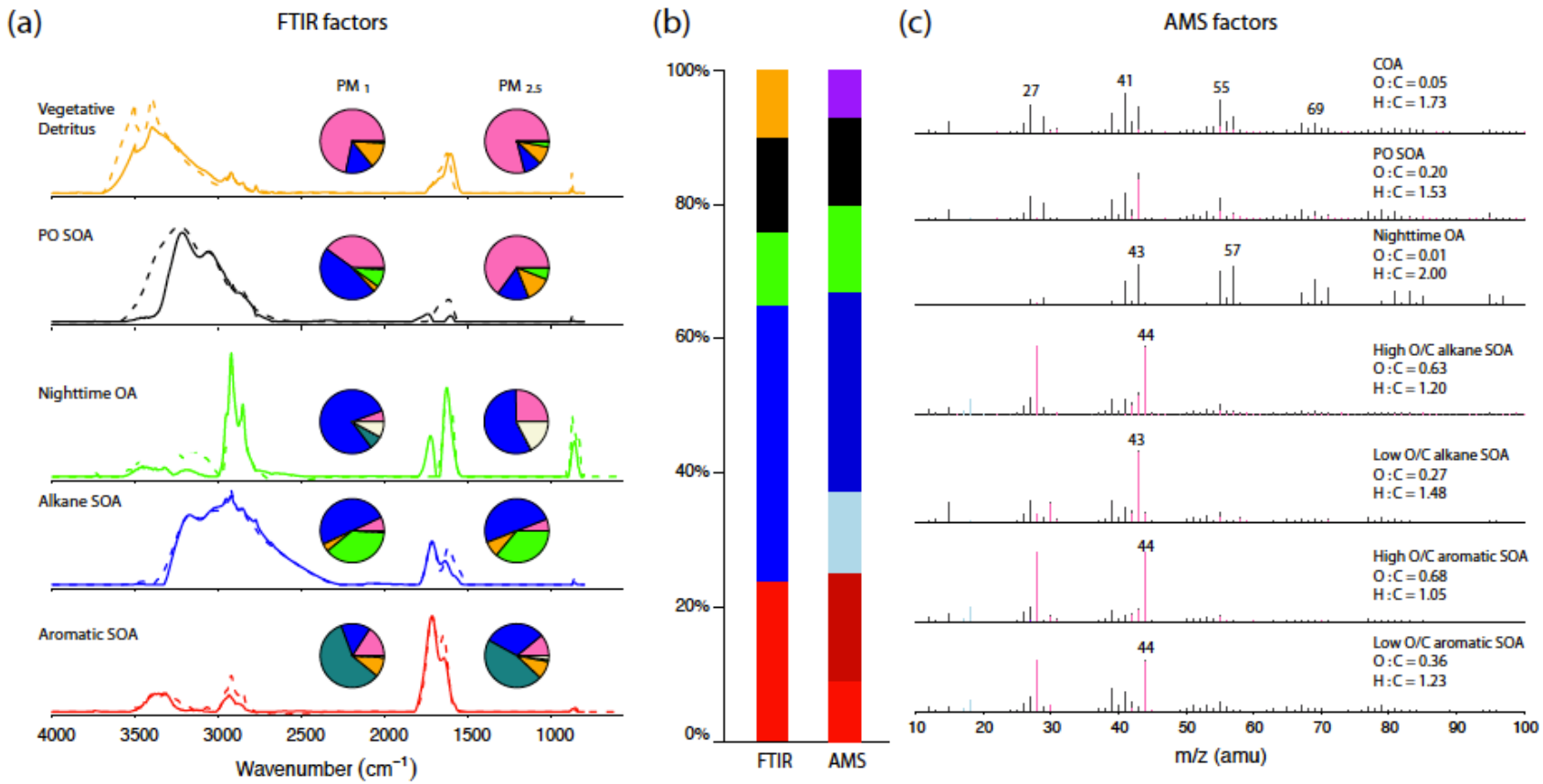
(a)
FTIR factors
PM 1
PM 2.5
Vegetative Detritus
PO SOA
Nighttime OA
Alkane SOA
Aromatic SOA
4000
3500
3000
2500
2000
1500
1000
Wavenumber (cm⁻¹)
(b)
100%
80%
60%
40%
20%
0%
FTIR
AMS
(c)
AMS factors
COA
O:C = 0.05
H:C = 1.73
27
41
55
69
PO SOA
O:C = 0.20
H:C = 1.53
Nighttime OA
O:C = 0.01
H:C = 2.00
43
57
High O/C alkane SOA
O:C = 0.63
H:C = 1.20
44
Low O/C alkane SOA
O:C = 0.27
H:C = 1.48
43
High O/C aromatic SOA
O:C = 0.68
H:C = 1.05
44
Low O/C aromatic SOA
O:C = 0.36
H:C = 1.23
44
10
20
30
40
50
60
70
80
90
100
m/z (amu)

Figure 6

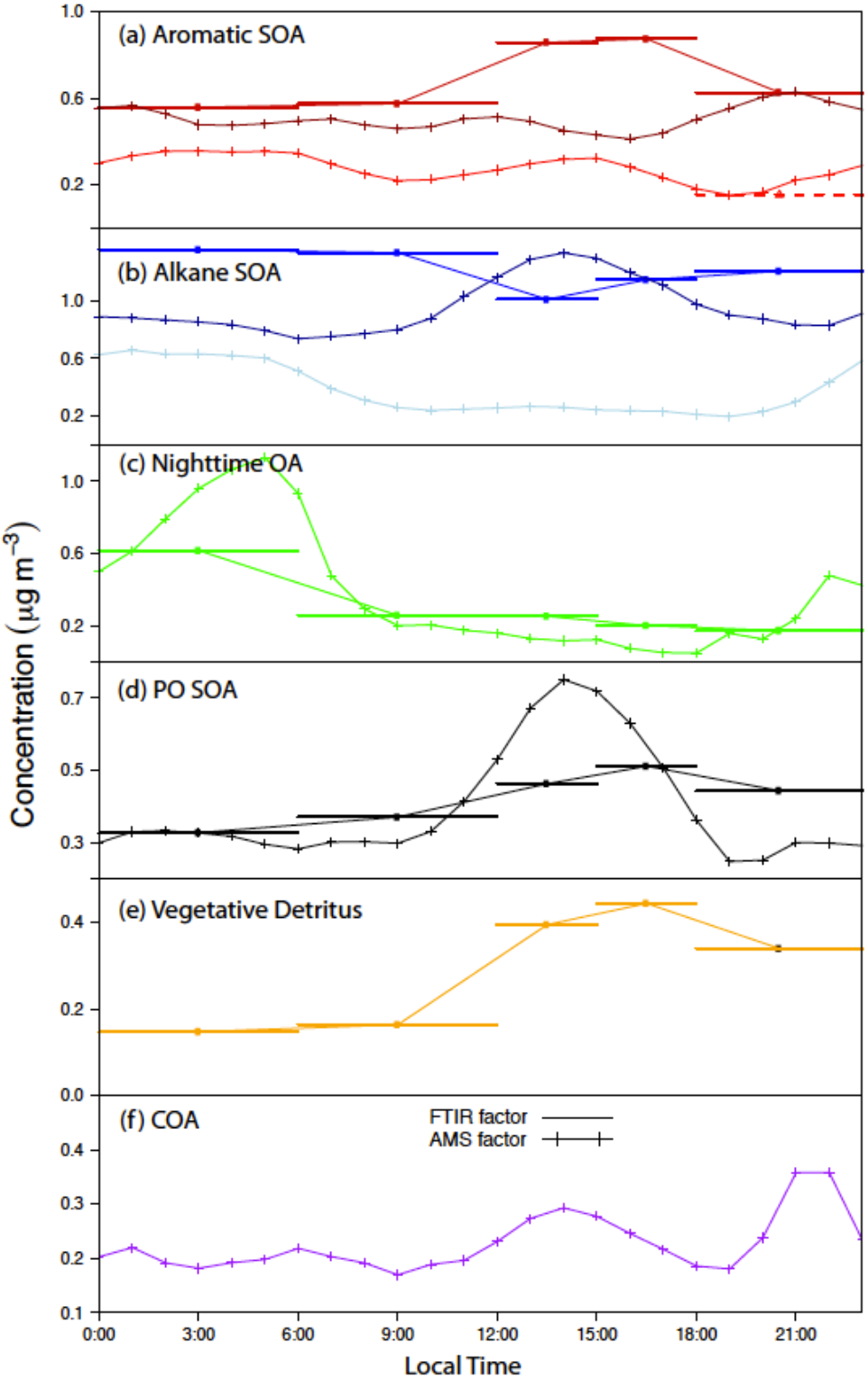
(a) Aromatic SOA
(b) Alkane SOA
(c) Nighttime OA
(d) PO SOA
(e) Vegetative Detritus
(f) COA
FTIR factor
AMS factor
Concentration (μg m^{-3})
Local Time
0:00
3:00
6:00
9:00
12:00
15:00
18:00
21:00

Figure 7

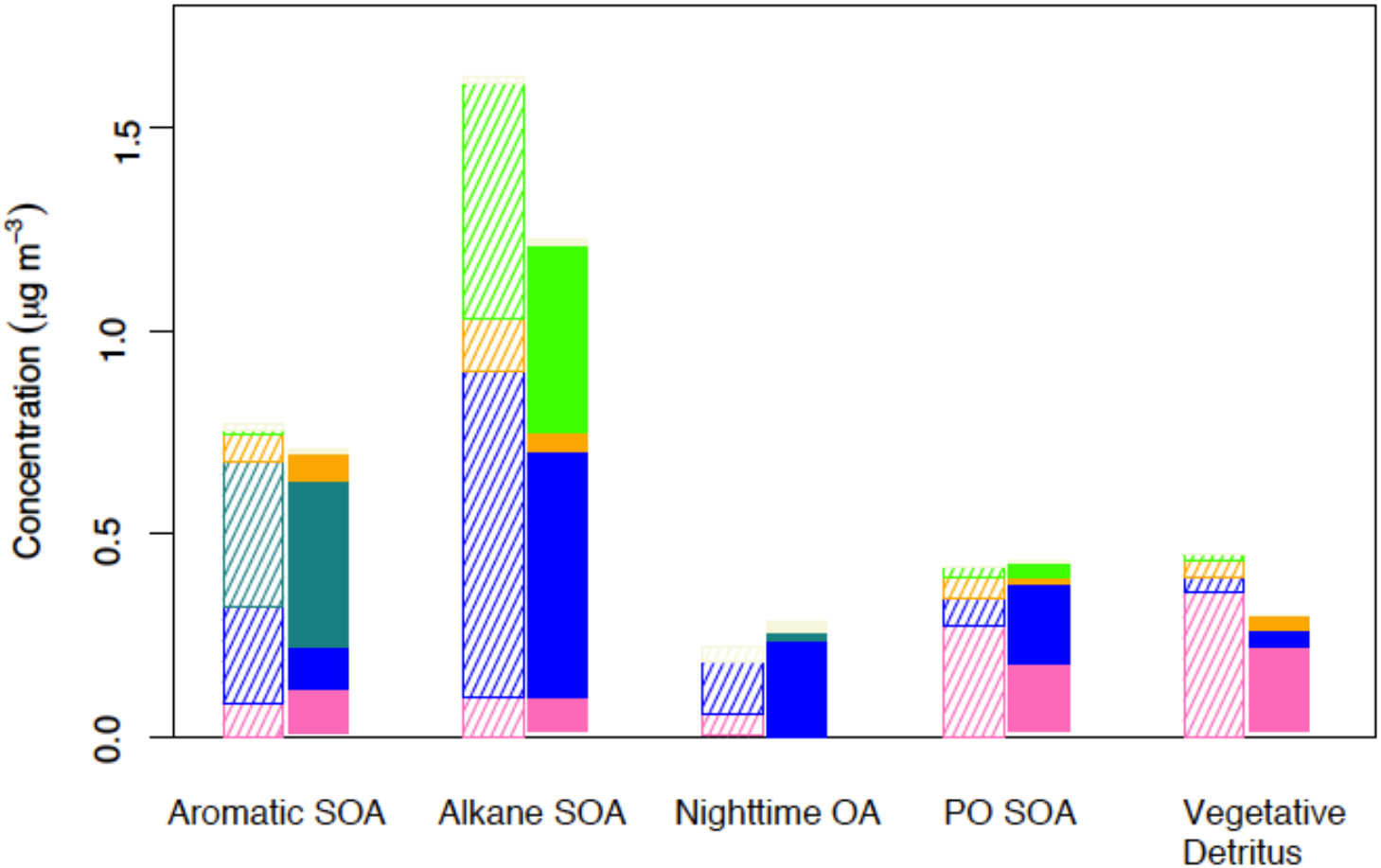
Concentration (μg m^{-3})
0.0
0.5
1.0
1.5
Aromatic SOA
Alkane SOA
Nighttime OA
PO SOA
Vegetative Detritus

Figure 8

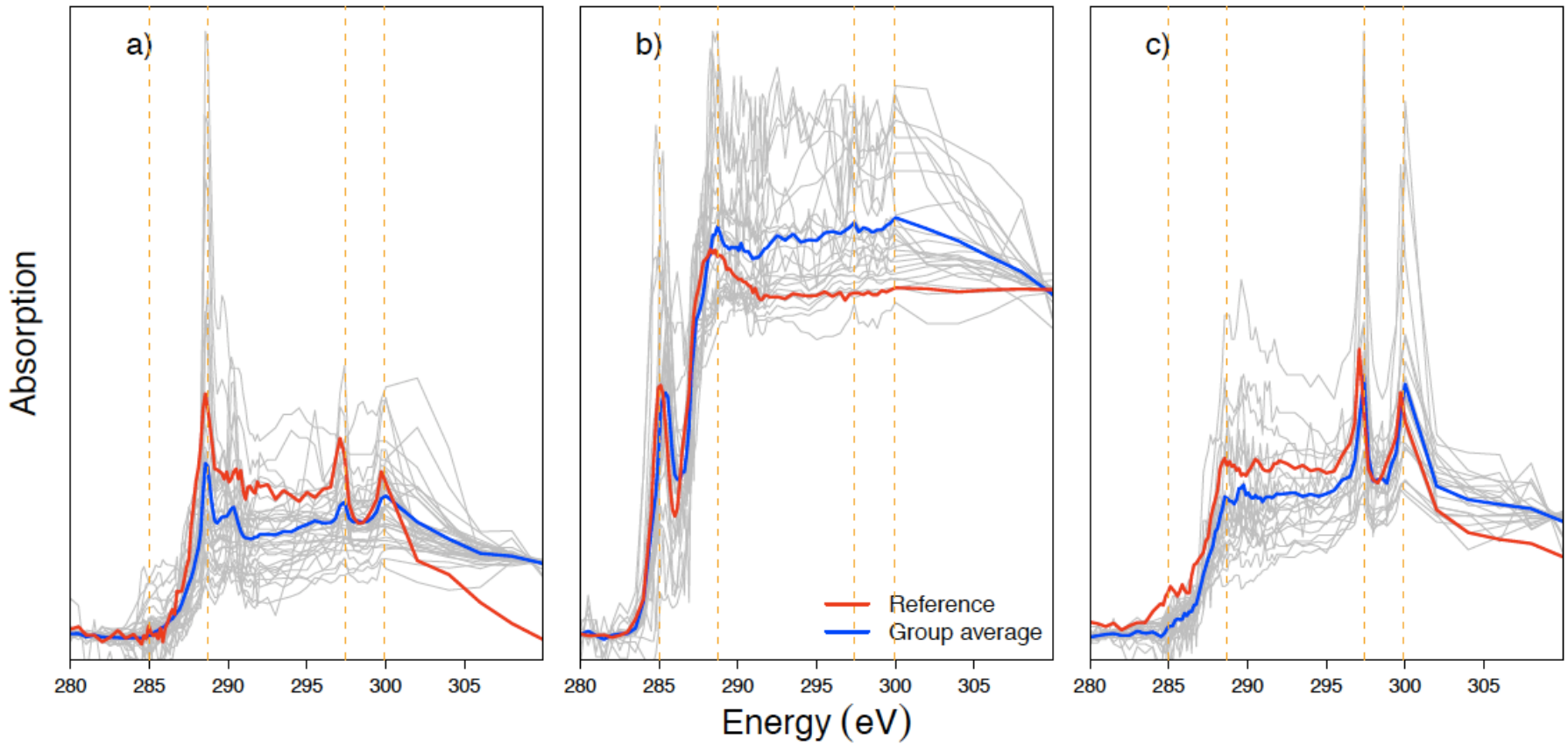
a)
b)
c)
Absorption
Reference
Group average
280
285
290
295
300
305
Energy (eV)

Figure 9

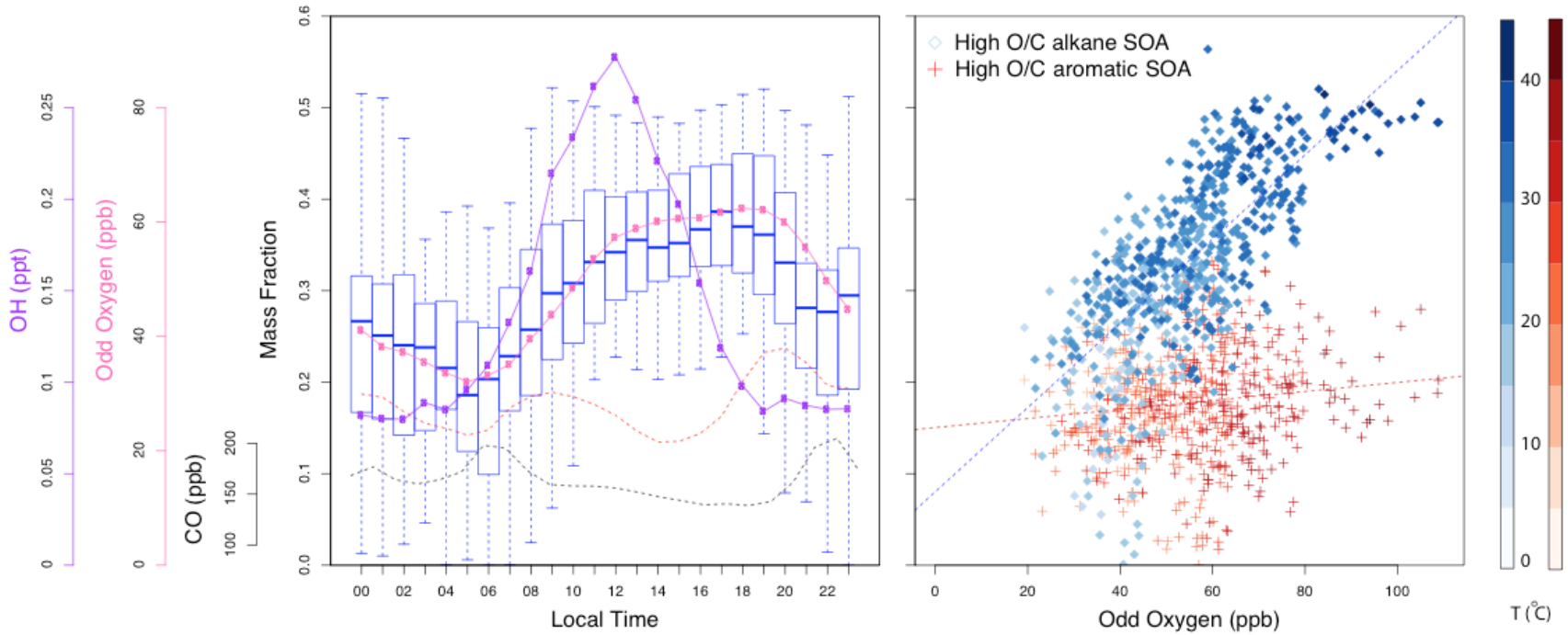
OH (ppt)
Odd Oxygen (ppb)
CO (ppb)
Mass Fraction
Local Time
High O/C alkane SOA
High O/C aromatic SOA
Odd Oxygen (ppb)
T (°C)

Figure 10

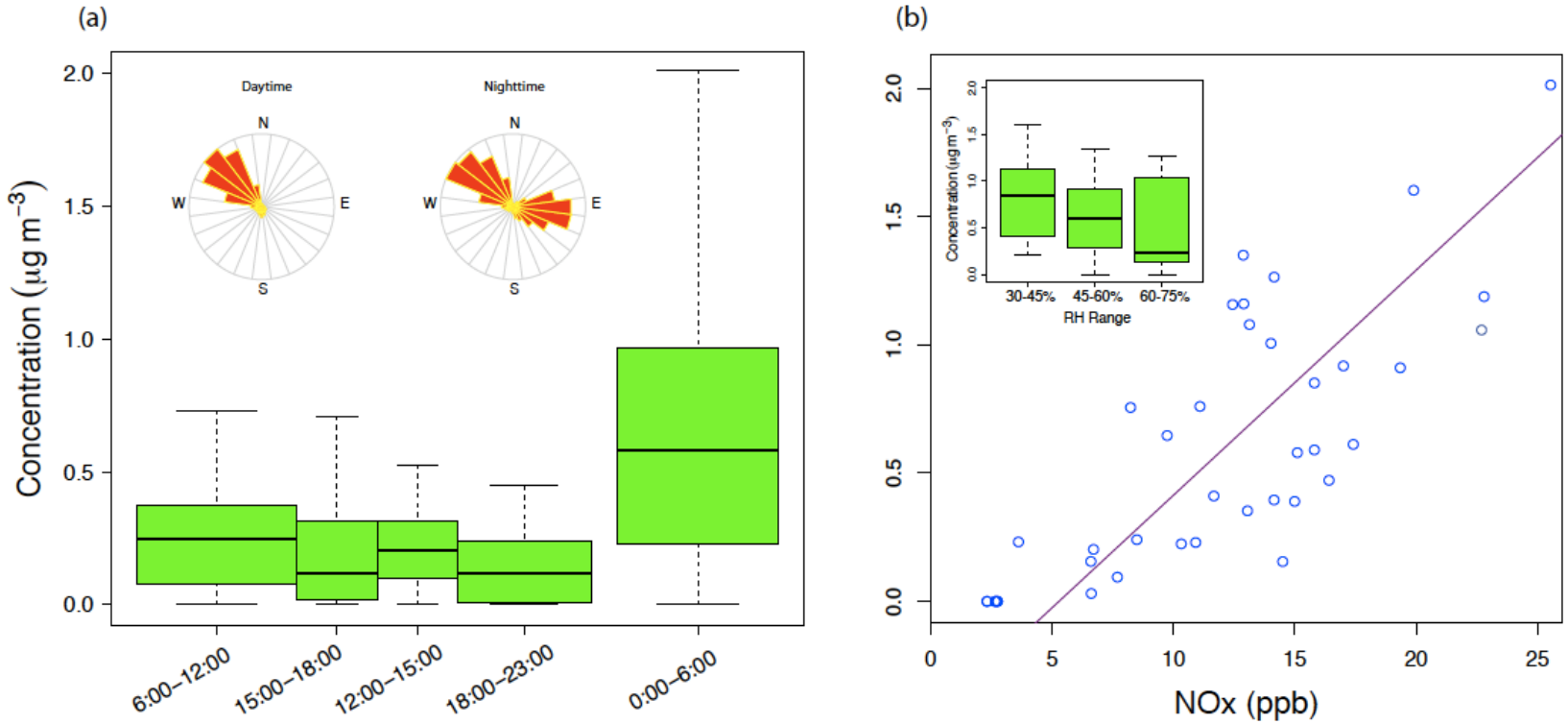
(a)
Daytime
Nighttime
N
W
E
S
Concentration (μg m⁻³)
2.0
1.5
1.0
0.5
0.0
6:00–12:00
15:00–18:00
12:00–15:00
18:00–23:00
0:00–6:00
(b)
Concentration (μg m⁻³)
30-45%
45-60%
60-75%
RH Range
NOx (ppb)
0
5
10
15
20
25

Figure 11

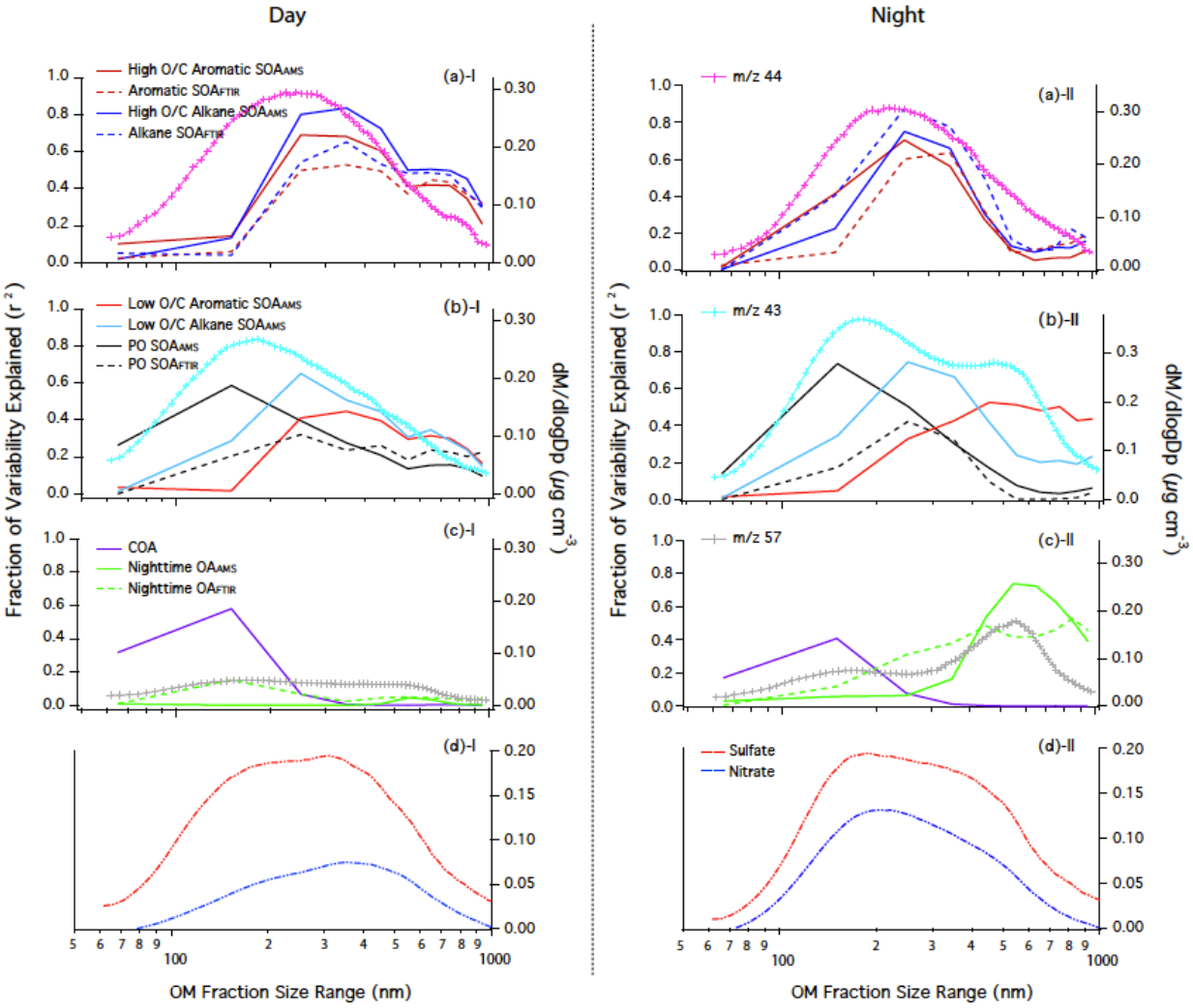
Day
Night
High O/C Aromatic SOAAMS
Aromatic SOAFTIR
High O/C Alkane SOAAMS
Alkane SOAFTIR
(a)-I
m/z 44
(a)-II
Low O/C Aromatic SOAAMS
Low O/C Alkane SOAAMS
PO SOAAMS
PO SOAFTIR
(b)-I
m/z 43
(b)-II
COA
Nighttime OAAMS
Nighttime OAFTIR
(c)-I
m/z 57
(c)-II
(d)-I
Sulfate
Nitrate
(d)-II
Fraction of Variability Explained (r²)
dM/dlogDp (μg cm⁻³)
OM Fraction Size Range (nm)

Figure 12

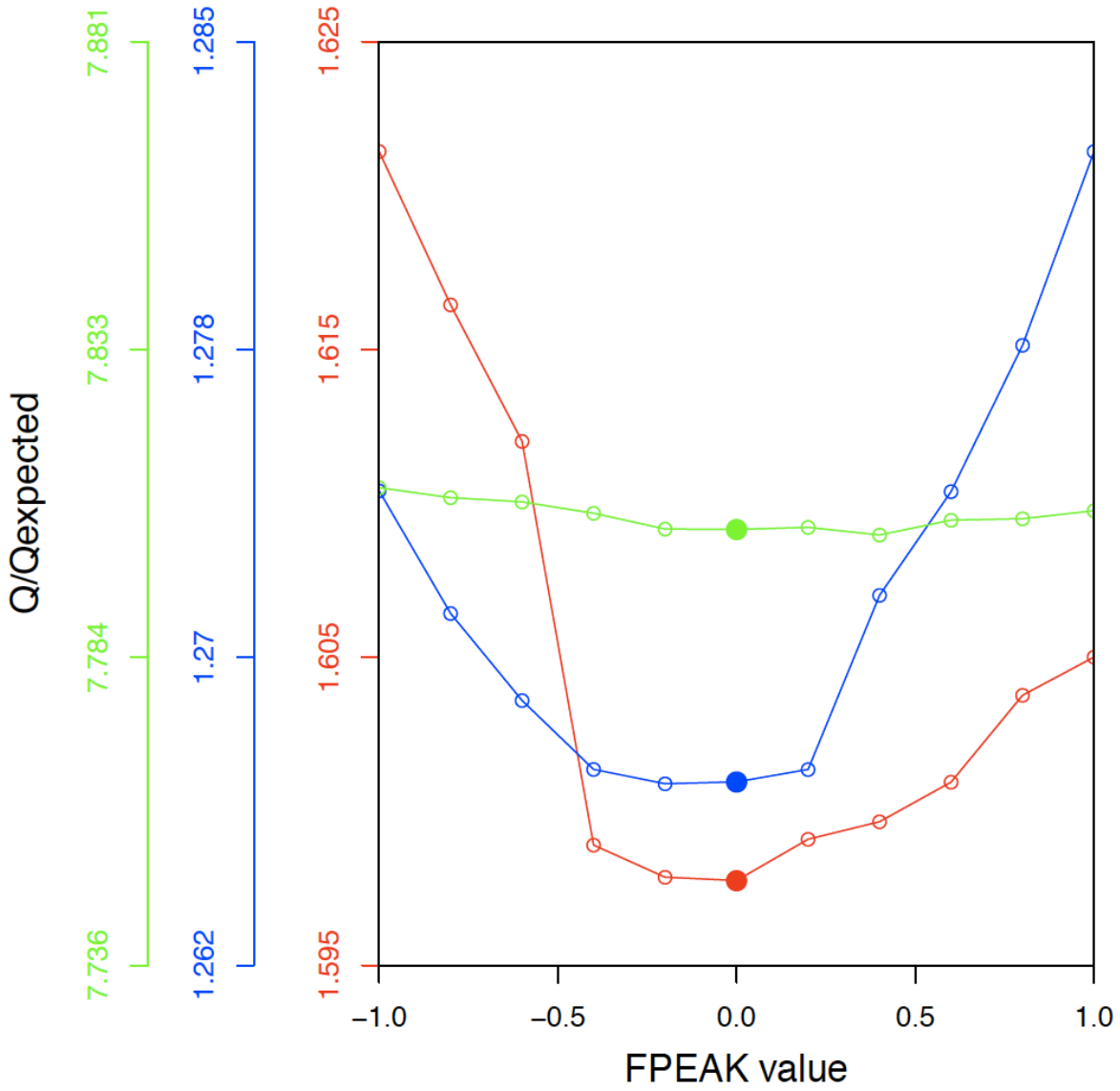
Q/Qexpected
7.736
7.784
7.833
7.881
1.262
1.27
1.278
1.285
1.595
1.605
1.615
1.625
−1.0
−0.5
0.0
0.5
1.0
FPEAK value

Figure A1

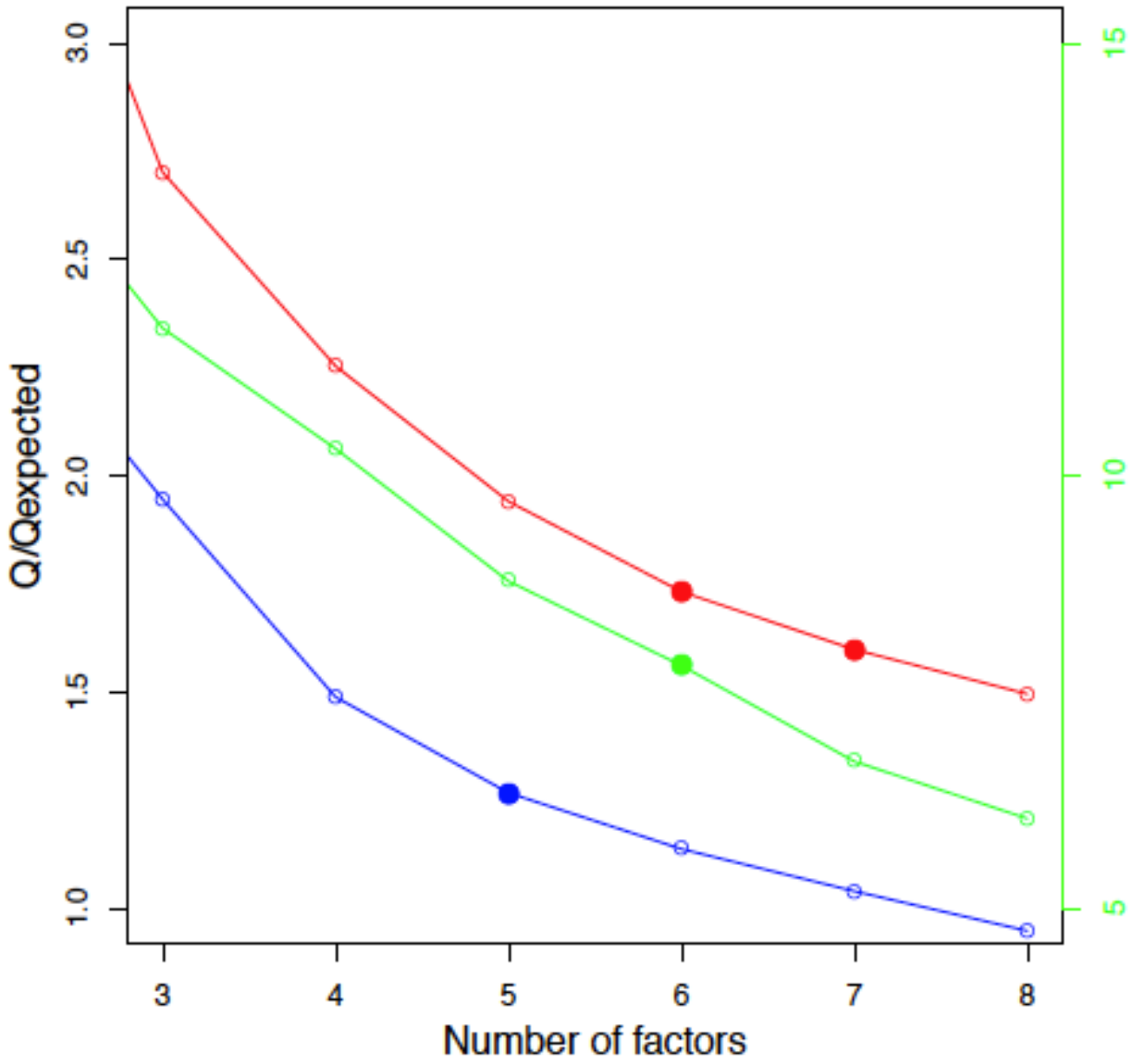

Figure A2

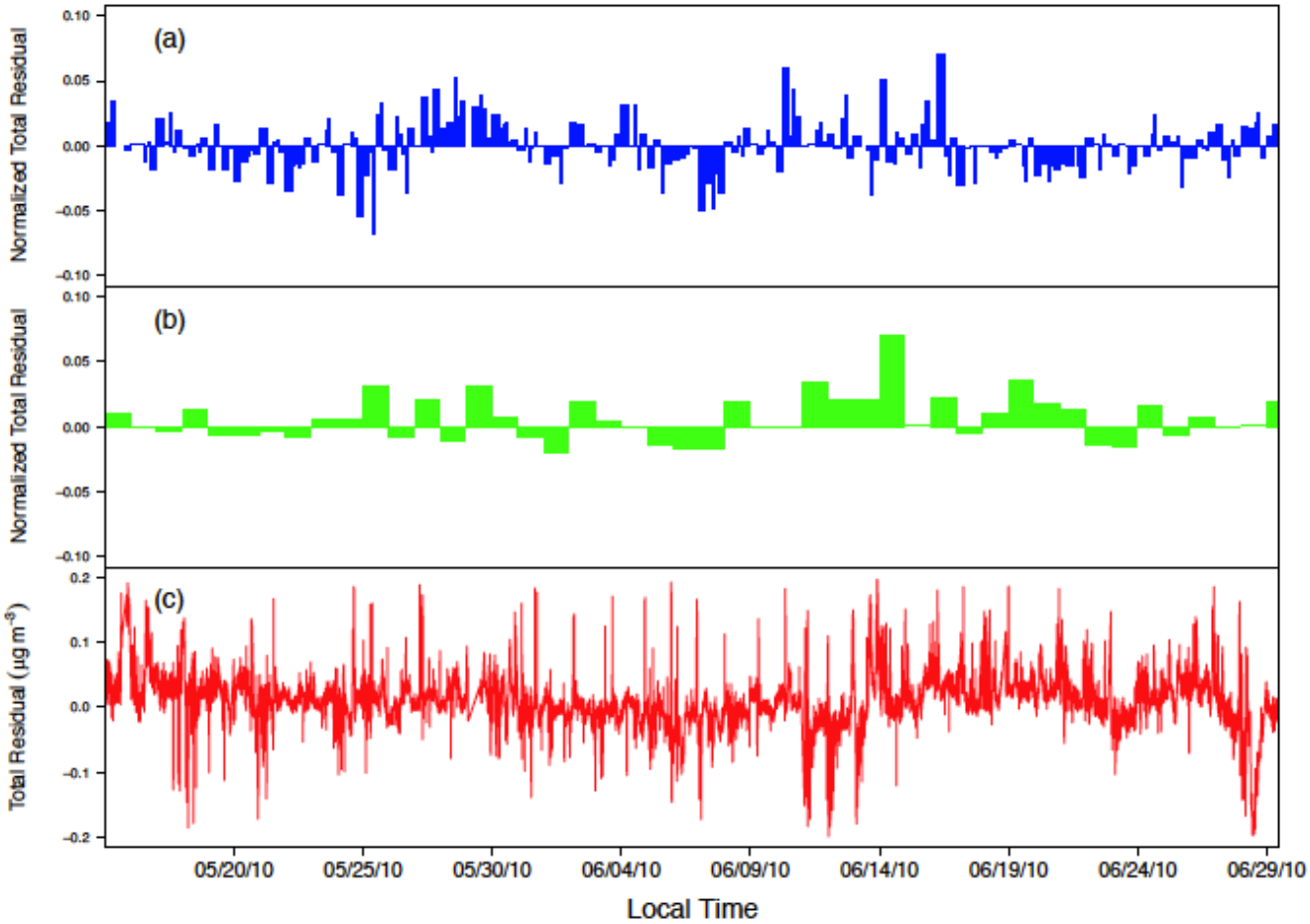
(a)
(b)
(c)
Normalized Total Residual
Normalized Total Residual
Total Residual (μg m⁻³)
0.10
0.05
0.00
−0.05
−0.10
0.2
0.1
0.0
−0.1
−0.2
05/20/10
05/25/10
05/30/10
06/04/10
06/09/10
06/14/10
06/19/10
06/24/10
06/29/10
Local Time

Figure A3

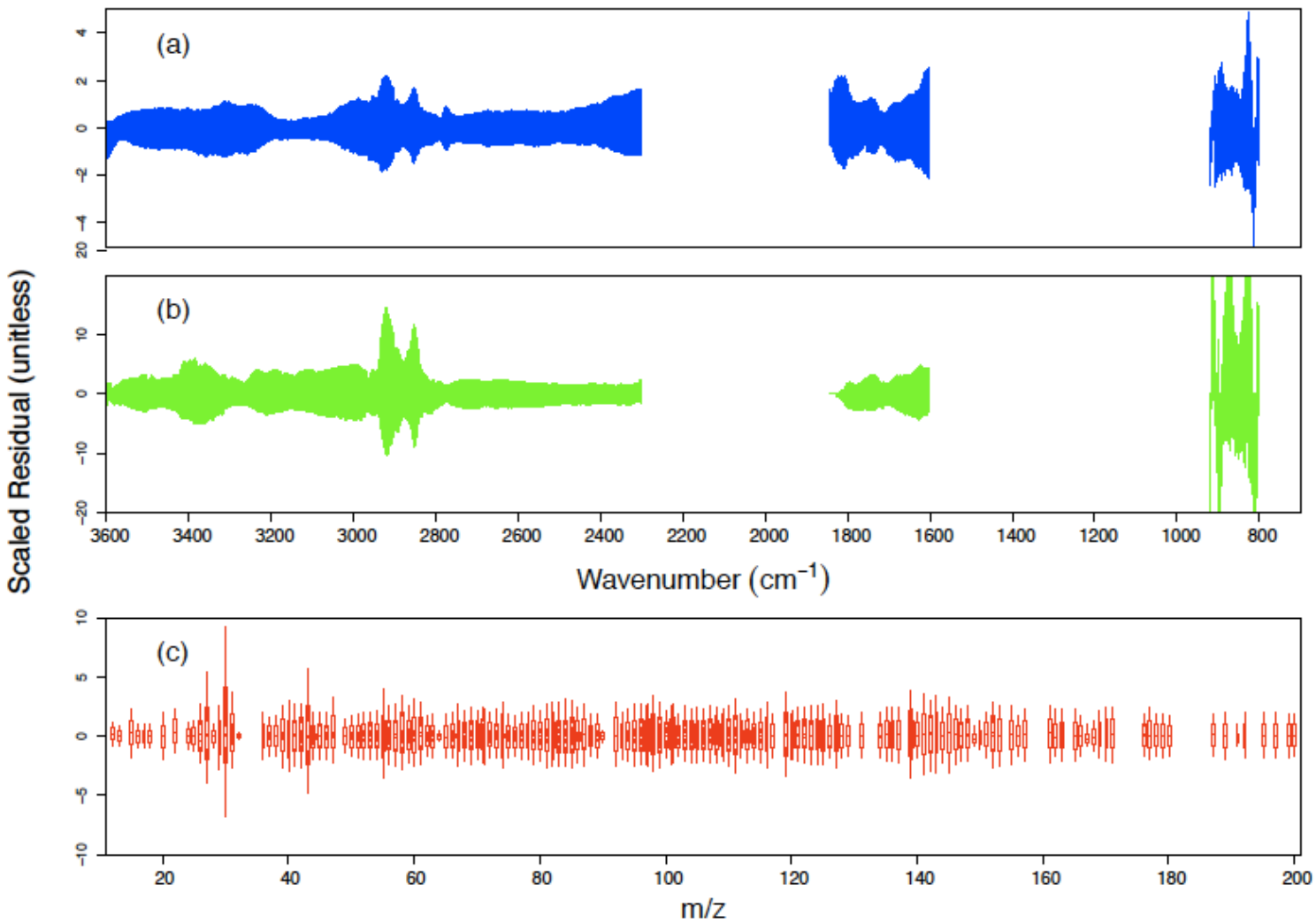

Figure A4

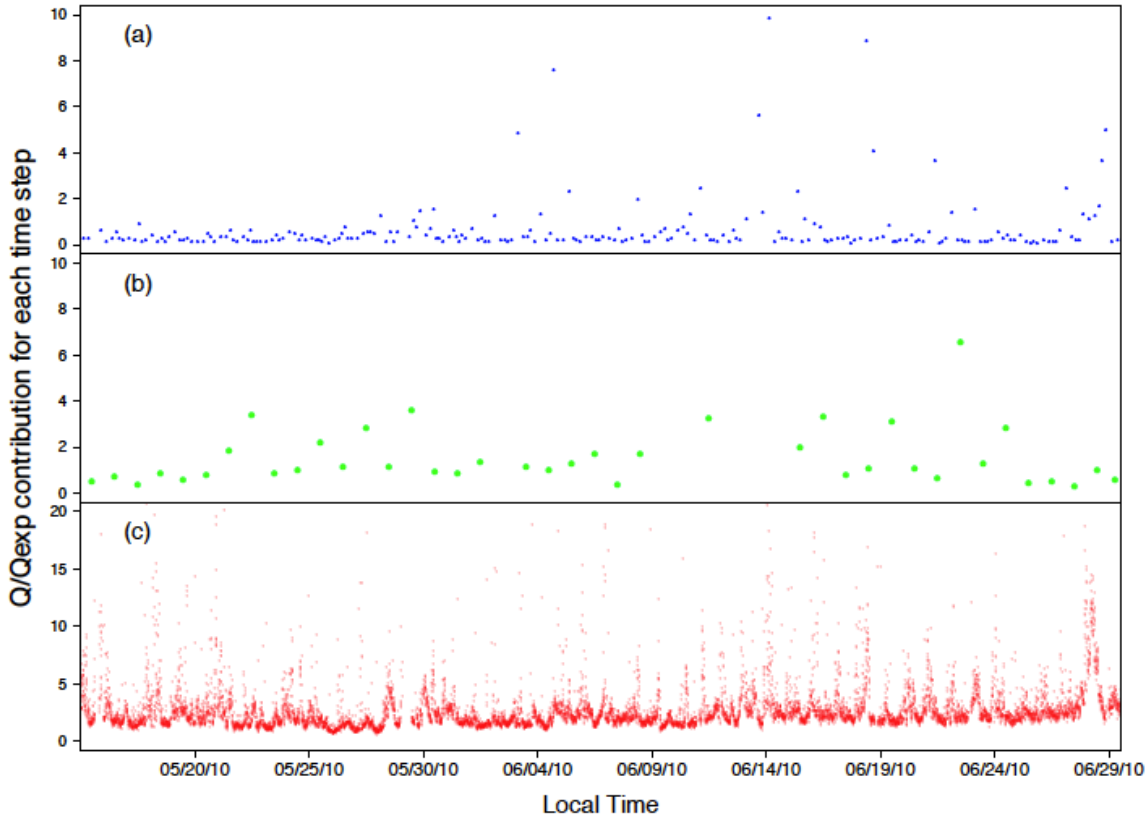
(a)
(b)
(c)
Q/Qexp contribution for each time step
Local Time
05/20/10
05/25/10
05/30/10
06/04/10
06/09/10
06/14/10
06/19/10
06/24/10
06/29/10

Figure A5

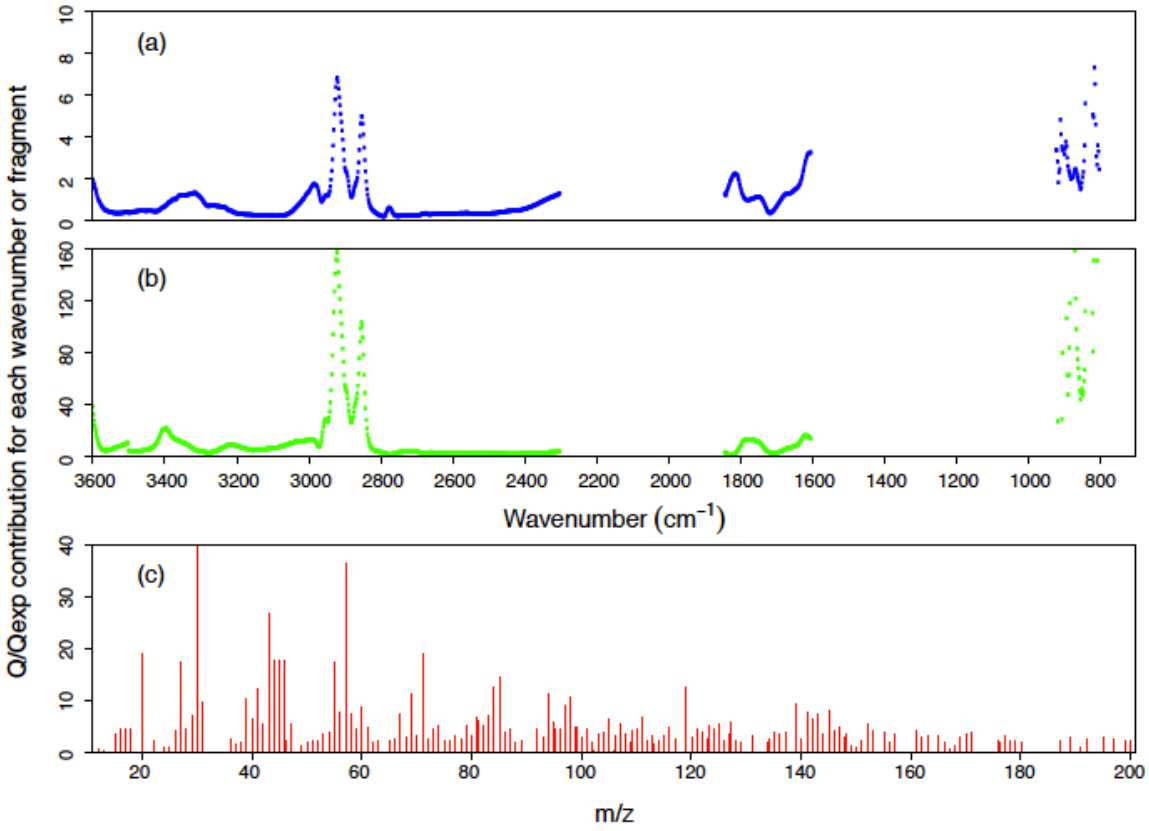
(a)
(b)
(c)
Q/Qexp contribution for each wavenumber or fragment
Wavenumber (cm^{-1})
m/z

Figure A6

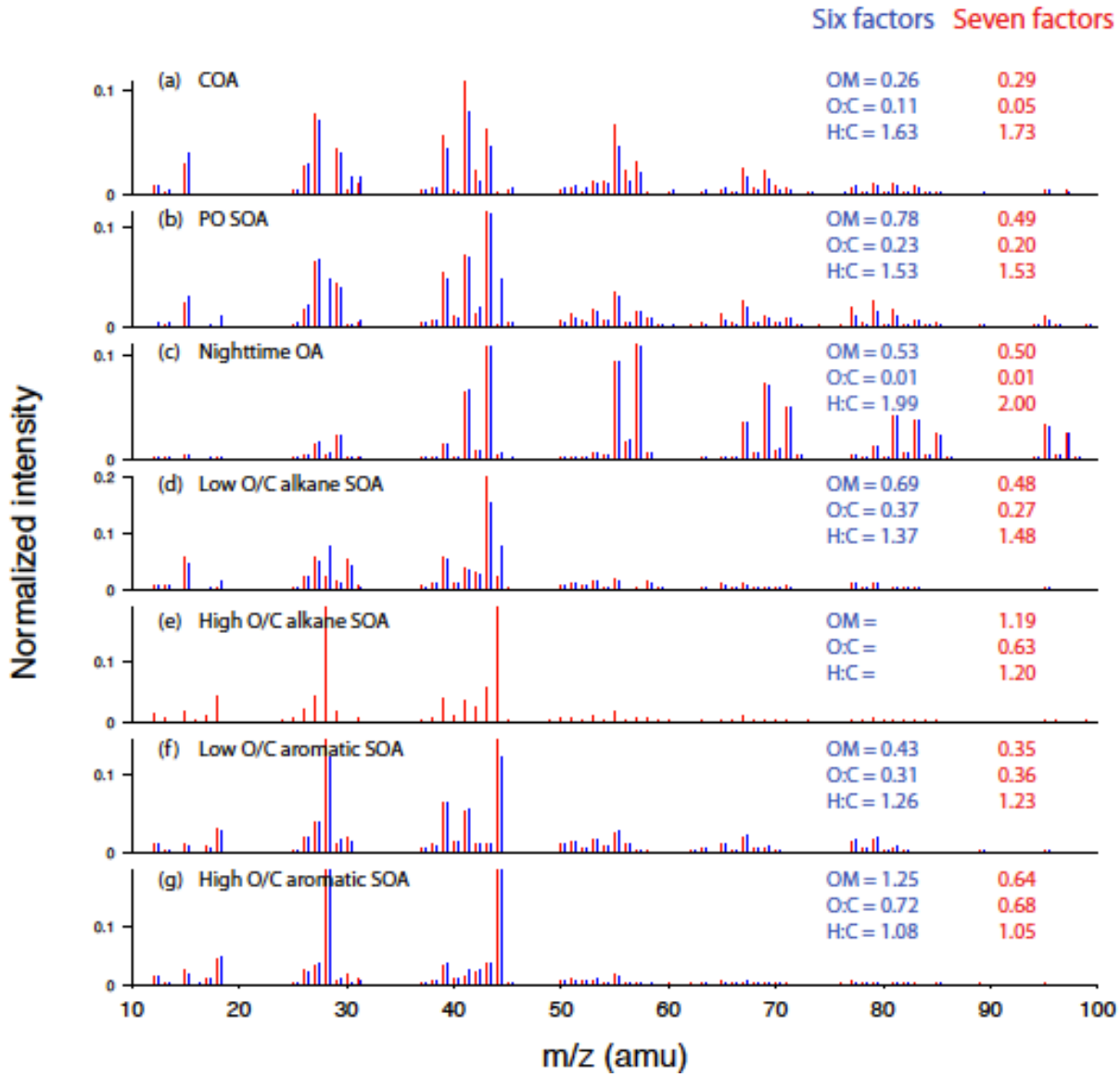
Six factors
Seven factors
(a) COA
OM = 0.26 0.29
O:C = 0.11 0.05
H:C = 1.63 1.73
(b) PO SOA
OM = 0.78 0.49
O:C = 0.23 0.20
H:C = 1.53 1.53
(c) Nighttime OA
OM = 0.53 0.50
O:C = 0.01 0.01
H:C = 1.99 2.00
(d) Low O/C alkane SOA
OM = 0.69 0.48
O:C = 0.37 0.27
H:C = 1.37 1.48
(e) High O/C alkane SOA
OM = 1.19
O:C = 0.63
H:C = 1.20
(f) Low O/C aromatic SOA
OM = 0.43 0.35
O:C = 0.31 0.36
H:C = 1.26 1.23
(g) High O/C aromatic SOA
OM = 1.25 0.64
O:C = 0.72 0.68
H:C = 1.08 1.05
Normalized intensity
m/z (amu)

Figure A7

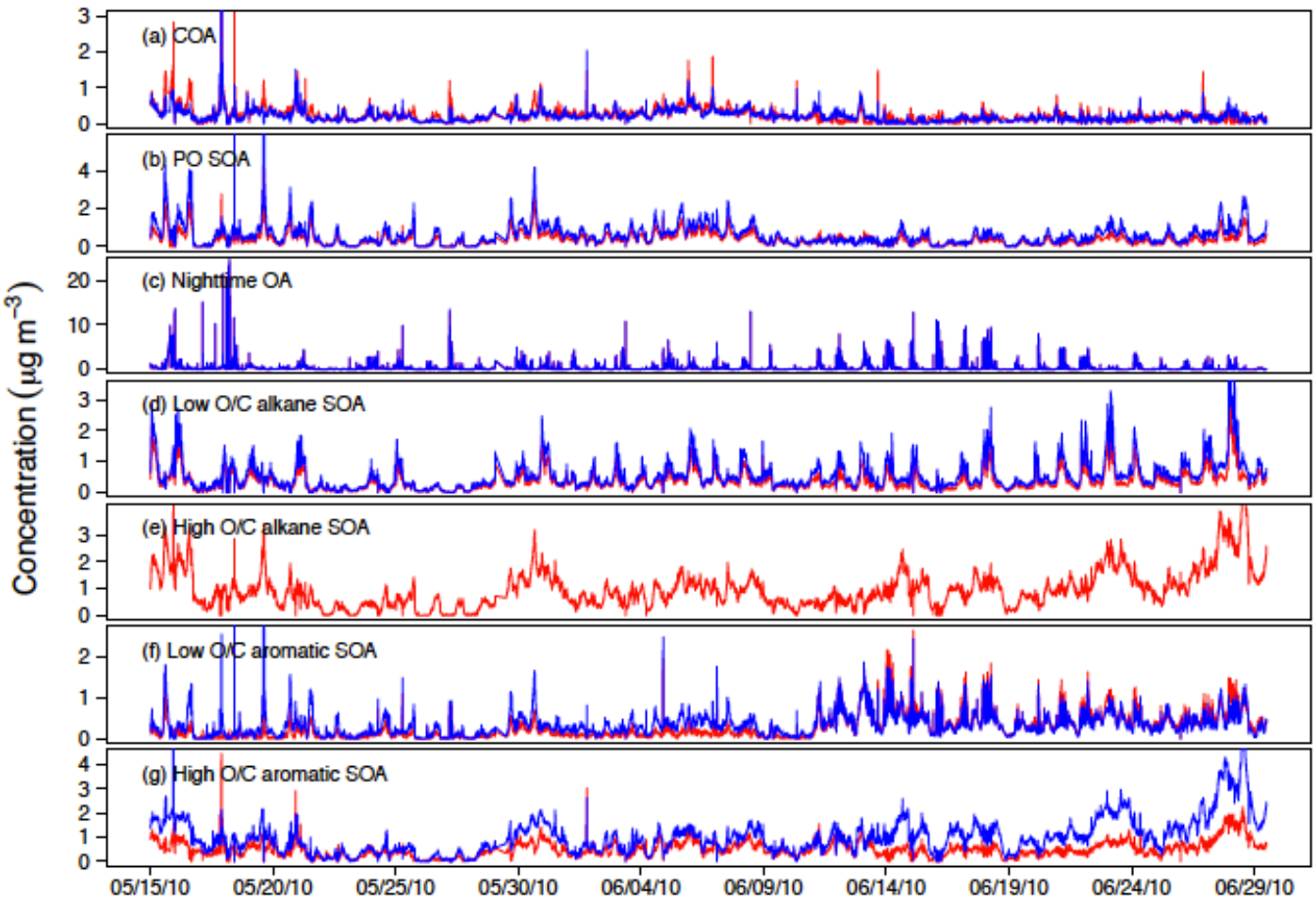
(a) COA
(b) PO SOA
(c) Nighttime OA
(d) Low O/C alkane SOA
(e) High O/C alkane SOA
(f) Low O/C aromatic SOA
(g) High O/C aromatic SOA
Concentration (μg m^{-3})
05/15/10
05/20/10
05/25/10
05/30/10
06/04/10
06/09/10
06/14/10
06/19/10
06/24/10
06/29/10

Figure A8

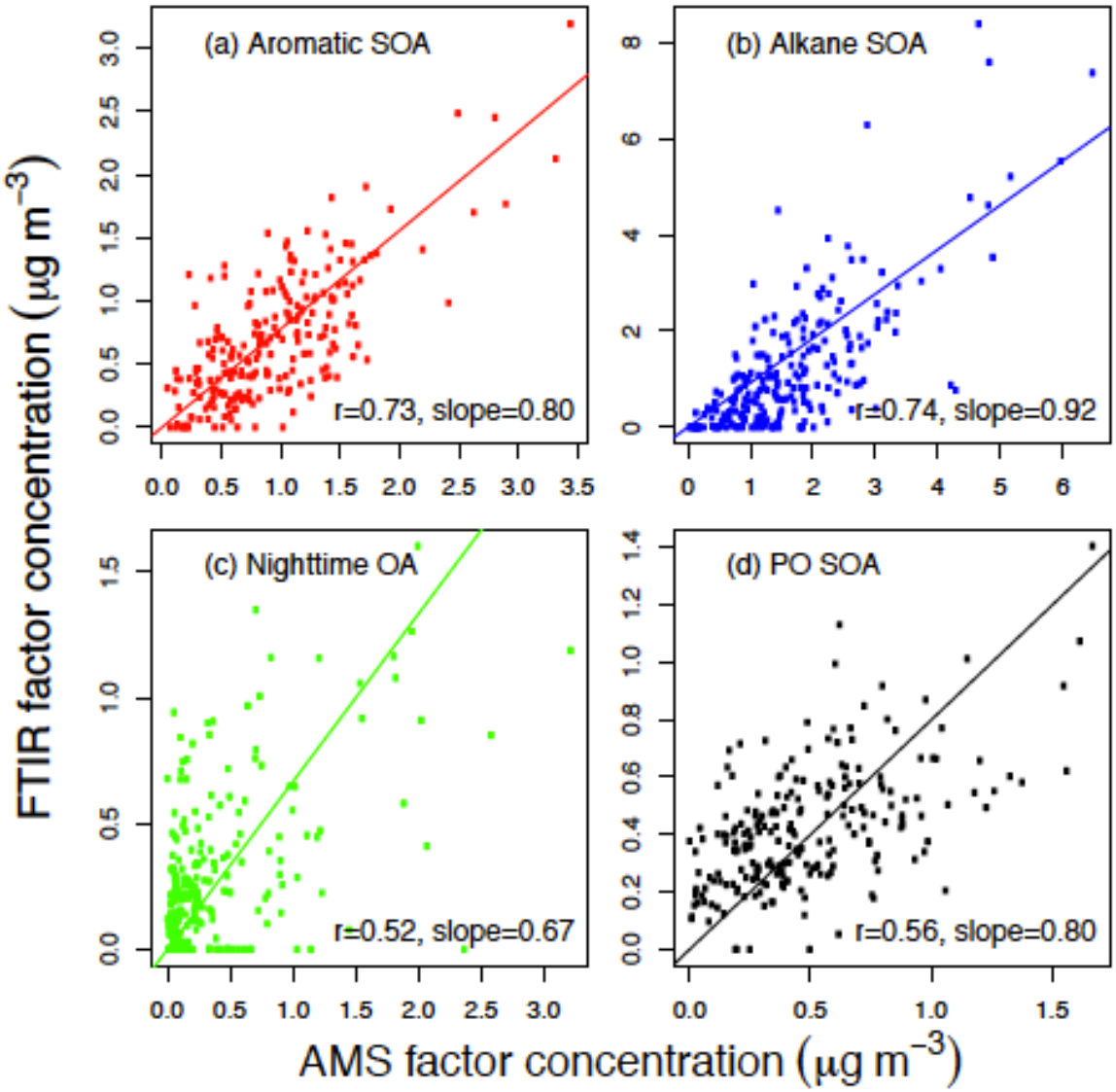
(a) Aromatic SOA
r=0.73, slope=0.80
(b) Alkane SOA
r=0.74, slope=0.92
(c) Nighttime OA
r=0.52, slope=0.67
(d) PO SOA
r=0.56, slope=0.80
FTIR factor concentration (μg m^{-3})
AMS factor concentration (μg m^{-3})

Figure A9